

JOINT TRANSPORTATION RESEARCH PROGRAM

INDIANA DEPARTMENT OF TRANSPORTATION
AND PURDUE UNIVERSITY



Efficient Pavement Thickness Design for Indiana



Tommy Nantung, Jusang Lee, Yu Tian

RECOMMENDED CITATION

Nantung, T., Lee, J., & Tian, Y. (2018). *Efficient pavement thickness design for Indiana* (Joint Transportation Research Program Publication No. FHWA/IN/JTRP-2018/06). West Lafayette, IN: Purdue University. <https://doi.org/10.5703/1288284316649>

AUTHORS

Tommy Nantung, PhD, PE

Section Manager
Office of Research and Development
Indiana Department of Transportation
(765) 463-1521
tnantung@indot.in.gov
Corresponding Author

Jusang Lee, PhD, PE

Asphalt Pavement Research Engineer
Office of Research and Development
Indiana Department of Transportation
(765) 463-1521
jlee@indot.in.gov
Corresponding Author

Yu Tian

Graduate Research Assistant
Lyles School of Civil Engineering
Purdue University

JOINT TRANSPORTATION RESEARCH PROGRAM

The Joint Transportation Research Program serves as a vehicle for INDOT collaboration with higher education institutions and industry in Indiana to facilitate innovation that results in continuous improvement in the planning, design, construction, operation, management and economic efficiency of the Indiana transportation infrastructure. https://engineering.purdue.edu/JTRP/index_html

Published reports of the Joint Transportation Research Program are available at <http://docs.lib.purdue.edu/jtrp/>.

NOTICE

The contents of this report reflect the views of the authors, who are responsible for the facts and the accuracy of the data presented herein. The contents do not necessarily reflect the official views and policies of the Indiana Department of Transportation or the Federal Highway Administration. The report does not constitute a standard, specification or regulation.

COPYRIGHT

Copyright 2018 by Purdue University. All rights reserved.
Print ISBN: 978-1-62260-498-2

1. Report No. FHWA/IN/JTRP-2018/06	2. Government Accession No.	3. Recipient's Catalog No.	
4. Title and Subtitle Efficient Pavement Thickness Design for Indiana		5. Report Date April 2018	6. Performing Organization Code
7. Author(s) Tommy Nantung, Jusang Lee, Yu Tian		8. Performing Organization Report No. FHWA/IN/JTRP-2018/06	
9. Performing Organization Name and Address Joint Transportation Research Program Hall for Discovery and Learning Research (DLR), Suite 204 207 S. Martin Jischke Drive West Lafayette, IN 47907		10. Work Unit No.	11. Contract or Grant No. SPR-3307
12. Sponsoring Agency Name and Address Indiana Department of Transportation State Office Building 100 North Senate Avenue Indianapolis, IN 46204		13. Type of Report and Period Covered Final Report	
15. Supplementary Notes Prepared in cooperation with the Indiana Department of Transportation and Federal Highway Administration.		14. Sponsoring Agency Code	
16. Abstract <p>Over the past several decades, a dramatic increase in traffic volume, axle loads, and tire pressure has led to rapidly deteriorated pavements in the United States. Several types of pavement surface distresses have been noted by many state agencies across the country. Among these distresses, permanent deformation, also known as rutting, is one of the most serious forms of flexible pavement distress. This research investigates the fundamentals of rutting behavior for full-depth flexible pavements. The scope incorporates an experimental study using full-scale accelerated pavement tests (APTs) to monitor the evolution of the transverse profiles of each pavement structural layer. The findings were then employed to improve the rutting model that is embedded in the current pavement design method, the Mechanistic-Empirical Pavement Design Guide (MEPDG).</p> <p>Four APT sections were constructed using two typical pavement structures and two types of surface course material. A mid-depth rut monitoring and automated laser profile system was designed to reconstruct the transverse profiles at each pavement layer interface throughout the process of accelerated pavement deterioration that is produced during the APT. The contributions of each pavement structural layer to rutting and the evolution of layer deformation were derived. This study found that the permanent deformation within asphalt concrete does not increase with an increase in pavement thickness once the pavement is sufficiently thick. Additionally, most pavement rutting is caused by the deformation of the asphalt concrete, with about half the amount of rutting observed within the top four inches of the pavement layers and only around ten percent of rutting observed in the subgrade.</p> <p>A guideline was developed to calibrate the MEPDG prediction models using a database that contains both APT sections and field roadway segments and accounts for the rutting in individual pavement layers. A procedure was developed to provide the most faithful simulations of the APT conditions using virtual weather station generation, special traffic configuration, and falling weight deflectometer evaluation. The accuracy of the MEPDG's prediction models was improved after the calibration process. The sum of squared error and the standard error of estimates between the predicted and actual measurements were reduced. No significant difference was found between the predicted and actual total asphalt concrete layer rutting and subgrade rutting at the 95 percent confidence level. Model validation using a jack-knife resampling technique confirmed that the calibrated models are able to provide accurate and statistically sound performance predictions. New calibration factors of the MPEGD rutting model from this study have been successfully implemented by the INDOT design team since 2017.</p>			
17. Key Words MEPDG, local calibration, rutting performance model, accelerated pavement testing, rutting distribution		18. Distribution Statement No restrictions. This document is available to the public through the National Technical Information Service, Springfield, VA 22161.	
19. Security Classif. (of this report) Unclassified	20. Security Classif. (of this page) Unclassified	21. No. of Pages 75	22. Price

EXECUTIVE SUMMARY

EFFICIENT PAVEMENT THICKNESS DESIGN FOR INDIANA

Introduction

Over the past several decades, a dramatic increase in traffic volume, axle loads, and tire pressure has led to rapidly deteriorated pavements in the United States. Several types of pavement surface distresses have been noted by many state agencies across the country. Among these distresses, permanent deformation, also known as rutting, is one of the most serious forms of flexible pavement distress. This research investigates the fundamentals of rutting behavior for full-depth flexible pavements. The scope incorporates an experimental study using full-scale accelerated pavement tests (APTs) to monitor the evolution of the transverse profiles of each pavement structural layer. The findings were then employed to improve the rutting model that is embedded in the current pavement design method, the Mechanistic-Empirical Pavement Design Guide (MEPDG).

Findings

Four APT sections were constructed using two typical pavement structures and two types of surface course material. A mid-depth rut monitoring and automated laser profile system was designed to reconstruct the transverse profiles at each pavement

layer interface throughout the process of accelerated pavement deterioration that is produced during the APT. The contributions of each pavement structural layer to rutting and the evolution of layer deformation were derived. This study found that the permanent deformation within asphalt concrete does not increase with an increase in pavement thickness once the pavement is sufficiently thick. Additionally, most pavement rutting is caused by the deformation of the asphalt concrete, with about half the amount of rutting observed within the top four inches of the pavement layers and only around 10 percent of rutting observed in the subgrade.

Implementation

A guideline was developed to calibrate the MEPDG prediction models using a database that contains both APT sections and field roadway segments and accounts for the rutting in individual pavement layers. A procedure was developed to provide the most faithful simulations of the APT conditions using virtual weather station generation, special traffic configuration, and falling weight deflectometer evaluation. The accuracy of the MEPDG's prediction models was improved after the calibration process. The sum of squared error and the standard error of estimates between the predicted and actual measurements were reduced. No significant difference was found between the predicted and actual total asphalt concrete layer rutting and subgrade rutting at the 95 percent confidence level. Model validation using a jackknife resampling technique confirmed that the calibrated models are able to provide accurate and statistically sound performance predictions.

CONTENTS

1. INTRODUCTION AND BACKGROUND	1
1.1 Background	1
1.2 Framework of the MEPDG Design Method	2
1.3 MEPDG Calibration	4
1.4 Accelerated Pavement Testing Techniques	6
1.5 Problem Statement	8
1.6 Scope of Study	9
2. RESEARCH APPROACH	9
2.1 Research Objectives	9
2.2 Testing Plan	9
3. FULL-SCALE ACCELERATED PAVEMENT TESTING	10
3.1 Introduction	10
3.2 Test Lanes Design	10
3.3 Test Lanes Construction and Instrumentation	11
3.4 Determination of Testing Parameters	25
3.5 Test Results and Interpretation	27
4. MEPDG INPUT PREPARATION	39
4.1 Introduction	39
4.2 Field Section Selection	39
4.3 Climate Data	40
4.4 Traffic Data	42
4.5 Material Characterization	43
4.6 Distress Survey	45
4.7 Conditions Simulation	45
5. MEPDG CALIBRATION	46
5.1 Introduction	46
5.2 Evaluation of Local Bias from Global Calibrated Model	46
5.3 Elimination of Local Bias and Dispersion	47
5.4 Model Validation	48
6. CONCLUSIONS AND RECOMMENDATIONS	54
6.1 Summary	54
6.2 Conclusions	54
6.3 Recommendations	54
REFERENCES	55
APPENDICES	
Appendix A. Instrumentation Plan	58
Appendix B. Accelerated Pavement Test Load Application History	61
Appendix C. Material Inputs	64
Appendix D. Distress Data	68

LIST OF TABLES

Table	Page
Table 3.1 Mixtures Design Summary	11
Table 3.2 Mix Design Parameters	13
Table 3.3 Construction Sequence	13
Table 3.4 Dynamic Cone Penetration Test Results	15
Table 3.5 Light-Weight Deflectometer Test Results	16
Table 3.6 Initial Gauge Responses	19
Table 3.7 Profile Measurement Plan	22
Table 3.8 Material Properties for Finite Element Model	24
Table 3.9 Pavement Temperatures	27
Table 3.10 Load Calibration Data	28
Table 3.11 Permanent Deformation Summary	32
Table 3.12 Layer-Wise Permanent Deformation Distribution	37
Table 3.13 FWD Testing Temperatures for Lane 1 and Lane 4	37
Table 4.1 Roadway Segments: 1–3	40
Table 4.2 Roadway Segments: 4–6	40
Table 4.3 Roadway Segments: 7–9	41
Table 4.4 Roadway Segments: 10–13	41
Table 4.5 Weather Stations for Roadway Segments	42
Table 4.6 Data Requirements for HMA Mixture Volumetric and Thermal Properties	43
Table 4.7 Data Requirements for HMA Mixture Mechanical Properties	44
Table 5.1 Summary of Statistical Parameters	48
Table 5.2 Combinations of β_{r2} and β_{r3}	49
Table 5.3 Selected Calibration Coefficients	50
Table 5.4 Statistics for Global and Local Models	52
Table 5.5 Statistics for Global and Local Models and Validation	53
Table B.1 Load Application History of Lane 1	61
Table B.2 Load Application History of Lane 4	62
Table B.3 Load Application History of Lane 3	63
Table C.1 Material Inputs for 1 APT Lane 1	64
Table C.2 Material Inputs for 2 APT Lane 3	64
Table C.3 Material Inputs for 3 APT Lane 4	65
Table C.4 Material Inputs for 4 Previous APT Lane 1	65
Table C.5 Material Inputs for 4 Previous APT Lane 2	65
Table C.6 Material Inputs for 6 SR-43 25550	66
Table C.7 Material Inputs for 7 SR-28 27265	66
Table C.8 Material Inputs for 8 US-41 28441	66
Table C.9 Material Inputs for 9 SR-43 29399	66
Table C.10 Material Inputs for 10 US-40 29133	67

Table C.11 Material Inputs for 11 I-465 29137	67
Table C.12 Material Inputs for 12 US-421 29320	67
Table C.13 Material Inputs for 13 US-31 29310	67

LIST OF FIGURES

Figure	Page
Figure 1.1 Typical repeated load permanent deformation behavior of pavement materials	1
Figure 1.2 Typical rutting diagrams	2
Figure 1.3 MEPDG design process	3
Figure 1.4 Accelerated pavement test facilities	7
Figure 2.1 Research approach flow chart	9
Figure 3.1 APT loading machine and empty test pit	10
Figure 3.2 Accelerated pavement test section layout	10
Figure 3.3 Test section structures	11
Figure 3.4 Aggregate gradation for surface SMA mix	12
Figure 3.5 Aggregate gradation for surface dense mix	12
Figure 3.6 Aggregate gradation for intermediate/base mix	12
Figure 3.7 Aggregate gradation for open-graded mix	13
Figure 3.8 Subgrade construction	14
Figure 3.9 (a) Dynamic cone penetrometer and (b) light-weight deflectometer testing	15
Figure 3.10 Locations of dynamic cone penetrometer and light-weight deflectometer tests on subgrade soil	15
Figure 3.11 Asphalt concrete layer construction	17
Figure 3.12 Asphalt strain gauges	18
Figure 3.13 Geokon model 3500 earth pressure cell	18
Figure 3.14 (a) 5TM Soil Moisture & Temperature Sensor and (b) thermocouple	18
Figure 3.15 Sensors at the subgrade surface	20
Figure 3.16 Sensors at the lower base layer surface	20
Figure 3.17 Sensors at the open-graded (OG) layer surface	21
Figure 3.18 Laser profile system components	21
Figure 3.19 Automated laser profile system	21
Figure 3.20 Reference system	21
Figure 3.21 Transverse surface profile locations	22
Figure 3.22 Rutted sample	22
Figure 3.23 Longitudinal cross-section view of monitoring holes in pavement structure	23
Figure 3.24 Construction of monitoring holes	23
Figure 3.25 Laser measurements of monitoring holes	24
Figure 3.26 Contour plots for vertical stress	25
Figure 3.27 Vishay Micro-Measurements System 6000	25
Figure 3.28 Falling weight deflectometer and test set-up	26
Figure 3.29 Falling weight deflectometer test locations	26
Figure 3.30 Pavement temperatures	27
Figure 3.31 (a) Heating lamp placement and (b) thermal image of heated test lane	27
Figure 3.32 (a) Applied load calibration and (b) tire footprint	28
Figure 3.33 Load calibration data	28
Figure 3.34 APT load speed record	29

Figure 3.35 Sample transverse profile	29
Figure 3.36 Definition of rut depth	29
Figure 3.37 Lane 1 permanent deformation evolution	30
Figure 3.38 Lane 4 permanent deformation evolution	31
Figure 3.39 Lane 3 permanent deformation evolution	32
Figure 3.40 Lane 1 mid-depth ruts	33
Figure 3.41 Lane 4 mid-depth ruts	34
Figure 3.42 Lane 1-layer permanent deformation and permanent strain	35
Figure 3.43 Lane 4-layer permanent deformation and permanent strain	35
Figure 3.44 Lane 3 mid-depth ruts	36
Figure 3.45 Lane 3-layer permanent deformation and permanent strain	37
Figure 3.46 Falling weight deflectometer deflections at Lane 1	38
Figure 3.47 Falling weight deflectometer deflections at Lane 4	38
Figure 3.48 Back calculated asphalt concrete layer moduli	39
Figure 4.1 Roadway segment locations	42
Figure 4.2 Rut depth measurements from SR-43-25550	45
Figure 4.3 MEPDG simulated aging effect for APT Lane 4	46
Figure 5.1 (a) Predicted rut depths, and (b) prediction residual errors of total rut depth for global model	47
Figure 5.2 (a) Predicted rut depths, and (b) prediction residual errors of asphalt concrete layer rut depth for global model	47
Figure 5.3 (a) Predicted rut depths, and (b) prediction residual errors of subgrade rut depth for global model	48
Figure 5.4 Calibration and validation flowchart	49
Figure 5.5 SSEs between predicted and measured asphalt concrete layer rut depths	50
Figure 5.6 (a) Predicted rut depths, and (b) prediction residual errors of total rut depth for global and local models	50
Figure 5.7 (a) Predicted rut depths, and (b) prediction residual errors of asphalt concrete layer rut depth for global and local models	51
Figure 5.8 (a) Predicted rut depths, and (b) prediction residual errors of subgrade rut depth for global and local models	51
Figure 5.9 (a) Predicted rut depths, and (b) prediction residual errors of total rut depth for calibration and validation	52
Figure 5.10 (a) Predicted rut depths, and (b) prediction residual errors of asphalt concrete layer rut depth for calibration and validation	52
Figure 5.11 (a) Predicted rut depths, and (b) prediction residual errors of subgrade rut depth for calibration and validation	53
Figure A.1 Plan view of the intermediate layer surface	58
Figure A.2 Plan view of the upper base layer surface	58
Figure A.3 Plan view of the open-graded layer surface	59
Figure A.4 Plan view of the lower base layer surface	59
Figure A.5 Plan view of the subgrade surface	60
Figure A.6 Plan view of the original surface	60
Figure D.1 Rut depth measurements from 6 SR-43-25550	68
Figure D.2 Rut depth measurements from 7 SR-28-27265	68
Figure D.3 Rut depth measurements from 8 US-41-28441	68
Figure D.4 Rut depth measurements from 9 SR-43-29399	68
Figure D.5 Rut depth measurements from 10 US-40-29133	68
Figure D.6 Rut depth measurements from 11 I-465-29137	68
Figure D.7 Rut depth measurements from 12 US-421-29320	69
Figure D.8 Rut depth measurements from 13 US-31-29310	69

1. INTRODUCTION AND BACKGROUND

1.1 Background

As an economical, durable, and recyclable material that also provides smooth, quiet, and attractive road surfaces, asphalt concrete has been used to cover more than 94 percent of the paved roads in the United States since it was first used to pave a roadway by Belgian chemist Edmund J. DeSmedt in 1870. To ensure that asphalt concrete pavement, also known as flexible pavement, performs well in the field, the pavement must be designed properly in terms of structure and material. Since the first transcontinental highway, the Lincoln Highway, was built across the United States at the beginning of the 20th century, pavement design has always been a challenging task. Pavement design engineers are inevitably faced with a great variety and uncertainty of design factors, such as the environment, construction materials, and traffic load, which fluctuate greatly due to climate, technology, economic growth, and population changes.

The first comprehensive pavement design method used throughout the United States was developed under the auspices of the American Association of State Highway and Transportation Officials (AASHTO). The 1993 AASHTO design method is an empirical approach based on Ottawa, Illinois road tests conducted in the late 1950s and early 1960s (AASHTO, 1993). This design method, which has been updated periodically, has served well over the intervening years, but it does have limitations. For example, the AASHTO method is based on only one set of environmental conditions, those of Ottawa, Illinois, one set of construction materials, and limited traffic loading. These shortcomings have motivated researchers to develop more advanced design methods.

In 1996, the National Cooperative Highway Research Program (NCHRP) and AASHTO initiated two research projects, NCHRP 1-37A and NCHRP 1-40, to develop a new pavement design approach based on more mechanistic methods (Applied Research Associates, Inc., 2004). The result of these projects was the Mechanistic-Empirical Pavement Design Guide (MEPDG). The underlying principle of the mechanistic-empirical design approach is to use mechanical responses of the pavement to the environment and traffic loading to predict the pavement's functional responses. This approach was first suggested by Kerkhoven and Dorman (1953) using the vertical compressive strain at the top of the subgrade as the critical indicator to predict permanent deformation and by Saal and Pell (1960) using the horizontal tensile strain at the bottom of the asphalt layer as the critical indicator to predict fatigue cracking. The mechanistic-empirical approach to pavement design has been discussed in detail by Thompson et al. (1990).

Over the past several decades, a dramatic increase in traffic volume, axle loads, and tire pressure has led to rapidly deteriorated pavements in the United States. Several types of pavement surface distresses have been noted by many state agencies across the country

(Brown & Cross, 1992; Monismith et al., 1994). Among these distresses, permanent deformation, also known as rutting, is one of the most serious forms of flexible pavement distress. In terms of public and vehicle safety concerns, rutting is considered a hydroplaning safety hazard by many state departments of transportation (DOTs). Rutting can be hazardous not only for vehicles and for passengers, but it also damages the pavement itself. When water accumulates in the ruts, it often penetrates the pavement structure and further deteriorates the pavement (White, Haddock, Hand, & Fang, 2002).

Rutting is a result of the permanent strain accumulation that is caused by repeated load applications. El-Basyouny (2005) stated that the evolution of permanent deformation in pavement material can be characterized as three distinct stages, as shown in Figure 1.1. The primary stage consists predominantly of volumetric change with a decreasing rate of deformation; high initial densification occurs during this stage. The secondary stage is characterized by a combination of densification and shear deformation; a small but constant rate of deformation occurs during this stage. Finally, the tertiary stage always exhibits a high rate of rutting that is caused mostly by shear deformation. Pavement design and analysis methods typically do not consider the tertiary deformation stage, but rather only the primary and secondary deformation stages, because the laboratory testing required to reach tertiary stage permanent deformation, and thus identify permanent deformation material characteristics, is extremely time consuming. In addition, the degree of permanent deformation in the tertiary stage is so large that pavements would be considered as having failed long before reaching this stage.

Rutting usually is manifested by depressions along the wheel paths and sometimes causes uplifted material between and outside the wheel paths, as shown in Figure 1.2. The two major causes of rutting are permanent deformation in the subgrade, as shown in Figure 1.2 (a), and permanent deformation in one or more of the asphalt layers, typically the surface layer, as shown in Figure 1.2 (b).

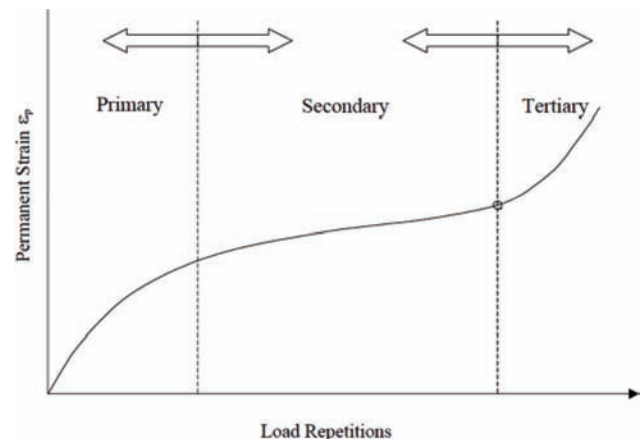


Figure 1.1 Typical repeated load permanent deformation behavior of pavement materials (El-Basyouny, 2005).

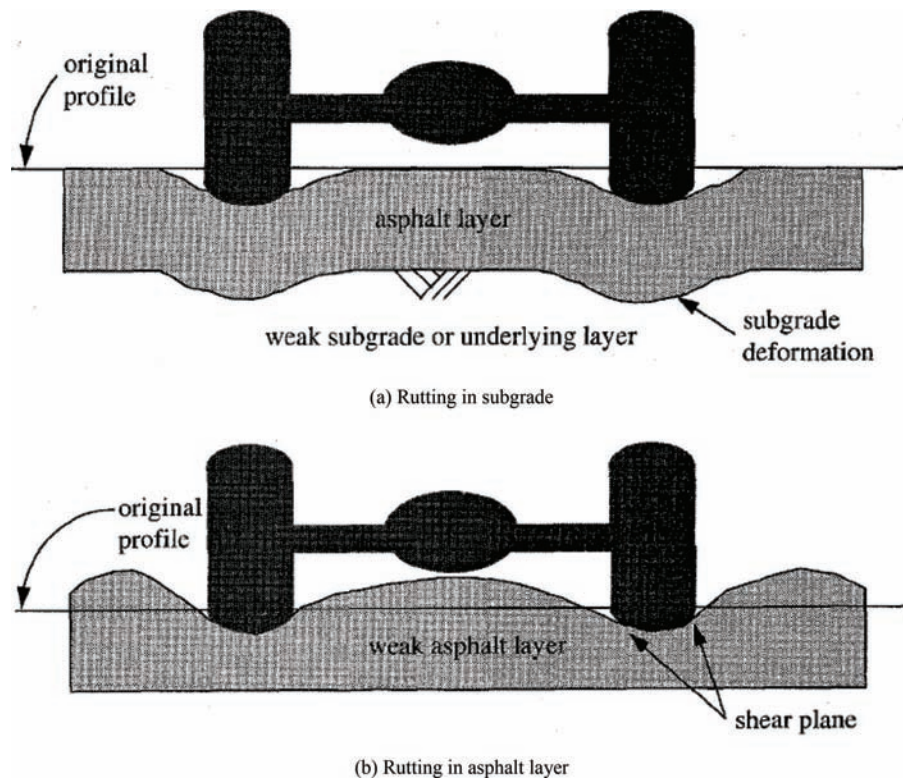


Figure 1.2 Typical rutting diagrams (McGennis, Anderson, Kennedy, & Solaimanian, 1995).

Permanent deformation of the subgrade is usually due to the insufficient thickness of one or more of the pavement layers or excessive moisture in the subgrade. Permanent deformation of an asphalt layer usually is caused by a combination of consolidation (densification) and shear deformation. Consolidation is a result of insufficient compaction during construction; the material changes volume and experiences a reduction in air voids due to traffic loading. Shear deformation is considered the dominant behavior that causes an asphalt surface layer to deform permanently and is characterized by the downward and lateral movement of the asphalt mixture layer, which causes shape distortion in the pavement (Brown & Cross, 1992).

To reveal the fundamentals of pavement rutting behavior, it is critical to investigate the origins of hot mix asphalt (HMA) permanent deformation failure. Researchers and pavement and material engineers have been performing trench cutting and coring, and using instrumentation such as multi-depth deflectometers (MDDs) to determine the contribution of the pavement's structural layers to the rutting of flexible pavement (Bonaquist & Mogawer, 1997; Brown & Cross, 1989; Gautreau, Zhang, & Wu, 2008; Harvey & Popescu, 2007; Kim, 2004; Zhou & Scullion, 2002). However, these methods have limitations, such as high costs, lack of accuracy, and damage to pavements. For example, trench cutting and coring are destructive test methods and can lead to inaccurate results. Furthermore, they provide rutting only at the end of the pavement's service life rather than throughout the entire evolution of

rutting development. Moreover, MDD sensors are expensive and have accuracy problems due to the relative movement between the MDD sensor and the pavement.

If not only the amount of deformation but also the complete profile at each structural layer interface could be monitored closely during the process of pavement deterioration, the resulting data would be valuable information to help understand the mechanisms of rutting behavior. In addition, such information would be a great source to validate the basic assumptions of current design methods.

1.2 Framework of the MEPDG Design Method

Figure 1.3 presents the general approach for the MEPDG design process. As the figure indicates, the method uses environmental, traffic loading, and materials properties as inputs, calculates the pavement mechanical responses given these inputs using mechanistic models, and then employs various transfer functions (i.e., empirical models) to predict pavement distresses, such as rutting and fatigue cracking.

The development of the input values (Stage 1) is a key step in the design process. A hierarchical input approach is applied in the MEPDG for traffic, materials, and existing pavement conditions. The hierarchical input levels are as follows.

- Level 1 requires the greatest knowledge about the input values and depends on site-specific laboratory tests.

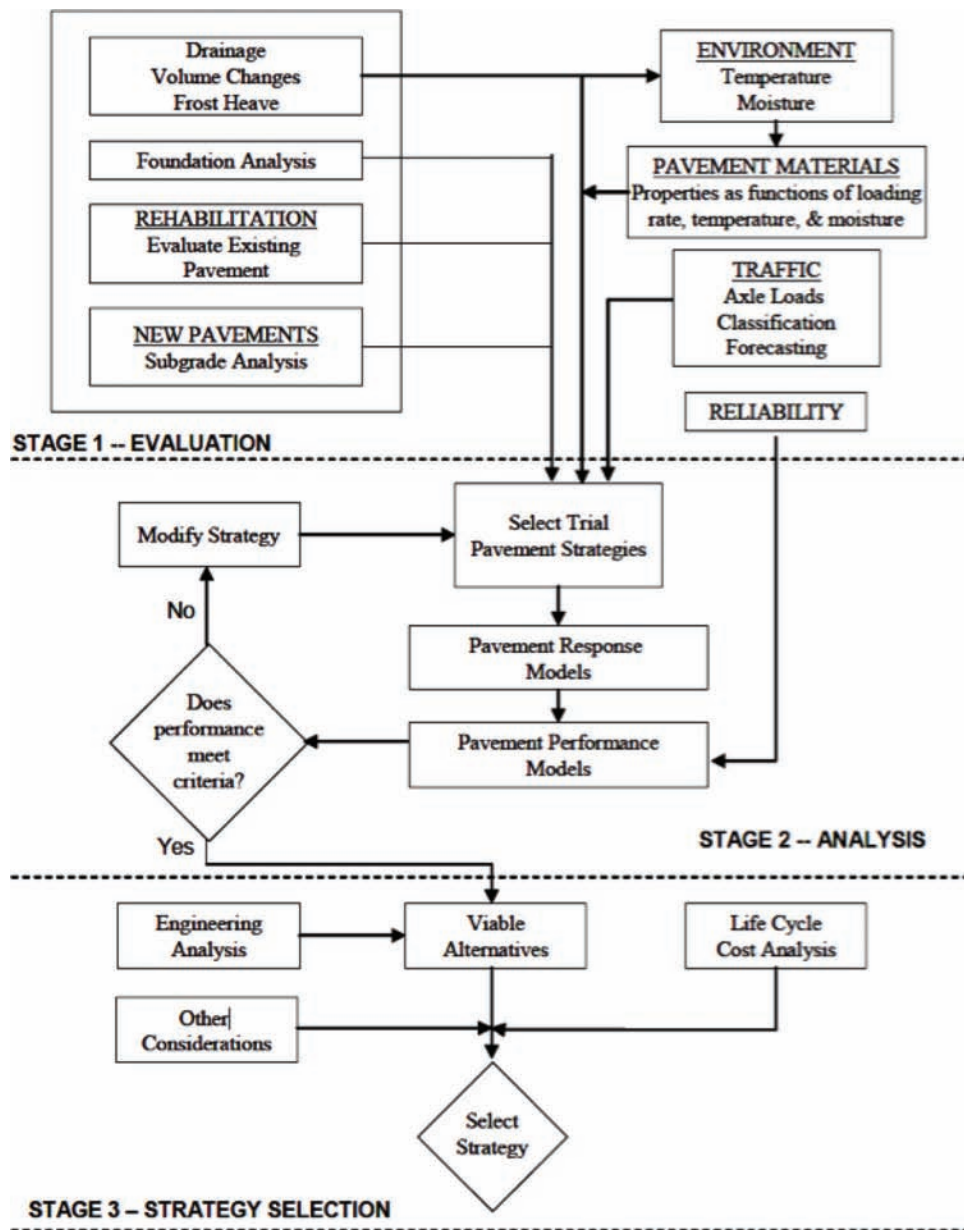


Figure 1.3 MEPDG design process (Applied Research Associates, Inc., 2004).

- Level 2 uses empirical correlations to estimate the required parameters. Data collection and experiment requirements are much simpler than for Level 1.
- Level 3 uses national or regional default values.

The impact of the environment is taken into account through an embedded climatic model called the Enhanced Integrated Climatic Model (EICM). Using climatic data that come from weather stations across the country, this model predicts the pavement layer temperature and moisture content on an hourly basis. This information is used to derive the evolution of the material properties throughout the pavement design life.

Stage 2 of the MEPDG method is the performance analysis of the pavement design. The design process is

iterative and begins with an initial trial design, developed based on either engineering judgment or a previous design method such as the AASHTO 1993 design guide. The trial design is analyzed incrementally over a user-defined design life using multilayer linear elastic analysis, specifically, the Jacob Uzan Linear Elastic Analysis (JULEA) program, to determine the development of the strains that are due to traffic and environment loading. Empirical transfer functions correlate the mechanical responses with the pavement's damage and distress. If the accumulated damage and distress values are predicted to be higher than the allowable user-defined design criteria, then modifications are made to the pavement cross-section and the MEPDG is executed again until satisfactory predicted pavement performance is obtained.

The third stage of the design process includes the evaluation of structurally viable alternatives, cost considerations, and life-cycle cost analysis. The MEPDG software does not include these functions, but rather they are the responsibility of the design engineer.

The focus of the proposed research is the MEPDG rutting transfer functions for flexible pavements. As mentioned, flexible pavement can undergo rutting by permanent deformation either in the subgrade or in the asphalt layer. The MEPDG utilizes two separate transfer functions to describe the permanent deformation that develops in the unbound material layer and the asphalt layer.

The transfer function for the unbound material layer, as shown in Equation 1.1, was first developed by Tseng and Lytton (1989) and later modified by Ayres (1997) and El-Basyouny (2005). The model is an empirical correlation based on permanent deformation test results obtained from a modified resilient modulus test procedure. The model estimates permanent deformation in the unbound material layer based on output from the MEPDG mechanistic model, such as vertical resilient strain, and output from the EICM, such as moisture content.

$$\delta_a(N) = \beta_{s1} k_1 \varepsilon_v h \left(\frac{\varepsilon_0}{\varepsilon_r} \right) e^{-\left(\frac{\rho}{\beta}\right)^\beta} \quad (1.1)$$

where:

δ_a = permanent deformation for a given layer;

N = number of load repetitions;

β_{s1} = calibration factor;

k_1 = 2.03 for granular material, 1.35 for fine-grained material;

ε_v = vertical resilient strain in the layer as obtained from a mechanistic model;

ε_r = resilient strain imposed in a laboratory test to obtain material properties;

h = layer thickness; and

$\varepsilon_0, \rho, \beta$ = material properties, which are correlated with the layer water content and layer resilient modulus; detailed discussion can be found in Tseng and Lytton (1989).

The transfer function for asphalt layers was first developed by Leahy (1989) and utilizes more than 250 asphalt mixture specimens that represent three binder contents, three stress levels, two binder types, three temperatures, and two aggregate types. Ayres (1997) and Kaloush and Witeczak (2000) completed work to modify the Leahy model, significantly expanding its data range. The transfer function, as used in the MEPDG, is shown in Equation 1.2.

$$\frac{\varepsilon_p}{\varepsilon_r} = K_Z \beta_{r1} 10^{k_{r1}} (T)^{k_{r2}} \beta_{r2} (N)^{k_{r3}} \beta_{r3} \quad (1.2)$$

where:

ε_p = incremental plastic strain at the mid-depth of a thickness increment;

ε_r = resilient strain calculated at the mid-depth of a thickness increment;

T = temperature at the mid-depth of a thickness increment (8F);

N = number of axle load applications of a specific axle type and load interval within a specific time period;

$\beta_{r1}, \beta_{r2}, \beta_{r3}$ = local calibration coefficients, all equal to one for globally calibrated model;

k_{r1} = plastic deformation factor, equal to 3.35412 based on the global calibration effort;

k_{r2} = plastic deformation factor related to the effect of temperature, equal to 1.5606 based on the global calibration effort;

k_{r3} = plastic deformation factor related to the effect of wheel loads, equal to 0.4791 based on the global calibration effort; and

K_Z = depth function.

The depth function, K_Z is used to consider the variation in stress level in terms of depth. It is a function of depth and asphalt layer thickness, as shown in Equations 1.3, 1.4, and 1.5.

$$K_Z = (C_1 + C_2 D)(0.328196)^D \quad (1.3)$$

$$C_1 = -0.1039 H_{HMA}^2 + 2.4868 H_{HMA} - 17.342 \quad (1.4)$$

$$C_2 = 0.0172 H_{HMA}^2 - 1.7331 H_{HMA} + 27.428 \quad (1.5)$$

where:

D = depth to the mid-depth of the thickness increment (sublayer); and

H_{HMA} = asphalt layer thickness.

The plastic deformation factors, k_{r1}, k_{r2}, k_{r3} , are material-dependent coefficients obtained from repeated load permanent deformation tests. The data are plotted in a log-log domain, and k_{r3} is the slope in the secondary stage, k_{r1} is the intercept, and k_{r2} is the effect of temperature on the intercept.

Each pavement structural layer can be subdivided. An appropriate transfer function is employed for the calculation within each sublayer. In this way, variations in loading frequency, temperature, and moisture content can be taken into account.

1.3 MEPDG Calibration

1.3.1 Terminology and Concepts

1.3.1.1 Calibration. The overall goal of the MEPDG calibration process is to adjust pavement performance transfer functions systematically so that the MEPDG can predict pavement performance without bias and be used to determine the standard error associated with the transfer functions. Two statistical measures are used to evaluate the goodness-of-fit between the predicted and observed values: bias and precision.

Bias describes the effect of distorting the simulations systematically. Within the scope of MEPDG calibration, bias is defined as the residual error between the predicted and observed values that cause the simulation to overestimate (i.e., when bias is positive) or underestimate

(i.e., when bias is negative) pavement performance. The objective term used in the optimization process during MEPDG calibration is the sum of squared error (SSE) instead of bias.

Precision describes the ability of the transfer function to predict repeatedly the distresses that strongly correlate with the observations. Precision is defined as the standard error of the estimate (s_e), i.e., the standard deviation of the residual error. Unlike the case for bias, lack of precision leads to inconsistent predictions and can be identified as scatter when plotting the observed and predicted values. Lack of precision has four major sources (AASHTO, 2010):

1. *Measurement error* occurs when the distress is measured in the field. The measured distress is merely an estimate of the true mean of the roadway segment. Measurement error can be lessened by increasing the number of measurements within a roadway segment.
2. *Input error* is associated with the input parameters that describe the material properties, traffic, and climate. Input error depends highly on the input level.
3. *Model error or lack-of-fit error* stems from the inability or deficiencies of a model to simulate real-world conditions, such as transfer functions, EICM data, Global Aging System (GAS) data, multilayer linear elastic analysis, etc.
4. *Pure error* is defined as the random variation between the distresses of two 'identical' roadway segments.

1.3.1.2 Validation. Validation is necessary because it assesses the capability of the calibrated transfer functions to produce robust and accurate predictions of pavement performance. A successful validation can be achieved if the bias and precision statistics obtained from the validation process are similar to those obtained from the calibration process, or, alternatively, a statistical test should be performed with the null hypothesis that no significant difference exists between the predicted and observed values.

1.3.2 Calibration/Validation Techniques

Validation typically requires an additional set of roadway segments that is independent of the set used for the calibration. Different sampling techniques can improve the accuracy and confidence of the calibrated models. Two sampling/resampling approaches recommended by AASHTO (2010) are described here: the split-sample approach and the jackknife resampling approach.

For the split-sample approach, during the calibration/validation process only a portion of the roadway segments is used for calibrating the transfer functions, while the remainder is used for validation. Typically, 80 percent of the roadway segments are used for calibration and 20 percent for validation. The major limitation of this approach is that it requires a large number of roadway segments, which is not normally available in practice.

The jackknife approach is taken when only a small sample size is available. For an $n - 1$ jackknife validation, a sample with n roadway segments is first divided into two groups. One group has $n - 1$ segments that are used for the model calibration, and then the calibrated model is applied to the remaining segment from which the standard error (e_1) is calculated. Next, another segment is withheld from n roadway segments and the new $n - 1$ segments are used for the model calibration. The calibrated model is applied to the withheld segment for the standard error (e_2) calculation. This process is repeated until all n segments have been withheld and n values of standard error are obtained. Those standard errors can be used to calculate the jackknife statistics.

1.3.3 Global Calibration

When the MEPDG was first designed as part of NCHRP Project 1-37A, in order to confirm that the embedded transfer functions could deliver reasonable accuracy in predicting actual pavement performance, the project's research team used more than 100 sections in the Long-Term Pavement Performance (LTPP) database to calibrate the MEPDG. The dataset that was used in this process covered a wide range of subgrades, structures, climates, and traffic throughout North America (Applied Research Associates, Inc., 2004).

However, each state has its own pavement maintenance and preservation strategies and construction and material specifications. These various factors have a great influence on the predicted pavement performance and were not considered in the global calibration process for the MEPDG. In addition, newly developed materials and mix design methods that are now commonly used by industry were not available in the LTPP program for global calibration. These more recent materials and mix design methods include, for example, the Superpave mix design method, stone matrix asphalt (SMA), warm-mix asphalt (WMA), and polymer-modified asphalt. As recommended by the research team of NCHRP Project 1-37A, each state should locally calibrate the embedded transfer functions prior to implementation of the MEPDG in order to address these factors.

1.3.4 Local Calibration

The efforts undertaken by several states' DOTs in calibrating the MEPDG are summarized in the following paragraphs.

The Arizona DOT conducted local calibration for MEPDG v. 1.0 in 2010. Three flexible pavement transfer functions for fatigue cracking, rutting, and roughness were calibrated. According to the Arizona calibration results, the global model underpredicted fatigue cracking and rutting in asphalt concrete layers and overpredicted rutting in the subgrade (Souliman, Mamlouk, El-Basyouny, & Zapata, 2010).

The Arkansas State Highway and Transportation Department calibrated MEPDG v. 1.1 using both LTPP program sections and Arkansas State Highway and Transportation Department Pavement Management System (PMS) sections. Alligator cracking and rutting transfer functions were considered in this study. Concerns were reported regarding the data quality during the calibration process. The different definitions of ‘transverse cracking’ between the MEPDG and LTPP program were believed to be critical to the data collection process (Hall, Xiao, & Wang, 2011).

The North Carolina DOT conducted its MEPDG local calibration (i.e., MEPDG v. 1.1) in 2011 using both LTPP and non-LTPP program pavement sections. All of the LTPP program sections were used for calibration and the non-LTPP program sections were used for validation. Material-specific HMA rutting plastic deformation factors were developed for 12 commonly used North Carolina HMA mixtures based on triaxial repeated load permanent deformation tests. Two approaches, i.e., a generalized reduced gradient (GRG) method and a genetic algorithm method, were used as the optimization techniques. Several conclusions were drawn in this study: (1) the MEPDG tends to overpredict rutting, especially in the subgrade; (2) local calibration reduces bias and standard error, but the improvement is not enough, and so, the null hypothesis that no difference exists between the predicted and measured values cannot be accepted at the 95 percent confidence level; and (3) forensic investigation is recommended for future studies to quantify the contribution of each layer to total rutting (Kim, Jadoun, Hou, & Muthadi, 2011).

The Nevada DOT started MEPDG implementation in 2005. It recently has conducted local calibration of the fatigue cracking and rutting models in the Pavement ME v. 2.0 (i.e., the current version of the MEPDG) using Nevada’s local PMS database. A materials database consisting of field-produced mixtures, mostly polymer-modified binder mixtures, was built, and material properties such as the dynamic modulus and binder properties were tested. Recalibration was recommended for the future to increase the accuracy of the predictions because the calibration method used test sections with only around 10 years of service life (Nabhan, 2015).

The Oregon DOT (ODOT) calibrated Darwin ME v. 1.1 (one version of the MEPDG) in 2013. The research focused on the rehabilitation of existing pavement structures, which is the majority of pavement work conducted by the ODOT. Rutting, alligator cracking, longitudinal cracking, and thermal cracking models were calibrated. The ODOT found that: (1) the MEPDG overpredicted total rutting and that most of the predicted rutting occurred in the subgrade; (2) all of the calibrated models provided less bias and standard error than the global models; and (3) large variations remained between the predicted and observed values, especially for longitudinal and transverse cracking (Williams & Shaidur, 2013).

The Iowa DOT calibrated MEPDG v. 1.1 using jointed plain concrete pavement (JPCP) sections, HMA pavement sections, and HMA over JPCP sections. Required inputs were collected from the Iowa DOT PMS database. JPCP faulting, transverse cracking, roughness, rutting, and fatigue cracking models were calibrated. For flexible pavements, acceptable bias and standard errors were found for the global fatigue cracking model; however, the global rutting model overpredicted the subgrade rutting while underestimating the asphalt concrete layer rutting (Ceylan, Kim, Gopalakrishnan, & Ma, 2013).

1.4 Accelerated Pavement Testing Techniques

1.4.1 Benefits and Impacts

Metcalf (1996) defined the APT as:

The controlled application of a prototype wheel loading, at or above the appropriate legal load limit to a prototype or actual, layered, structural pavement system to determine pavement response and performance under a controlled, accelerated, accumulation of damage in a compressed time period. The acceleration of damage is achieved by increased repetitions, modified loading conditions, imposed climatic conditions (e.g., temperature and/or moisture), the use of thinner pavements with a decreased structural capacity and thus shorter design lives, or a combination of these factors. Full-scale construction by conventional plant and processes is necessary so that real world conditions are modeled (Metcalf, 1996).

APT techniques provide an opportunity to investigate pavement behavior in cost- and time-efficient ways whereby the amount of damage that might take more than 10 or even 20 years to occur in the field can be achieved in a matter of months. Metcalf (1996) summarized a list of 35 full-scale APT facilities around the world. During the past several decades, there has been an increased interest in APTs. APT facilities and methods, such as circular tracks, linear tracks, and mobile loading machines, have been developed worldwide; Figure 1.4 presents several examples.

APT have been used extensively in areas such as:

- The development and validation of pavement analysis and design models
- Research into pavement mechanics and damage mechanisms
- Identification of deficiencies in current practices
- Development of performance-based specifications or tests for asphalt concrete pavements
- Investigations into correlations between laboratory experiments and real long-term pavement performance
- Evaluation of the efficiency and impacts associated with implementing innovative materials, designs, specifications, construction standards, vehicle technology, rehabilitation techniques, etc.
- Evaluation of load damage equivalency and the remaining life of pavements
- Improved vehicle–pavement interaction, including advanced load and contact stress models



(a) National Airport Pavement Test Facility (NAPTF), U.S.



(b) Laboratoire Central des Ponts et Chaussées (LCPC), France



(c) Mobile Load Simulator (MLS), South Africa



(d) HVS Mark IV at Cold Regions Research and Engineering Laboratory (CRREL), U.S.

Figure 1.4 Accelerated pavement test facilities.

1.4.2 Evaluation of Permanent Deformation of Flexible Pavement

Many research studies have been conducted to analyze rutting behavior using APT facilities. Sivasubramaniam and Haddock (2006) evaluated Superpave designed mixtures using the National Center of Asphalt Technology (NCAT) test track and full-scale APT and PURWheel laboratory wheel trackers. Saeed, Hammons, and Bianchini (2010) compared the rutting performance of a SMA mixture and dense-graded airfield HMA mixture under an F-15E aircraft load cart. They found the SMA mixture to have much better rutting resistance than the HMA mixture. Villiers, Roque, and Dietrich (2005) evaluated the contribution of pavement layers to total rut depth using a falling weight deflectometer (FWD) test and transverse profiles. They also validated their findings with a forensic trench study. Gibson, Li, and Kutay (2010) studied the rutting susceptibility of mixtures compacted with a Superpave Gyrotory Compactor (SGC) and field compaction rollers. They found that the SGC-compacted mixtures exhibited a higher rate of rutting development in the early stage of loading whereas the rate tended to decrease when the loading was continued.

Several mechanistic or mechanistic-empirical models have been developed using the APT method. Monismith, Popescu, and Harvey (2006) and Li, Lee, and Lee (2011) developed a relationship between rutting and mixture shear properties obtained from triaxial compressive strength and repeated load permanent deformation tests. Park, Martin, and Masad (2004) developed an elasto-viscoplastic model based on Perzyna's viscoplastic theory and the Druker-Prager yield function

to predict rutting measured in APTs. Mbakisy and Romanoschi (2010) evaluated three mechanical models, namely, the Druker-Prager, elasto-viscoplastic, and creep models for rutting prediction. Immanuel and Timm (2007) developed two mechanistic-empirical models using NCAT test track data; one model is based on the vertical strain on top of a granular layer and the other is based on the maximum shear strain in the HMA layer. Both models exhibited reasonable accuracy. Xu and Mohammad (2008) developed a mechanistic-empirical model that uses power law and vertical strain and conducted their tests at the Louisiana Accelerated Load Facility (ALF).

1.4.3 MEPDG Analysis

Azari, Mohseni, and Gibson (2008) validated the MEPDG rutting models using both Level 1 and Level 3 inputs with Federal Highway Administration Accelerated Loading Facility (FHWA ALF) data. They found that both Level 1 and Level 3 simulations overpredicted the rutting.

Gibson et al. (2008) analyzed FHWA ALF tests using the MEPDG. They used special axle configuration features in the MEPDG to customize their super-single tire assembly. They employed a surrogate of the MEPDG to bypass various MEPDG features, such as the inherent climate model and global aging system, which challenged the ability to simulate ALF testing conditions.

Hong and Chen (2008) calibrated the MEPDG rutting model using data obtained from eight sections tested at the Cold Regions Research and Engineering Laboratory (CRREL). These researchers simulated APT

traffic by constructing a special vehicle that has only one tandem axle in the MEPDG. The spacing between the two axles was set above 100 inches so that one repetition in the MEPDG equals two passes in the APT. Hong and Chen (2008) conducted the optimization process by considering the entire history of rutting development instead of only the final rut depth measured at the end of the pavement service life.

1.5 Problem Statement

As a replacement for the 1993 AASHTO design method, the MEPDG has been adopted by state agencies since 2005. After ten years of implementation, over 30 states use the MEPDG as their primary tool to design and analyze their pavements. When the MEPDG was first developed, transfer functions, including the rutting transfer function, were calibrated globally using data from the Long-Term Pavement Performance (LTPP) database (Applied Research Associates, Inc., 2004). This database, initiated in 1991, contains data from more than 2,500 test sections scattered throughout North America. The LTPP program collects data from these pavement test sites that include inventory, distress, rehabilitation, materials testing, traffic, and climate information (Elkins, Tompson, Simpson, & Ostrom, 2012).

Although it is understandable that the MEPDG development team globally calibrated the rutting transfer functions, the global calibration factors almost certainly do not properly reflect local conditions. Furthermore, when the MEPDG was first calibrated using the LTPP database, newly developed mix design methods, such as the Superpave mix design method, and nonconventional mixtures, such as stone matrix asphalt (SMA), were not incorporated into the database. The discrepancies between global and local conditions, old and new mixture design methods, and conventional and nonconventional mixtures can introduce bias and errors into distress predictions.

In fact, several state DOTs have reported significant bias and variance between predictions obtained from globally calibrated transfer functions and those calibrated locally. Additionally, the MEPDG practice manual (AASHTO, 2008) encourages local calibration of the transfer functions prior to implementation of the MEPDG. Given others' experiences and the guidance provided in the practice manual, it seems prudent to calibrate the MEPDG rutting transfer functions using local data prior to the adoption and use of the MEPDG in designing pavements for a local area.

When the Indiana DOT (INDOT) initiated a local calibration project, it encountered several challenges. The MEPDG practice manual (AASHTO, 2008) suggests that some of the test sections used for local calibration should exhibit a level of distress that is at least 50 percent of the design criterion. For example, if the maximum allowable rutting depth design criterion is 0.5 inch, then the pavement sections used for local calibration should display at least 0.25 inch of rutting.

If this action is not taken, the accuracy and bias of the predictions obtained from the transfer functions might not be well defined at the trigger values for pavement failure. However, finding asphalt pavements that met this 50 percent distress level and that were designed and built using the Superpave asphalt mixture design method was problematic.

Indiana began implementing the Superpave asphalt mixture design method around 2000 and has used the method ever since. Thus, to complete local calibration of the MEPDG rutting transfer functions, only asphalt pavements containing Superpave designed mixtures should be used. A preliminary search of the Indiana roadway inventory indicated that most of the full-depth flexible pavements containing Superpave designed mixtures had been in service for less than ten years and were showing limited rutting distress. This finding is especially true in the case of conventional flexible pavements, which are precisely the types of pavement that the flexible pavement design portion of the MEPDG is supposed to design.

Another challenge in calibrating the rutting transfer functions, as indicated by the MEPDG developers, is the limitation of the rutting transfer functions themselves. These functions were developed using total rut depths measured at the pavement surface, as these data were all that were available from the LTPP database. Trench data, or any other information that could be used to derive layer-wise rutting, were not available (Applied Research Associates, Inc., 2004). Without knowing the individual layer rutting information, it is impossible to calibrate the transfer functions precisely, because there is no way to determine from the data how much of the total rutting occurred in the unbound layer and how much occurred in the asphalt layer. Given this limitation, the MEPDG rutting transfer functions were calibrated globally based on the assumption that the contribution of each of the layers to the total rut depth measured at the surface would be similar to that predicted by the MEPDG. This assumption is widely believed to be questionable, however, and it might be one of the major sources of error in prediction results. Several local calibration efforts have indicated that overprediction was observed when globally calibrated transfer functions were used (Applied Research Associates, Inc., 2004; Hong & Chen, 2008; Kim et al., 2011; Souliman et al., 2010; Von Quintus, Mallela, Bonaquist, Schwartz, & Carvalho, 2012). Several researchers have suggested that this overprediction of total rut depths might be due to the overprediction of subgrade rutting (Kim et al., 2011; Von Quintus et al., 2012).

The accelerated pavement test (APT) could be an ideal tool to overcome most of the aforementioned problems associated with MEPDG local calibration. However, several limitations of the APT must be taken into account. First, the MEPDG simulates realistic environmental conditions based on weather station data and predicts daily and seasonal temperature and moisture variations in pavements, whereas the APT normally has

controlled climate conditions that challenge the most realistic simulations obtained through the MEPDG. Second, the MEPDG simulates more asphalt aging than actually occurs during APTs, as reported by Von Quintus et al. (2012):

To evaluate the rutting evolution from accelerated pavement test (APT) sections with the MEPDG requires that the loads be applied over a longer time period; stretching the load cycles over a longer period of time results in more asphalt aging than actually occurs during the loading cycles for many APT sections. This will result in a negative bias between the predicted and measured rut depths (Von Quintus et al., 2012).

1.6 Scope of Study

This research was initiated with the intent to investigate the fundamentals of rutting behavior for full-depth flexible pavements. The scope incorporates an experimental study using full-scale APT techniques to monitor the evolution of the transverse profiles of each pavement structural layer interface. The findings are then employed to improve the rutting model that is embedded in the current pavement design method, the MEPDG.

2. RESEARCH APPROACH

2.1 Research Objectives

The focus of this study is the permanent deformation of full-depth flexible pavements that have been constructed using a Superpave designed mixture. This type of pavement has the highest priority among INDOT projects. The research objectives are to:

- Investigate the rutting behavior for individual pavement structural layers.

- Improve the prediction performance of the current mechanistic-empirical pavement design method.

2.2 Testing Plan

To address the issues discussed in Chapter 1 and accomplish the research objectives, an APT experiment was designed in this study. Four APT sections were constructed using two typical pavement structures and two types of surface course material. One of the four sections was constructed in the same manner as the newly paved Indiana State Road (SR) 25. A mid-depth rut monitoring and automated laser profile system was designed to reconstruct the transverse profiles at each pavement layer interface throughout the process of the accelerated pavement deterioration that is produced during the APT. The contributions of each pavement structural layer to rutting and the evolutions of layer deformation thus could be derived.

Figure 2.1 presents a flow chart of the research approach. APT techniques were employed to improve current mechanistic empirical pavement design methods and assist in MEPDG local calibration. The APT sections served to supplement the field roadways used in the calibration process. All of the qualified roadway segments had been in service for less than ten years and exhibited ‘fair’ pavement conditions. The APT sections, on the other hand, exhibited distress levels close to the failure design criterion that was met by accelerated load applications. Also, the use of the APT sections reduced the required number of field roadway segments, as the APT sections led to lower standard errors of the estimates due to well-controlled test conditions and measurement procedures.

Once the database was formed, the measured rut depths were distributed into the asphalt concrete layers and subgrade. The unbound layer rutting model was calibrated externally and then the asphalt concrete layer

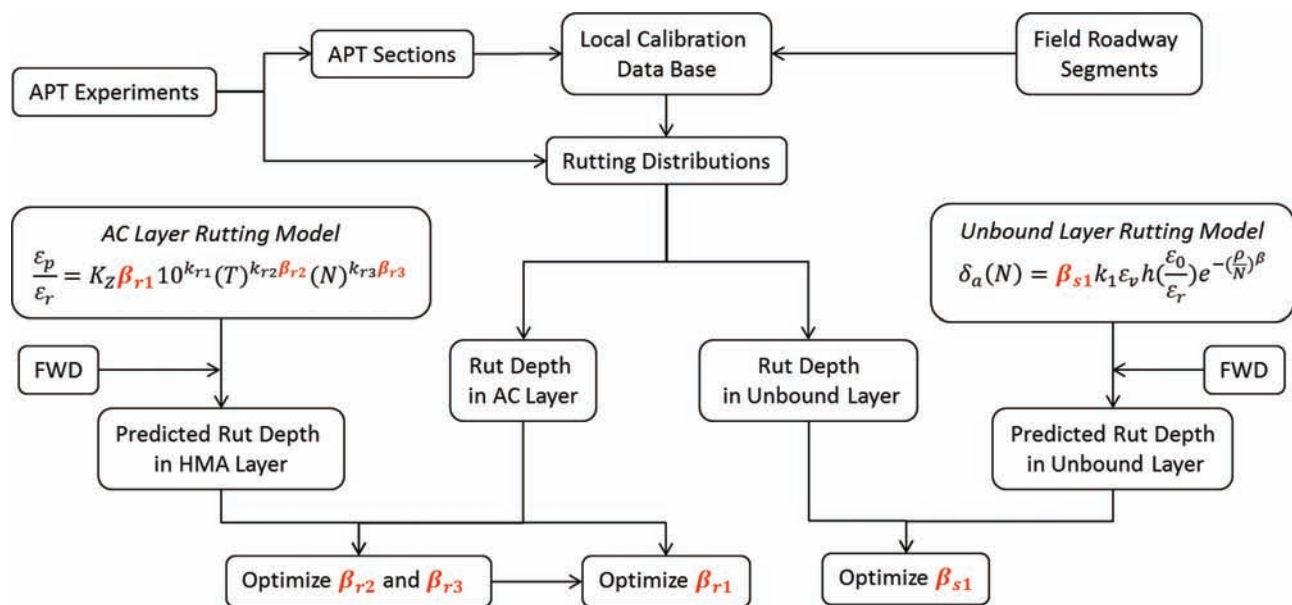


Figure 2.1 Research approach flow chart.

rutting model was calibrated using a mixed method. Then, a procedure was developed to provide the most faithful simulations of the APT conditions that include climate, traffic, and aging conditions using virtual weather station generation, a special traffic configuration, and FWD evaluation.

3. FULL-SCALE ACCELERATED PAVEMENT TESTING

3.1 Introduction

A prototype full-scale APT facility has been designed and built by Purdue University and the INDOT (Levenberg, McDaniel, & Olek, 2009). Figure 3.1 presents a photograph of the test facility. The test pit is 20 feet (6.10 m) wide by 20 feet (6.10 m) long and 6 feet (1.83 m) deep. The test facility is equipped with a radiant heating system that has the ability to maintain the air temperature at a constant 100°F (37.78°C). Higher local temperatures can be achieved by placing individual heat lamps in specific locations.

The accelerated traffic loads are applied by wheels with full-scale tires mounted to a large steel frame carriage that spans the test pit. The steel carriage is supported on two sides; each side is attached to steel rails embedded inside concrete ground. The carriage can be moved north and south along the length of the test pit, with the tire assembly able to move east and west along the carriage so that the load can be applied at any desired location.

Loading is applied through the tires by four pneumatic cylinders with air pressure control systems that adjust and maintain the applied load magnitude. The loading system is capable of applying a constant force up to 20,000 lb (9.07 ton). Two tire assembly types are available, i.e., dual tire or super single tire. A conventional dual tire set-up with tire pressure of 100 psi (0.69 MPa) was used in this research.



Figure 3.1 APT loading machine and empty test pit (Levenberg et al., 2009).

The loading machine is able to produce either unidirectional or bidirectional tire movement. For unidirectional movement, the tire assembly is raised at the end of one loading cycle, moved back to the start point, placed back onto the pavement, loaded to the desired load level, and then the loading cycle is repeated. For bidirectional movement, the tire assembly is loaded consistently at the desired load level and travels back and forth over the test sections. Wheel wander of up to 5 inches (12.7 cm) can be achieved by allowing the control computer to assign a random wander distance to each wheel pass.

An automated laser profiler is mounted beside the wheel assembly such that the wheel assembly controls the profiler's longitudinal position. An accurate servomotor controls the transverse position of the profiler. By programming the servomotor, the laser profiler is able to scan the transverse and longitudinal profiles of the pavement surface automatically at any desired location and at any time.

The APT control room is equipped with two computers and a control panel operating APT. One computer is used for APT control and programming and the other is used for data acquisition.

3.2 Test Lanes Design

In order to maximize the benefits of this APT project, it was desirable to have as many test lanes as possible while ensuring that each test lane was wide enough that wheel loads would not affect adjacent lanes. Therefore, the research team decided to divide the test pit into four independent test sections. Each test section is 5 feet (1.52 m) wide and 20 feet (6.10 m) long; see Figure 3.2.

3.2.1 Pavement Structure

The test sections were designed using the conventional INDOT full-depth flexible pavement structure with

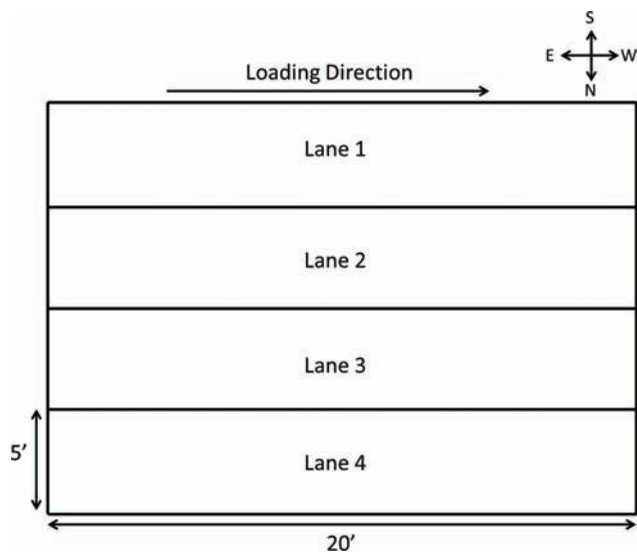


Figure 3.2 Accelerated pavement test section layout.

overall pavement thicknesses of 12.5 inches (31.75 cm) or 15.5 (39.37 cm) inches. The pavement structure has five asphalt concrete layers. As shown in Figure 3.3, all the test lanes have a 1.5-inch (3.81 cm) surface course, 2.5-inch (6.35 cm) intermediate layer, 2.5-inch (6.35 cm) open-graded (OG) drainage layer, and 3-inch (7.62 cm) lower base layer. Lane 1 and Lane 2 have a 6-inch (15.24 cm) upper base layer and the overall pavement thickness is 15.5 inches (39.37 cm). Lane 3 and Lane 4 have a 3-inch (7.62 cm) upper base layer and the overall pavement thickness is 12.5 inches (31.75 cm). Such a five-layer pavement structure is a unique design, and it has been applied to almost all full-depth flexible pavement installations in Indiana. The structure of Lane 3 and Lane 4 was intended to duplicate that of new SR-25, which connects Lafayette to Fort Wayne and was opened to traffic in October 2013. The structure of Lane 1 and Lane 2 is another common design used in Indiana.

The asphalt concrete layers were constructed on top of a layer of lime-treated A-6 soil subgrade. Compacted No. 53 aggregate left over from a previous project was underneath the subgrade. Due to the fixed depth of the pit, this layer was 12.5 inches (31.75 cm) thick in Lanes 1 and 2 and 15.5 inches (39.37 cm) thick in Lanes 3 and 4, as shown in Figure 3.3.

SMA has been widely used to improve the rutting resistance of flexible pavement. In the APT project, SMA also was included as a surface course material. As shown in Figure 3.3, the surface mixture used in Lane 1 and Lane 4 is regular 9.5-mm Superpave designed

dense-graded asphalt mixture, and that used in Lane 2 and Lane 3 is 9.5-mm SMA.

3.2.2 Paving Materials

The asphalt mix design of the APT HMA was planned so that test Lane 4 duplicated SR-25 in terms of pavement structure and paving material. Table 3.1 provides a summary of information regarding aggregate size and binder grade.

3.2.2.1 HMA Aggregate. Figures 3.4, 3.5, 3.6, and 3.7 present the aggregate gradations of the job mix formulas that are given in 0.45 power gradation charts along with control points. Each aggregate gradation meets the Superpave gradation specifications. The intermediate course and base course (i.e., including the upper base and lower base) share the same aggregate source as well as gradation.

3.2.2.2 HMA Mix Design. Table 3.2 presents the mix design parameters. The intermediate course and base course were produced using the same job mix formula, varying only in asphalt binder performance grade (PG).

3.3 Test Lanes Construction and Instrumentation

The construction of the test sections took place between November 21, 2013 and December 9, 2013. Table 3.3 presents the detailed construction sequence.

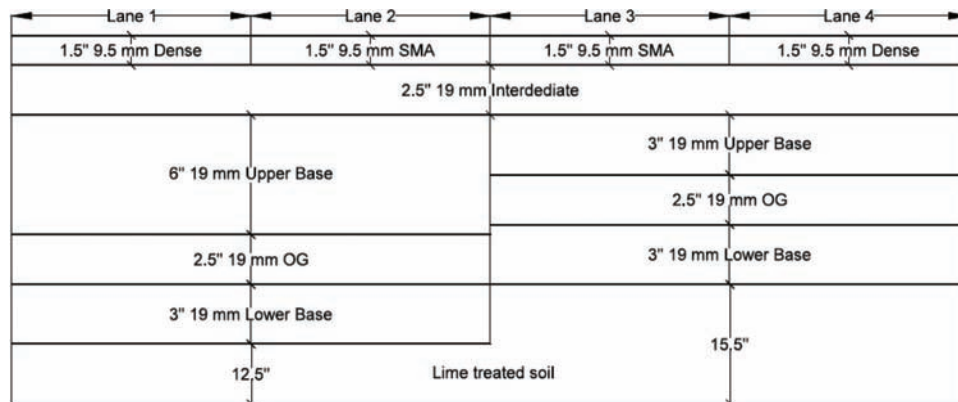


Figure 3.3 Test section structures.

TABLE 3.1
Mixtures Design Summary

Layer	Nominal Maximum Aggregate Size (NMAS)	Binder Performance Grade (PG)
Surface	9.5-mm	70-22
Intermediate	19.0-mm	70-22
Upper Base	19.0-mm	64-22
OG Layer	19.0-mm	76-22
Lower Base	19.0-mm	64-22

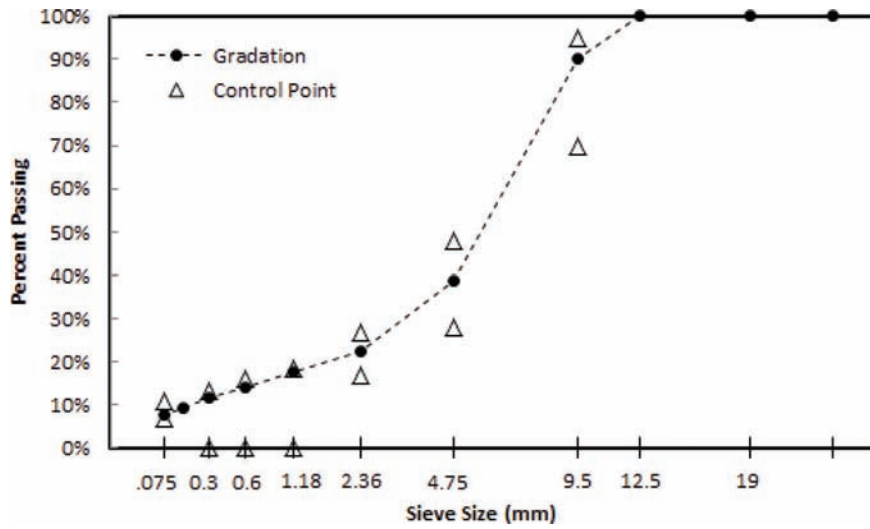


Figure 3.4 Aggregate gradation for surface SMA mix.

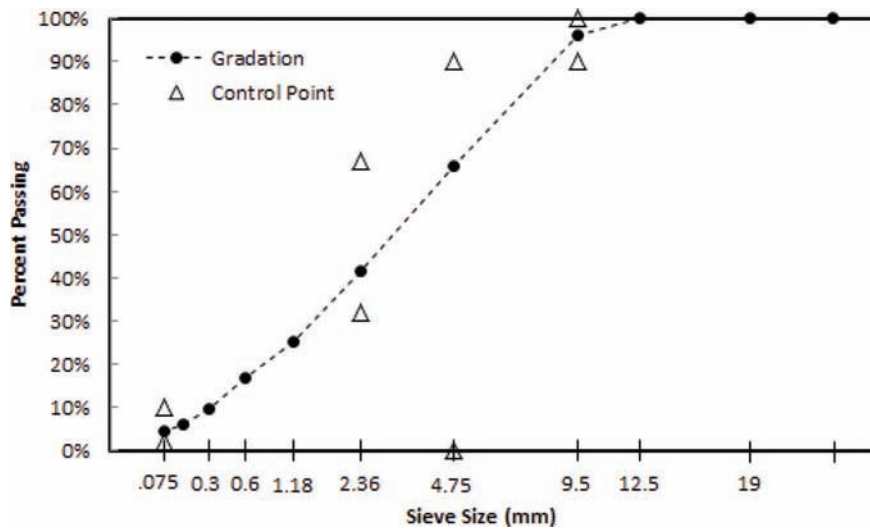


Figure 3.5 Aggregate gradation for surface dense mix.

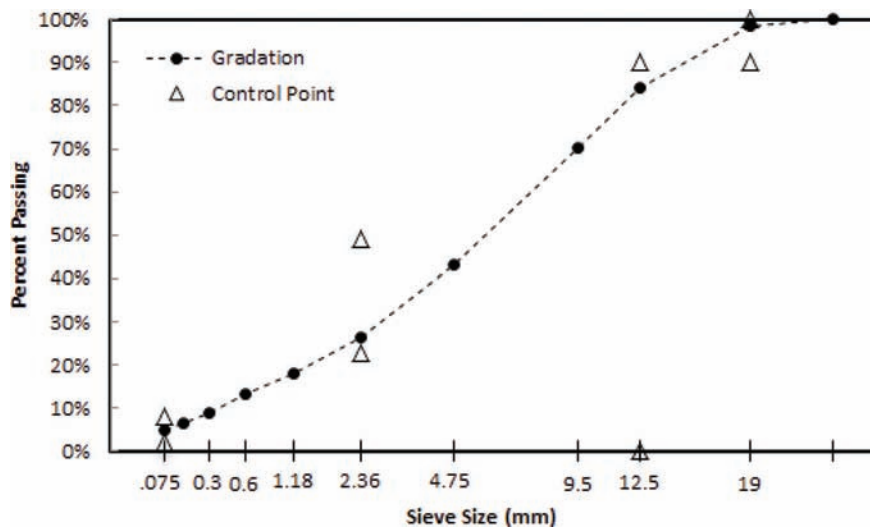


Figure 3.6 Aggregate gradation for intermediate/base mix.

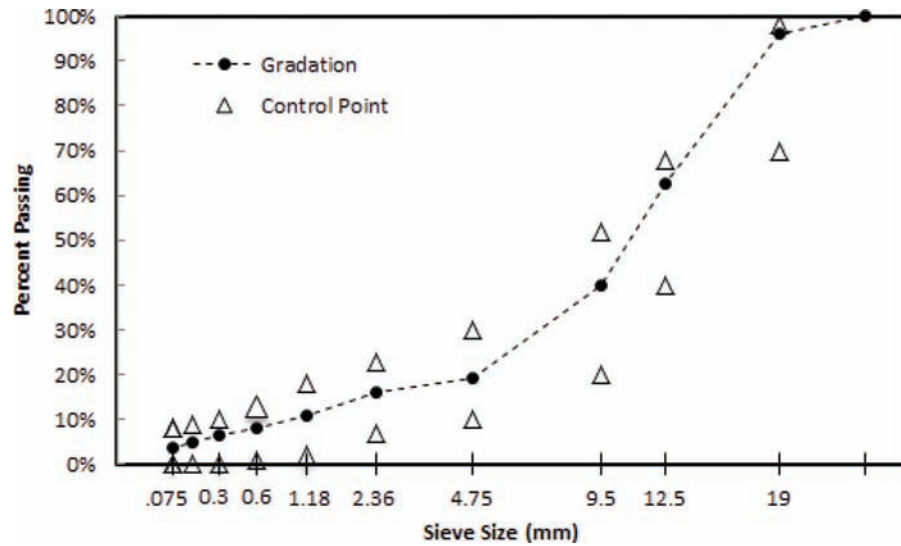


Figure 3.7 Aggregate gradation for open-graded mix.

TABLE 3.2
Mix Design Parameters

Mix Course	Surface SMA	Surface Dense	Intermediate	Base	OG
PG	70-22	70-22	70-22	64-22	76-22
NMAS (mm)	9.5	9.5	19	19	19
ESAL Categories	3/4	3	3/4	3/4	5
Binder Content by Weight (%)	5.6	5.7	4.6	4.6	3.1
Gyrations $N_{ini}/N_{des}/N_{max}$	8/100/160	8/100/160	8/100/160	8/100/160	20
G_{mm}	2.826	2.533	2.578	2.578	2.648
G_{sb}	3.101	2.716	2.719	2.719	2.723
Air Voids @ N_{des} (%)	4.0	4.0	4.0	4.0	18.8
G_{mb} @ N_{des}	2.711	2.432	2.475	2.475	2.151
VMA @ N_{des} (%)	17.5	15.6	13.2	13.2	N/A
VFA @ N_{des} (%)	76.6	74.4	69.7	69.7	N/A
Compaction Temp.	300°F	300°F	300°F	300°F	260°F

Note that in Table 3.2, NMAS refers to nominal maximum aggregate size; ESAL refers to equivalent single axle load; VMA refers to voids in mineral aggregate; VFA refers to voids filled with asphalt; G_{mm} refers to theoretical maximum specific density; G_{sb} refers to bulk specific gravity of aggregate; G_{mb} refers to bulk specific gravity of the mix. N_{ini} is the number of gyrations used as a measure of mixture compactability during construction; N_{des} is the design number of gyrations required to produce a sample with the same density as that expected in the field after the indicated amount of traffic; and N_{max} the number of gyrations required to produce a laboratory density that should never be exceeded in the field.

TABLE 3.3
Construction Sequence

Date	Task
11/21/2013	Subgrade Construction
12/2/2013	Instrumentation
12/3/2013	Lower Base Layer Construction
12/4/2013	Instrumentation
12/5/2013	OG Layer Construction
12/5/2013	Instrumentation
12/6/2013	Upper Base Layer Construction
12/7/2013	Intermediate Construction
12/9/2013	Surface Layer Construction

3.3.1 Test Lanes Construction

3.3.1.1 Construction of Subgrade Soil. Lime-stabilized A-6 soil (also known as silt-clay soil according to the

AASHTO soil classification system) is a common sub-grade material used in Indiana and was used in the construction of SR-25. This soil was prepared for this study at the INDOT Lafayette Maintenance Unit. As shown in Figure 3.8, first the original A-6 soil pile was spread, and then 5 percent lime was applied and mixed using a soil stabilizer. Once the soil was thoroughly blended with the lime, it was transported to the APT facility and placed inside the test pit within two hours. The subgrade construction was conducted by lifts, and water was added between lifts in order to activate the lime and allow it to develop to its maximum strength. Full-sized compaction equipment could not be used due to the elevation drop along the edges of the test pit, as shown in Figure 3.8 (f). Thus, compaction was performed using a hand-operated sheep foot roller compactor and a jumping jack tamper. The lime-treated subgrade



Figure 3.8 Subgrade construction.

was cured for 11 days after construction to allow strength to develop.

The strength of the subgrade was evaluated using a dynamic cone penetrator (DCP) and a light-weight deflectometer (LWD) as shown in Figure 3.9.

A DCP is a simple and convenient device that is used to measure the penetration resistance of *in situ* material. As shown in Figure 3.9 (a), in order to perform a DCP test, a shaft with a cone-shaped tip is placed at the ground surface and a solid 17.6-lb (7.98 kg) weight is dropped from a standard height of 26 inches (66.04 cm). During the test, the number of blows is recorded for a specified cone penetration. DCP testing was performed on the subgrade in accordance with ASTM D 6951 (2015), Standard Test Method for Use of the Dynamic Cone Penetrometer in Shallow Pavement Applications.

The LWD test was used to measure the *in situ* modulus values of the materials, as shown in Figure 3.9 (b). A bearing plate 11.81 inches (30.00 cm) in diameter was placed on the surface to be tested, and a standard weight (22 lb or 10 kg) was released from a specified height (28.34 in. or 71.98 cm) so that it impinged upon

the bearing plate. The resulting deflection of the bearing plate was obtained by double integrating the accelerations measured by an accelerometer inside the bearing plate. For the purposes of this project, the LWD tests were performed at the surface of the subgrade as well as at each layer interface in accordance with ASTM E 2583 (2015), *Standard Test Method for Measuring Deflections with a Light Weight Deflectometer (LWD)*. The elastic modulus values of the tested material were calculated based on Boussinesq half-space elastic solution, as shown in Equation 3.1. Figure 3.10 shows the test locations. Table 3.4 and Table 3.5 provide the subgrade strength evaluation results for the DCP and LWD tests, respectively, with 20 as the average number of DCP test blows for 6-inch (15.24 cm) penetration and an average LWD deflection of 0.37 mm (0.0146 inch). The moisture content at the end of the curing period was 15.0 percent.

$$E = \frac{(1 - \nu^2)\sigma_0 a}{d_0} \times f \quad (3.1)$$

where:

E = modulus (MPa);

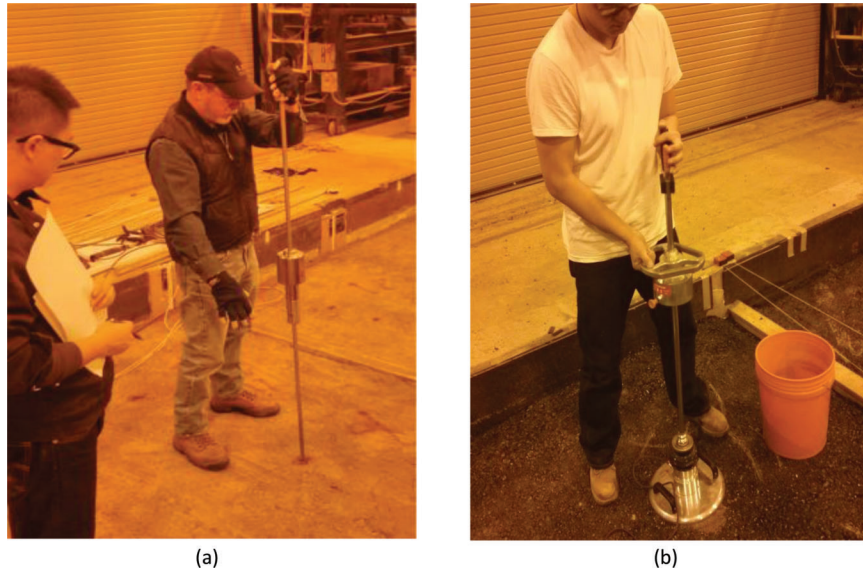


Figure 3.9 (a) Dynamic cone penetrometer and (b) light-weight deflectometer testing.

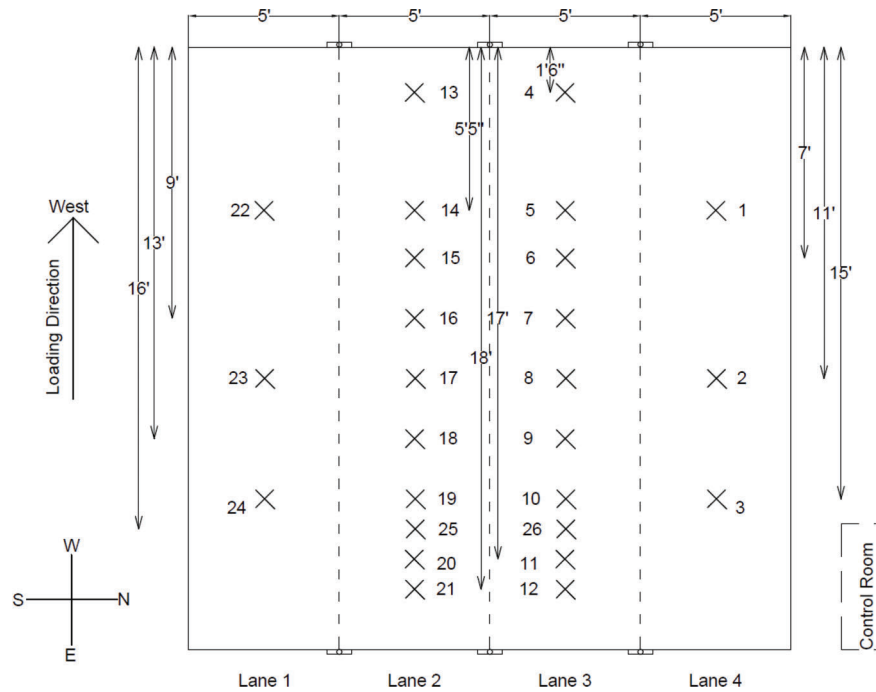


Figure 3.10 Locations of dynamic cone penetrometer and light-weight deflectometer tests on subgrade soil.

TABLE 3.4
Dynamic Cone Penetration Test Results

Location	Number of Blows for 6-inch Penetration
5	14
8	24
10	19
14	18
17	23
19	22

d_0 = measured displacement (mm);
 ν = Poisson's ratio;
 σ_0 = applied stress (MPa);
 a = radius of the plate (mm); and
 f = shape factor depending on stress distribution.

3.3.1.2 Construction of HMA Layers. The lower base layer, OG drainage layer, and upper base layer were paved manually because a full-size paver could not fit inside the test pit. One or two days between the construction of each asphalt concrete layer allowed for the

TABLE 3.5
Light-Weight Deflectometer Test Results

Location	Deflection (mm)	Location	Deflection (mm)	Location	Deflection (mm)
1	0.449	9	0.281	17	0.331
2	0.631	10	0.348	18	0.452
3	0.490	11	0.297	19	0.505
4	0.321	12	0.281	20	0.356
5	0.351	13	0.336	21	0.427
6	0.338	14	0.468	22	0.567
7	0.301	15	0.332	23	0.39
8	0.429	16	0.382	24	0.433

installation of the instrumentation (covered in section 3.3.2.2). The entire asphalt concrete layer construction process took eight days.

The HMA material was transferred directly to the pit by shuttle buggy to prevent mixture segregation, as shown in Figure 3.11 (a). The layers were compacted using a two-ton roller compacter, shown in Figure (b), and a vibratory plate, shown in Figure 3.11 (c). A tack coat was applied between each of the asphalt concrete layers to ensure full bonding, as shown in Figure 3.11 (d). The intermediate layer and surface layer were paved using a full-size paver along with a 10-ton roller compacter, shown in Figure 3.11 (e) and (f). The degree of compaction was evaluated using a pavement quality indicator (PQI), as shown in Figure 3.11 (g). The PQI measures the density of asphalt pavement via a measured dielectric constant of the material. The degree of compaction is given by the percentage of the theoretical maximum specific density ($\% G_{mm}$) using the measured bulk specific gravity (G_{mb}) value. During the APT section construction, the $\% G_{mm}$ was measured during compaction, and a target of 93 percent G_{mm} was ensured for every asphalt concrete layer except the OG drainage layer. The PQI readings for the OG drainage layer could be erroneous due to the high air void content; therefore, eight roller compacter passes were made for each lift in accordance with OG drainage layer construction experience. The as-constructed layer thicknesses were determined by measuring the relative distance between the as-constructed surface and the pit surface at random selected points, as shown in Figure 3.11 (h). The as-constructed layer thickness was maintained within 1/8 inch (0.32 cm) of the designed value.

3.3.2 Instrumentation and Pavement Response Monitoring

Instrumentation includes the installation of sensors that measure the pavement's mechanical responses, such as vertical stress, horizontal strain, pavement temperature, and moisture content. Pavement response monitoring includes an FWD test and pavement surface profile measurements. The FWD test is used to evaluate the pavement's *in situ* modulus, and the surface profile measurements are used to determine pavement surface rutting as well as individual layer rutting.

3.3.2.1 Sensor Selection. Asphalt strain gauges were installed at the top of the subgrade, which was assumed to be the critical tensile strain location due to traffic loading, and to the top and bottom of the OG drainage layer to evaluate the drainage layer's behavior. The strain gauges were located along the centerlines of Lane 2 and Lane 3. Both longitudinal and transverse directional strains were measured. Eighteen strain gauges were installed. Twelve of these gauges were manufactured by Construction Technology Laboratory (CTL) and are shown in Figure 3.12 (a), and six gauges were provided by Dynatest and are shown in Figure 3.12 (b). Both types are about 8 inches (20.32 cm) long, 6 inches (15.24 cm) wide, and 3/4 inch (1.91 cm) thick. The approximate stiffness values obtained from the CTL and Dynatest gauges are 340,000 psi (2,344 MPa) and 319,083 psi (2,200 MPa), respectively.

Gauge functionality was checked prior to the gauge installation. Specifically, all gauges were connected to a data acquisition system and checked to determine that (1) there was signal stability in the neutral condition; (2) the initial response in the neutral condition was within a reasonable range; and (3) the output signal was reasonable based on external tension or compression stimulus. Calibration of the strain gauges was performed individually by the manufacturer, and then the gauges were shipped to the APT facility.

Ten Geokon model 3500 earth pressure cells, shown in Figure 3.13, were installed along with the asphalt strain gauges. These pressure cells measured the vertical pressure within the pavement structure. Each pressure cell consists of two round steel plates with a diameter of 9 inches (22.86 cm). The gap between the two plates is filled with de-aired oil, and hence, the earth pressure is measured through the fluid pressure.

HMA is a type of material whose properties depend highly on the temperature and loading frequency. Therefore, thermocouples, as shown in Figure 3.14 (b) were installed at each layer interface in all the test lanes to monitor the temperature profile across the pavement structures (i.e., 20 thermocouples were installed). Four moisture gauges were installed at the subgrade surface and at the boundaries between Lane 4 and Lane 3 and between Lane 2 and Lane 1. Two additional moisture gauges were installed at the surface of the OG layer and at the boundaries between Lane 4 and Lane 3 and between Lane 2 and Lane 1. In the second phase of this



(a) transferring material into pit



(b) 2-ton roller compacter



(c) vibratory plate



(d) applying tack coat



(e) full size paver



(f) 10-ton roller compacter



(g) pavement quality indicator evaluation



(h) checking paving thickness

Figure 3.11 Asphalt concrete layer construction.

project, water will be introduced into the subgrade through preinstalled water pipes, and the moisture gauges will be used to monitor the water content in the subgrade and OG drainage layer as part of an additional testing project. The moisture gauges are 5m Soil Moisture & Temperature Sensors manufactured by Decagon Devices, Inc., shown in Figure 3.14 (a). These moisture gauges measure the volumetric water content with an accuracy of 0.08 percent. The operational temperature is from -40°C to 60°C (-40°F to 140°F). The gauge dimensions are 10 cm × 3.2 cm × 0.7 cm (3.94 in. × 1.26 in. × 0.28 in.).

3.3.2.2 Sensor Installation. Several considerations were taken into account when designing the instrumentation layout. Because the location of critical tensile strain is one of the main interests in this study, the subgrade, lower base, and OG layer surfaces were instrumented. Because the test sections would be loaded unidirectionally without applying wander, the strain gauges and load cells were installed at the centerlines of each test lane, along the longitudinal line of the load application. According to previous research (Al-Qadi, Loulizi, Elseifi, & Lahouar, 2004; Choubane, Greene, & Sheppard, 2011; Jones, Harvey, Mateos, & Al-Qadi, 2012;

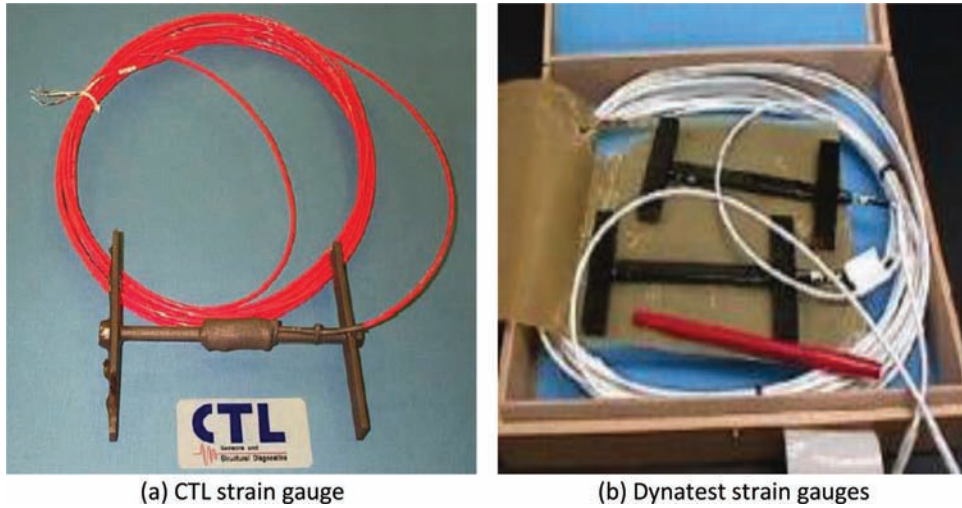


Figure 3.12 Asphalt strain gauges.

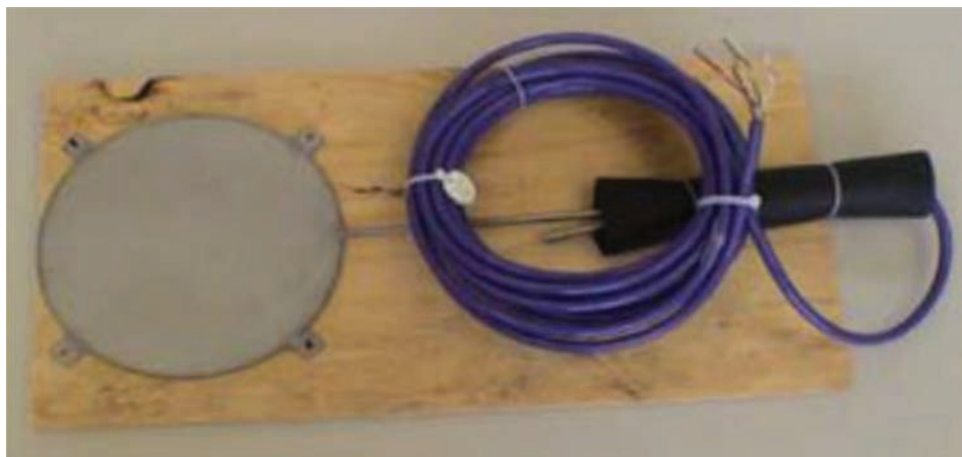


Figure 3.13 Geokon model 3500 earth pressure cell.

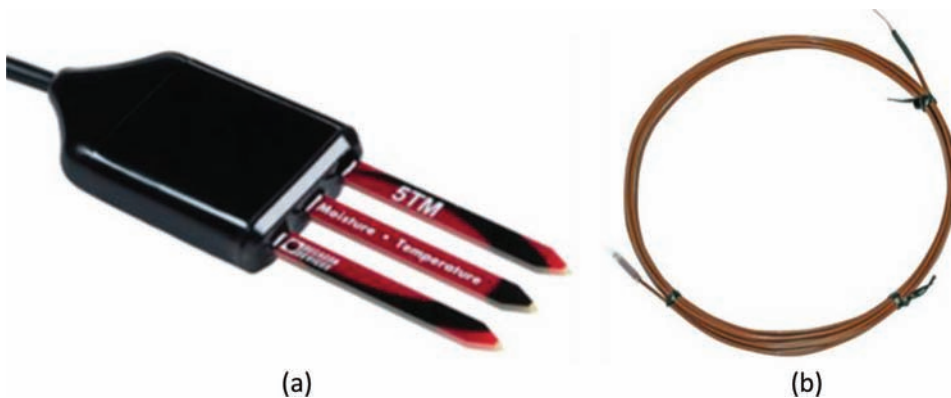


Figure 3.14 (a) 5TM Soil Moisture & Temperature Sensor and (b) thermocouple.

McEwen, Priest, & Timm, 2004; Zafar, Nassar, & Elbella, 2005), instrumented sensors should be spaced apart to avoid sensor interaction. Based on suggestions from other researchers, a minimum of two feet of horizontal spacing and 5.5 inches (13.97 cm) of

vertical spacing were selected. The instrumentation layout can be found in Appendix A.

Most of the strain gauges and load cells had one duplicate, the exception being at the surface of the lower base layer due to limited space and the number

of available gauges. Efforts were made to avoid placing gauges within the tire assembly's acceleration and deceleration areas. However, due to limited space, duplicate load cells at the surfaces of the subgrade and OG layers were placed in the acceleration area. The gauges in the deceleration area were the load cells at the surface of the lower base layer. The gauges placed in the acceleration or deceleration areas would serve only as back-ups in case of gauge failure during construction. At the surface of the subgrade, two gauges were placed at a 45-degree angle between the test lane centerline and gauge centerline. These gauges were used in a trial to investigate the possibility of correlating 45-degree strain with longitudinal and transverse strains.

When installing the load cells in the subgrade, cell-shaped holes were dug along with trenches for the cables. When placing the cells, care was taken to avoid direct contact between any large stones and the load cells. Before placing the cells inside the cavities, it was critical that the cells be properly leveled with no air voids beneath them in order for the load cells to maintain accuracy (Timm, Priest, & McEwen, 2004). This set-up was achieved by repeatedly checking the imprint beneath each load cell and checking whether or not the cell was leveled properly. Once the load cell placement was completed, fine material was used to backfill the hole to protect it from the asphalt layer construction. When installing the load cells in the asphalt layers, it was not possible to dig a hole as had been possible in the subgrade soil, so the load cells were placed directly on top of the asphalt layer surface, and sand was used to fill in between the load cells and asphalt surface. Again, the cells were placed carefully so that they were level and had no air voids underneath them. For the moisture probe installation, a hole was dug in the subgrade surface and the probe was then buried inside. To install the moisture probe in the OG layer, the probe was placed directly on top of the surface and buried under fine sand. For the strain gauge and thermocouple installation, asphalt

binder was used to bind the sensors to the layer surface. After installation, loose asphalt mixture from the subsequent layer to be placed was used to cover the sensors and then hand-compacted to protect the sensors from the construction process.

Table 3.6 presents the initial recorded responses of the strain gauges and load cells. Figures 3.15, 3.16, and 3.17 present the finished instrumentation at the subgrade surface, lower base layer surface, and OG layer surface, respectively.

3.3.2.3 Pavement Surface Profile Measurement Using Laser Profiler. An automated laser profile system was used to scan the pavement surface during loading, and the pavement total rutting and individual layer rutting measurements were obtained based on the measured profile. In this laser profiler system, a motor moves the laser gauge horizontally (north to south), and the wheel moves the system longitudinally (east to west). Once the transverse profile is requested, the wheel first moves the system to the desired longitudinal location and then the motor drives the laser gauge to scan the requested transverse profile. Once the longitudinal profile is requested, the motor first moves the laser gauge to the desired transverse location and then the wheel drives the laser gauge to scan the requested longitudinal profile. Through programming, the transverse and longitudinal profiles of a test lane can be measured at any desired location and at any time.

For this study, the system consisted of a Parker MPJ Series Motor and an Accurange AR700 laser distance gauge, shown in Figure 3.18 (a) and (b), respectively. These devices were mounted beside the wheel assembly; the laser gauge was about 10 inches (25.4 cm) above the pavement surface, which was also approximately at the center of the span of the laser gauge, which was 6 inches (15.24 cm), as shown in Figure 3.19. The resolution of the profile scan was 0.16 mm (0.00630 inch)/data point with an accuracy of 0.15 mm (0.00590 inch).

One of the main objectives of this study is to evaluate the rutting distribution within the pavement

TABLE 3.6
Initial Gauge Responses

Gauge Number	Initial Reading (mv)	Gauge Number	Initial Reading (mv)
SG1	0.4185	SG16	-0.3313
SG2	0.1643	SG18	-0.2515
SG3	-0.2355	SG19	0.1573
SG4	1.1623	SG20	-0.1078
SG5	0.0253	LC1	1.5
SG6	0.7883	LC2	-0.3
SG8	-0.8380	LC3	3.4
SG9	0.1175	LC4	1.5
SG10	-0.6080	LC5	1.2
SG11	0.1328	LC6	-1.5
SG12	-0.5253	LC7	2.7
SG13	-0.4140	LC8	1.5
SG14	-0.2750	LC9	1.8
SG15	-0.4243	LC10	1.8

Note: SG = strain gauge; LC = load cell.

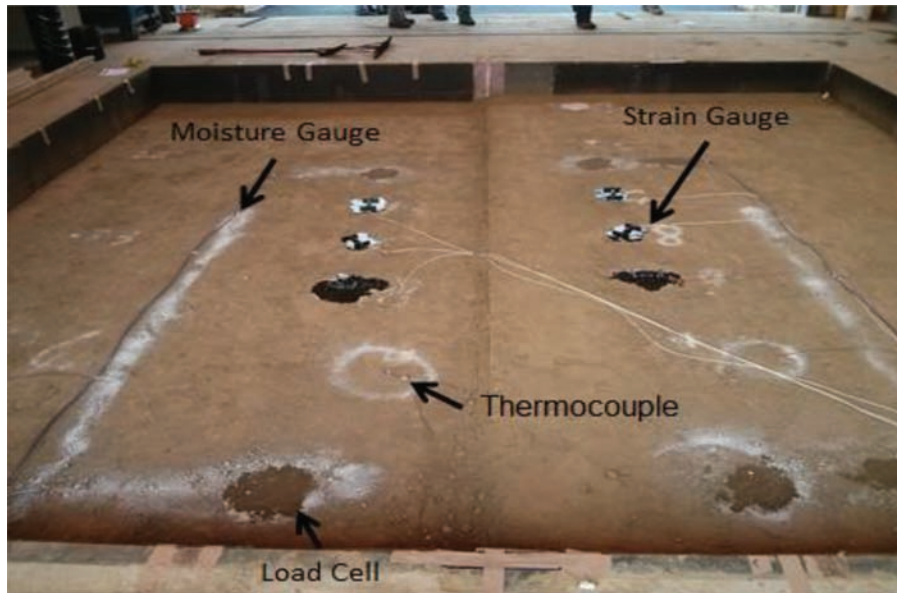


Figure 3.15 Sensors at the subgrade surface.

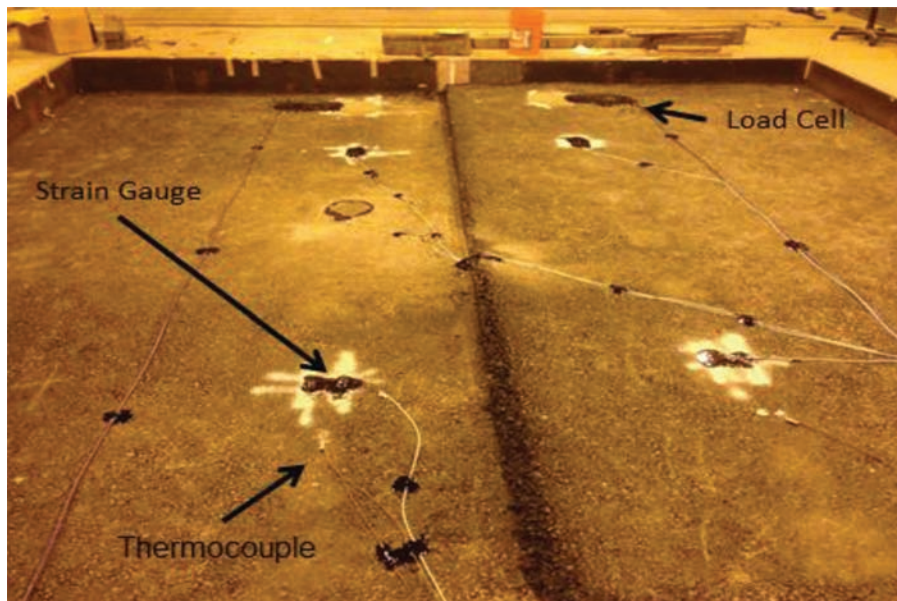


Figure 3.16 Sensors at the lower base layer surface.

structure. The test sections have more than 12.5 inches (31.75 cm) of asphalt concrete material constructed on lime-stabilized subgrade. It was expected that the amount of rutting in some layers, especially the subgrade, could be very small. If the target total rutting is 10 mm (0.4 inch), the amount of rutting in the subgrade might be as small as 1 mm (0.04 inch). In order to capture such a small amount of deformation using the laser gauge, a reference system was built, as shown in Figure 3.20. Two 2-inch by 2-inch (5.08 cm by 5.08 cm) aluminum bars were installed along the edges of each test lane and supported at the concrete pad so that they were isolated from the pavement surface. Each profile

scan started at one reference bar and ended at the other. In this way, any vertical movement of the laser gauge could be taken into account.

Due to the fact that most rutting occurs at the primary stage, the profile measurements were taken more frequently at the beginning of the load application. Table 3.7 provides the detailed profile measurement plan. Thirty-four sets of profiles were taken for each test lane during 50,000 load applications. Each set contained five transverse profiles located at the intact portion of the test lane and within the constant speed zone, as shown in Figure 3.21, and seven longitudinal profiles for the mid-depth rut measurements.

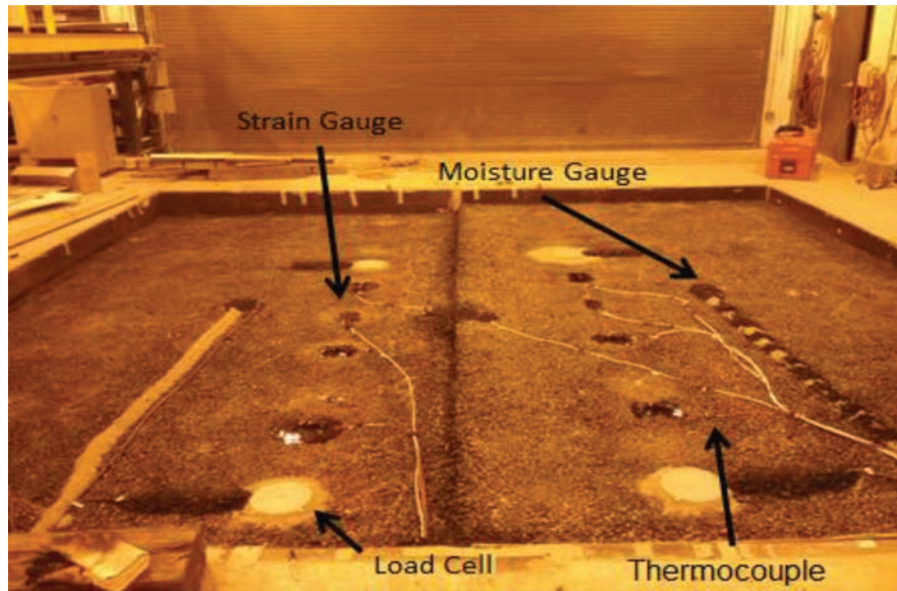
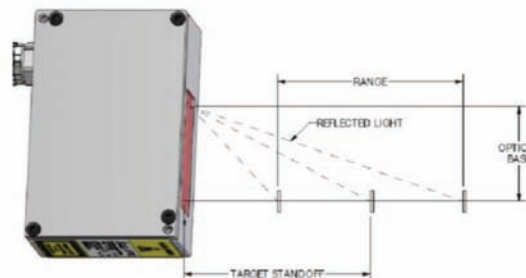


Figure 3.17 Sensors at the open-graded (OG) layer surface.



(a) Parker MPJ Series Motors



(b) Accurange AR700 laser distance gauge

Figure 3.18 Laser profile system components.



Figure 3.19 Automated laser profile system.



Figure 3.20 Reference system.

TABLE 3.7
Profile Measurement Plan

Number	Load Application	Number	Load Application	Number	Load Application
1	0	13	900	25	17,500
2	25	14	1,000	26	20,000
3	50	15	1,500	27	22,500
4	75	16	2,000	28	25,000
5	100	17	2,500	29	27,500
6	200	18	3,000	30	30,000
7	300	19	4,000	31	35,000
8	400	20	5,000	32	40,000
9	500	21	7,500	33	45,000
10	600	22	10,000	34	50,000
11	700	23	12,500		
12	800	24	15,000		

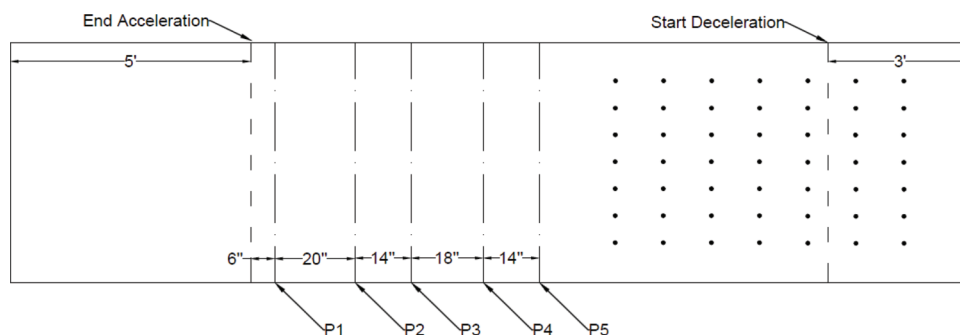


Figure 3.21 Transverse surface profile locations.



Figure 3.22 Rutted sample.

3.3.2.4 Monitoring Layer Deformation. To monitor the rutting that developed within each individual layer, a series of monitoring holes were drilled into the pavement surface. In order to reconstruct the transverse profile of the layer interface under dual tire loading, at least seven points were required, with one point between the two tires (the upheave point), one point in the middle of each tire (depression points, two total), one point on the outside of each tire (upheave points, two total) and one point further outside each tire (reference points, no upheave or depression expected, two total). Five sets of monitoring holes were drilled, one for each layer interface. By measuring the change in elevation at the bottom

of the monitoring holes, the profile of each interface could be measured at the seven points transversely across the test lanes. These profiles could be used to determine the rutting that occurs in each individual layer.

In order to capture an interface profile, it is important to choose the correct spacing for a set of monitoring holes. Ideally, each point should be positioned at either the highest point of upheave or the lowest depression point, but these locations are difficult to determine *a priori*. For this study, as a best estimate for properly locating the monitoring holes, measurements were taken from an asphalt pavement sample that had been saw-cut in a previous APT project; Figure 3.22 shows a

photograph of this rutted sample. That project used the same loading parameters as were used in this study. Based on the sample, monitoring hole spacing of 6.75 inches (17.15 cm) was deemed appropriate.

Appendix A includes the layout of the monitoring holes. Seven sets of holes were drilled in Lane 1 and Lane 4. The two extra sets of holes served as back-ups in case a hole collapsed during testing. The east side of Lane 1 remained intact to provide a valid surface profile. For the same reason, only the west side of Lane 4 was drilled. For Lane 2 and Lane 3, only one set of 1.5-inch (3.81 cm) deep monitoring holes and one set of 12.5-inch (31.75 cm) or 15.5-inch (39.37 cm) holes were drilled. The structure and materials were almost identical at this location; only the surface course material was different. That is, Lane 1 and Lane 4 were constructed with a regular dense-graded mixture, and Lane 2 and Lane 3 contained SMA mixtures. So, it was assumed that the rutting for each layer in these locations would be the same, with the possible exception of the surface courses.

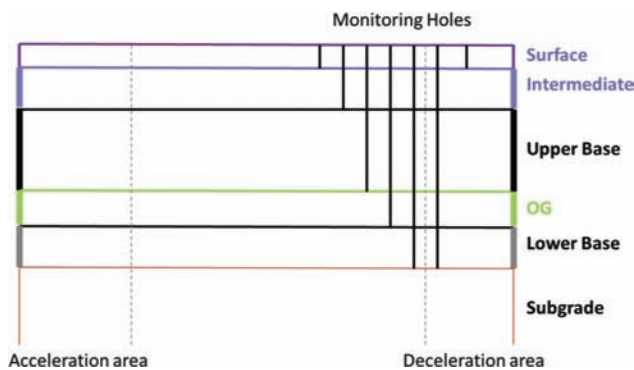


Figure 3.23 Longitudinal cross-section view of monitoring holes in pavement structure.

Also, these two test sections were heavily instrumented, and the drilling process could damage the sensors or leads. Figure 3.23 provides a longitudinal cross-section view of the monitoring holes in the pavement structure.

Laser pointers were used to ensure that the monitoring holes were aligned perfectly with the laser profiler and were drilled perpendicular to the surface, as shown in Figure 3.24. The monitoring holes were 1.5 inches (3.81 cm) in diameter. Steel conduit was inserted inside the monitoring holes to protect them from collapsing during loading. During loading, it was anticipated that the holes could become slightly skewed from their perpendicular orientation due to shear failure of the asphalt layers. Because the holes were only 1.5 inches (3.81 cm) in diameter, any such skew might prohibit the laser profiler from correctly reading the bottom of the monitoring holes. To alleviate this possibility, steel rods were inserted in the monitoring holes such that the tops of the rods were one inch below the layer surface. Thus, the laser profiler could measure the elevation at the top of the steel rods instead of at the bottom of the monitoring holes, as shown in Figure 3.25.

3.3.2.5 Test Section Design Verification. To examine the influential zone of the wheel load as well as the effect of the monitoring holes, a simple two-dimensional finite element (2-D FE) model was built, and the configuration of four test lanes was examined using a commercial finite element program, ABAQUS v. 6.10. The model test lane was 5 feet (1.524 m) wide and 28 inches (71.12 cm) deep, with fixed bottom and side boundaries. An elastic model was chosen that included typical values for Young's modulus and Poisson's ratio for the HMA materials, as shown in Table 3.8.

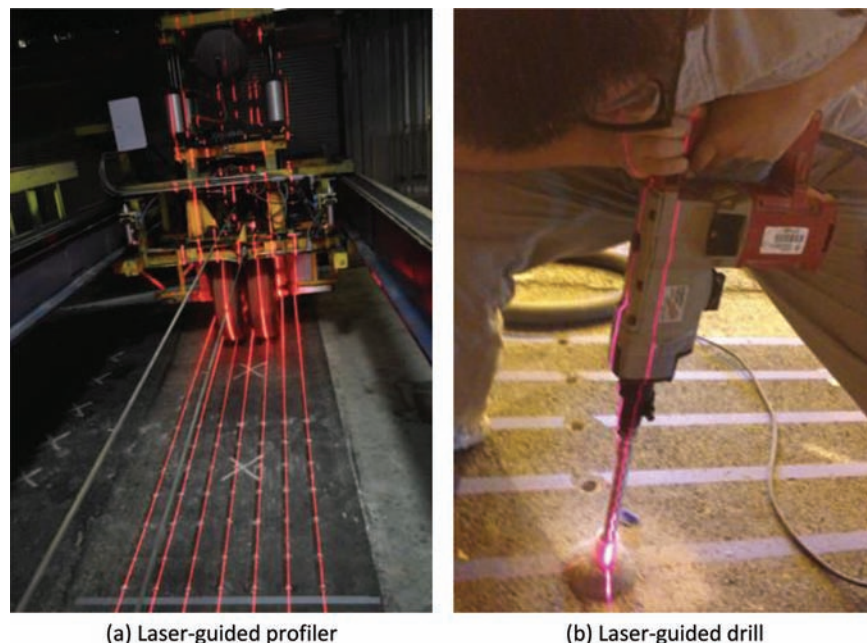


Figure 3.24 Construction of monitoring holes.

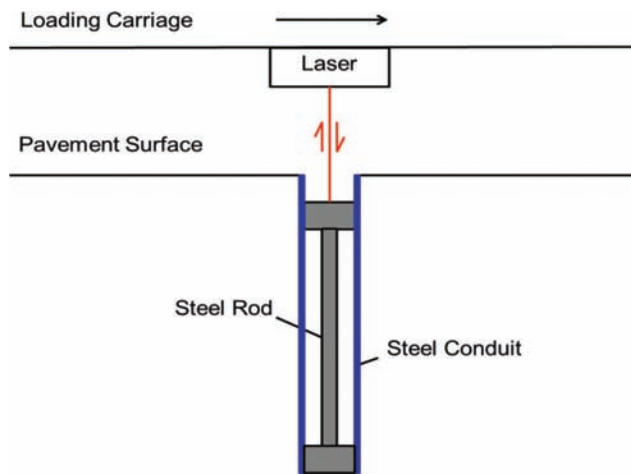


Figure 3.25 Laser measurements of monitoring holes.

TABLE 3.8
Material Properties for Finite Element Model

Layer	Elastic Modulus (psi)	Poisson's Ratio
Surface	500,000	0.3
Intermediate	300,000	0.3
Upper Base	350,000	0.3
OG	150,000	0.3
Lower Base	350,000	0.3
Subgrade	150,000	0.3

To simulate traffic loading on a pavement, one approach is to assume that the vertical stress induced by traffic at the pavement surface is distributed uniformly over an oval area (to simulate a tire imprint) with the magnitude of the stress equal to that of the tire inflation pressure (Onyango, 2009). In reality, however, tire pressure and contact areas are dependent upon the amount of load that can be withstood by the tires, and the stress distribution over the contact area might not necessarily be uniform. Several research studies have shown that the uniformity of the stress distribution over the contact area affects the pavement response (Al-Qadi et al., 2004; De Beer, Groenendijk, & Fischer, 1996; Hua, 2000; Stiadly, Hand, Noureldin, Hua, & White, 2003).

In order to simulate the pavement's response to vehicular loading accurately, the contact area, stress distribution, and tire pressure should be taken into account. De Beer et al. (1996) studied tire pressure using a Vehicle-Road Surface Pressure Transducer Array (VRSPTA) system and determined the stress underneath each tire tread. In this research, De Beer et al. studied the tire pressure distribution and tire imprint along with wheel load calibration. In a preliminary model, they assumed that (1) the stress distribution was uniform, (2) the diameter of the loaded area was equal to an actual tire width (8 inches or 20.32 cm), and (3) the distance of the space between two tires was 5.5 inches (13.97 cm).

Drilling monitoring holes into test lanes may affect the performance of the pavement test sections. To investigate the effects of the monitoring holes on the

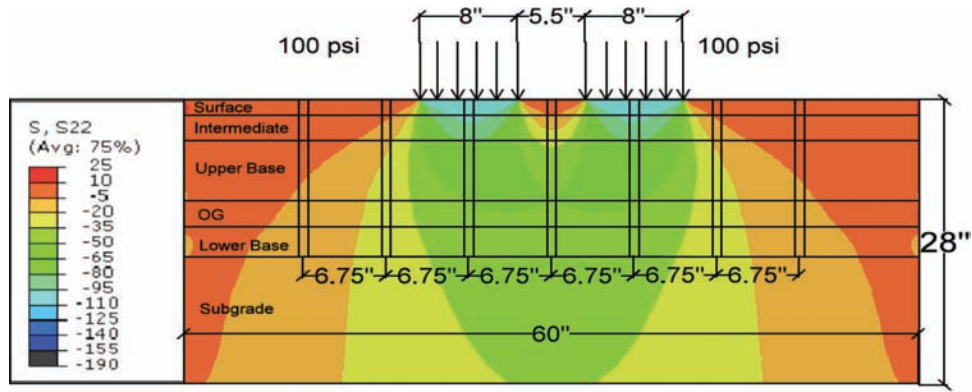
integrity of the pavement structure in this study, the 2-D FE model was used with the monitoring holes added to the system. A series of elements (2-D 4-node plain strain elements with dimensions of 0.5 inch by 0.5 inch or 1.27 cm by 1.27 cm) were selected to represent the monitoring holes. For the case of no monitoring holes, the modulus values of the elements were assigned the same value as the corresponding pavement layer. For the case with monitoring holes, the assigned modulus values were extremely low to simulate the drilled holes.

As shown in Figure 3.26 (a), the influential zone of the wheel load is limited to within a single test lane. This being the case, a four-lane configuration is reasonable. Figure 3.26 (b) presents the vertical stress contour plots. As shown, the existence of the monitoring holes changed the stress distribution within the pavement structure. The stress concentration was observed along the two monitoring holes immediately beneath the wheels, which resulted in weak zones around the monitoring holes. This scenario likely would lead to an increase in deformation immediately adjacent to the openings of the monitoring holes. However, Figure 3.26 (a) and (b) indicate that the stress distribution in the pavement structure immediately beneath the monitoring holes remained relatively similar. Because the depth measurements of the holes were taken with reference to the bottom of the holes, it is reasonable to assume that the measurements were valid and could correctly represent the resulting permanent deformation of the pavement structure beneath the monitoring holes.

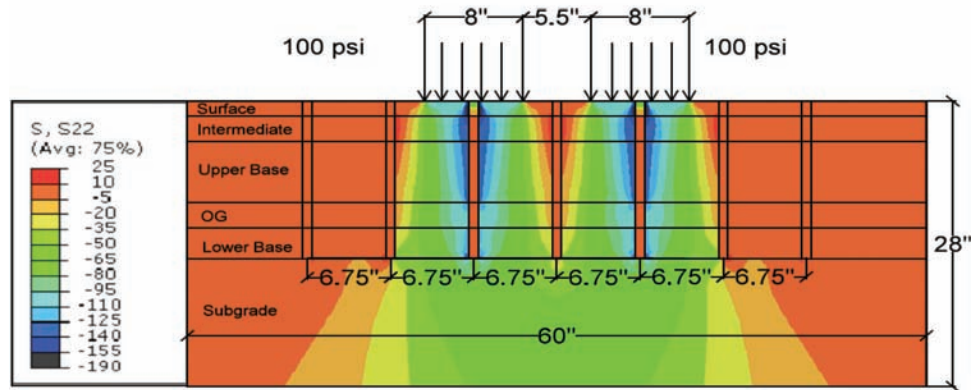
3.3.2.6 Data Acquisition. The computer used for data acquisition is networked to two Vishay Micro-Measurement System 6000 scanners, as shown in Figure 3.27. Each scanner has 20 input channels, with the highest sampling rate of 10 kHz. By installing four thermocouple cards (model 6020), 20 strain gauge cards (model 6010), and five high level cards (model 6030), four thermocouples, eighteen strain gauges, and five load cells can be monitored at the same time.

3.3.2.7 Pavement Structure Evaluation Using Falling Weight Deflectometer. The FWD is widely used to evaluate pavement structures and determine *in situ* modulus values, as shown in Figure 3.28. The FWD applies an impact force to a circular plate placed on the surface of the pavement and measures the resulting deflections at the center of the load as well as at fixed radii from the loading center. Deflections at the load center represent the overall structural capacity of the pavement. A set of pavement deflections can be used to back-calculate pavement layer modulus values using various programs, such as ELMOD, MODULUS, and MODCOMP (Alavi, Tavares, & LeCates, 2008; Noureldin & Zhu, 2007).

An FWD test was performed to evaluate the pavement modulus evolution that is caused by APT trafficking at different transverse locations (i.e., in the wheel path and outside the wheel path) and to determine the



(a) Finite element model without monitoring holes



(b) Finite element model with seven monitoring holes

Figure 3.26 Contour plots for vertical stress.



Figure 3.27 Vishay Micro-Measurements System 6000.

hardening effect that is caused by asphalt aging. The test was conducted in accordance with ASTM D 4694-09 (2015), *Standard Test Method for Deflections with a Falling-Weight-Type Impulse Load Device*, before and after APT trafficking at each test lane. Test locations were chosen at the sites where strain gauges or load cells were embedded in Lane 2 and Lane 3, with six additional test locations in Lane 1 and Lane 4. Seven points were tested at each location. The layout of those seven points is the same as that of the mid-depth rutting monitoring holes, as shown in Figure 3.29.

For most of the test locations, geophones were oriented toward the west; exceptions were locations 13 and 4 where, due to limited space in the test lanes on the west side of these two locations, the geophones were oriented

toward the east. The nine geophones were placed at -12, 0, 8, 12, 18, 24, 36, 48, and 60 inches (-30.48, 0, 20.32, 30.48, 45.72, 60.96, 91.44, 121.92, and 152.4 cm) from the center of the FWD loading plate. One set of FWD load drops consisted of three load levels (i.e., 7,000 lb, 9,000 lb, and 11,000 lb or 3,175 kg, 4,082 kg, and 4,989 kg), and three sets of FWD load drops were applied at each test location.

3.4 Determination of Testing Parameters

3.4.1 Load Application History

Trafficking started on test Lane 1 on August 27, 2014, and finished on March 18, 2015. Thirty-four sets



Figure 3.28 Falling weight deflectometer and test set-up.

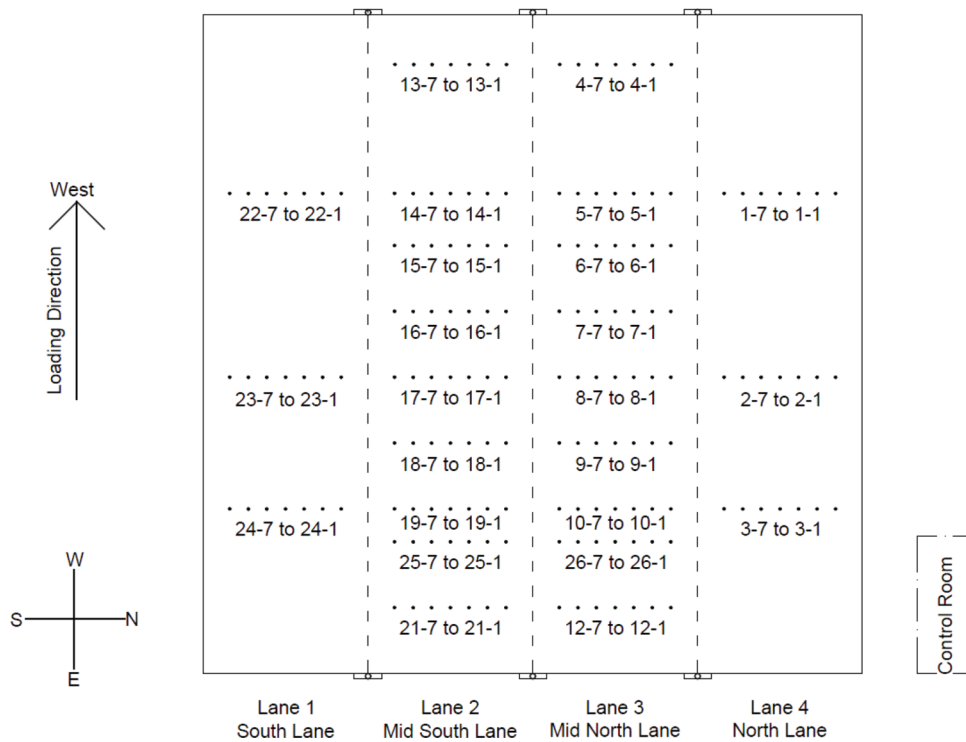


Figure 3.29 Falling weight deflectometer test locations.

of transverse and longitudinal profiles were recorded over 50,000 load applications. A LWD test and ultrasonic pulse velocity test were performed along with taking profile measurements to evaluate the pavement's *in situ* modulus evolution. Trafficking on test Lane 4 started on July 7, 2015 and finished on October 9, 2015, and trafficking on test Lane 3 started on November 25, 2015 and finished on December 12, 2015. For the Lane 4 and Lane 3 tests, the LWD test and ultrasonic pulse velocity test were performed only at load applications 0, 50, 200, 600, 1,500, 3,000, 7,500, 15,000, 35,000 and 50,000. Appendix B provides detailed load histories.

3.4.2 Test Temperatures

The test temperatures were determined based on the design high pavement temperature that was derived from the mean average maximum air temperature for the hottest seven-day period within a 20-year period obtained from Delphi, IN weather station data. Pavement temperatures were then calculated using LTPP Bind software v. 3.1; Table 3.9 presents the results. The test temperature was determined as 117°F (47.22°C) at a depth of 1.5 inches (3.81 cm), as shown in Figure 3.30.

The APT facility is equipped with a radiant heater that is able to heat the ambient temperature to 100°F

(37.78°C); a higher temperature was achieved by placing eight heat lamps beside the test lane, as shown in Figure 3.31 (a). To protect the laser profiling system and tires from being overheated by the lamps, foam shields were installed at each side of the loading wheel. A thermal image of a heated test lane, shown in Figure 3.31 (b), indicates that the pavement surface temperature was distributed uniformly over most portions of the test lane, except for cooler areas at the east and west ends and hotter areas along the north and south edges.

TABLE 3.9
Pavement Temperatures

Depth (mm)	High Temp (°F)	Low Temp (°F)
0	123.98	1.58
25	118.76	5.00
50	115.16	6.98
75	112.46	8.42
100	110.12	9.50
125	108.32	10.40
150	106.70	11.12

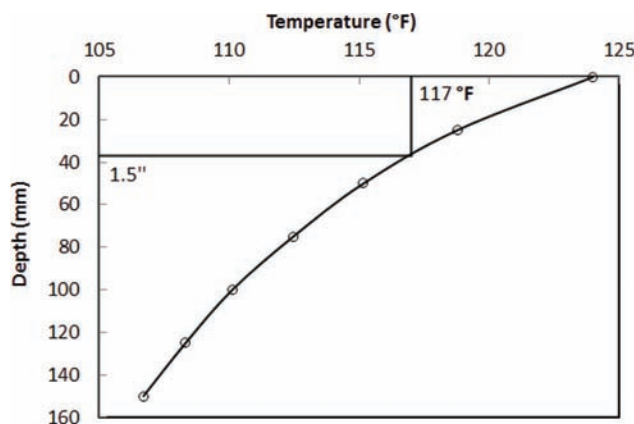


Figure 3.30 Pavement temperatures.

3.4.3 Load Level Calibration

The APT loading frame consists of a full-scale half single-axle with dual tires. The tires are typical truck tires with dimensions of 11R22.5. The width of the tire contact area is eight inches and the center-to-center spacing between the two tires is 13.5 inches (34.29 cm). The loading frame is able to provide an axle load from 2,000 lb (907 kg) to 20,000 lb (9.07 ton). The testing load level was determined as 9,000 lb (4.08 ton) to simulate the standard axle load of 18,000 lb (8.16 ton). Tire pressure was chosen as 100 psi (0.69 MPa). Prior to test lane trafficking, the tire footprint was measured to calculate the contact area, and the applied load magnitude was calibrated using a scale to measure the actual load underneath the tires as shown in Figure 3.32 (a) and (b).

The contact area was 58.59 square inches (378.00 square cm). Table 3.10 and Figure 3.33 provide the load level calibration data in table and graph formats, respectively. To achieve a 9,000-lb (4.08 ton) axle load, the input load level was chosen as 9,315 lb (4.23 ton).

The APT loading frame is able to apply either unidirectional or bidirectional traffic loads at a maximum speed of 5 mph (8.05 km/h). Unidirectional tire movement was used in this APT project. As shown in Figure 3.34, the loading frame needs five feet (1.52 m) to accelerate to maximum speed and three feet (0.91 m) to stop; the constant speed zone is 15 feet (4.57 m). One full load cycle takes about 11 seconds.

3.5 Test Results and Interpretation

3.5.1 Permanent Deformation at Surface

3.5.1.1 Characteristics of Pavement Profile. Figure 3.35 presents a typical pavement surface transverse profile. The elevations of the pavement surface refer to

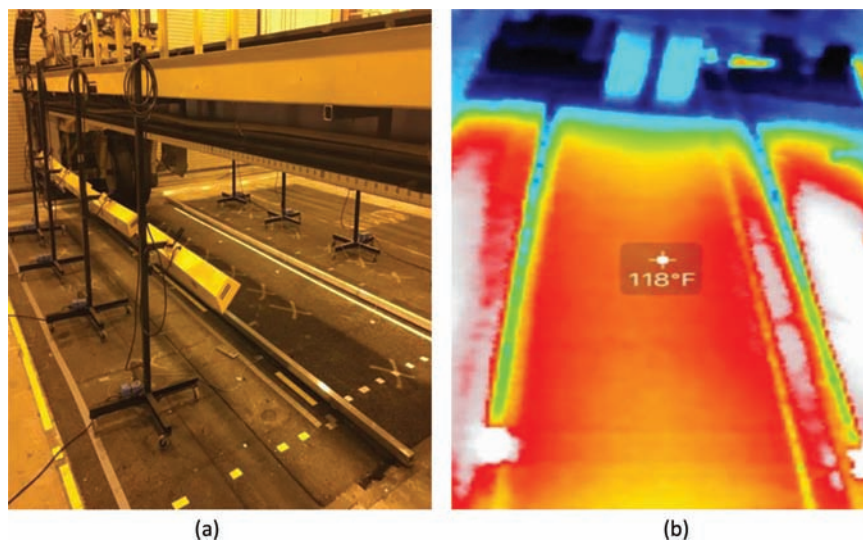


Figure 3.31 (a) Heating lamp placement and (b) thermal image of heated test lane.

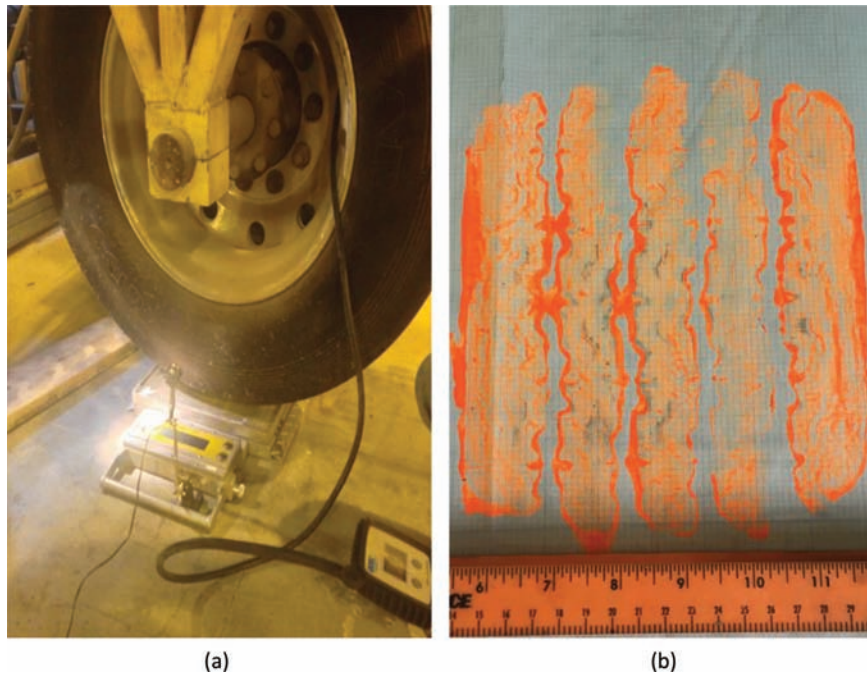


Figure 3.32 (a) Applied load calibration and (b) tire footprint.

TABLE 3.10
Load Calibration Data

1st		2nd		3rd		Average	
Applied	Measured	Applied	Measured	Applied	Measured	Applied	Measured
1740	1620	1740	1520	1740	1500	1740	1547
3566	3580	3566	3570	3566	3560	3566	3570
5392	5350	5392	5340	5392	5320	5392	5337
7218	7120	7218	7110	7218	7090	7218	7107
9044	8920	9044	8900	9044	8880	9044	8900
10870	10690	10870	10670	10870	10660	10870	10673
12696	12450	12696	12440	12696	12410	12696	12433
14522	14110	14522	14070	14522	14060	14522	14080
16348	15680	16348	15650	16348	15640	16348	15657
18174	17250	18174	17190	18174	17180	18174	17207
20000	18700	20000	18570	20000	18100	20000	18457

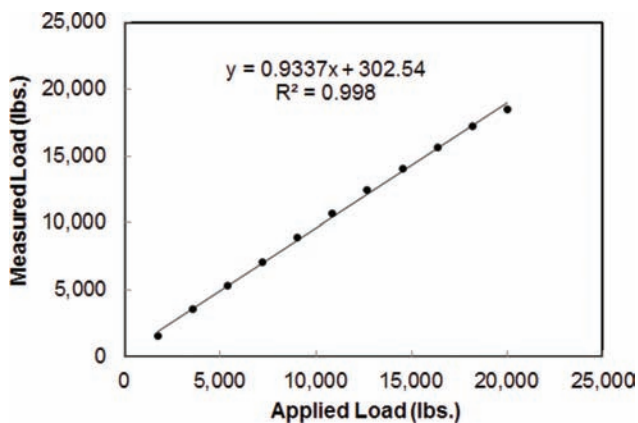


Figure 3.33 Load calibration data.

an imaginary datum about 225 mm (8.86 inch) below the pavement surface. The profile measured by a laser scanner with high resolution and accuracy (i.e., 0.15 mm (0.00590 inch) accuracy and 0.16 mm (0.00630 inch)/data point) captured the pavement surface texture that reflected the aggregate arrangement and compaction. As discussed earlier, the longitudinal orientation of the laser profiler is controlled by the APT load frame. Due to limitations of its positioning accuracy, each transverse profile might not be positioned at the exact requested location, and the actual scanning location could be at any point within 10 mm (0.39 inch) around the requested location. Consequently, quantifying the characteristics of the profiles is difficult. Data filtering was performed to smooth the raw profile data. A percentile filter with a 19-mm (0.75 inch)

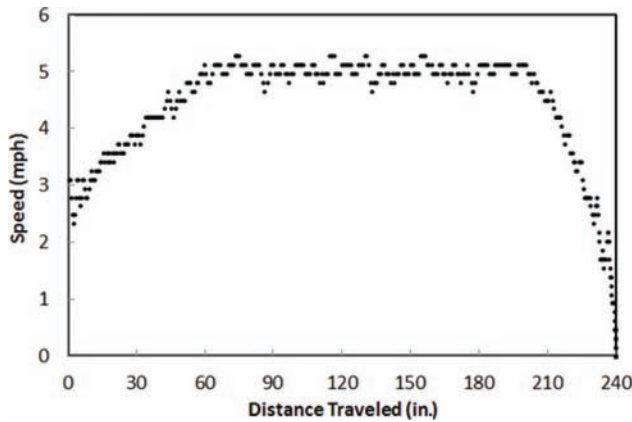


Figure 3.34 APT load speed record.

sampling window (i.e., twice the aggregate size) and 90th percentile were applied to all data. Figure 3.35 presents comparisons between the original and filtered data (not to scale).

Two parameters typically are used to define pavement rutting. First, permanent deformation, as shown in Figure 3.35, is defined as the maximum difference in elevation between the original and deformed pavement surface caused by APT loading. Permanent deformation is negative when the deformed surface is lower than the original surface; i.e., depression is evident. The second parameter is rut depth, as shown in Figure 3.36, according to AASHTO R 48 (2013), *Standard Practice for Determining Rut Depth in Pavements*. This definition has been widely used by local agencies in their PMS for pavement evaluation. In this study, this definition was used consistently to compare and analyze the rutting performance of the test sections and field roadway segments.

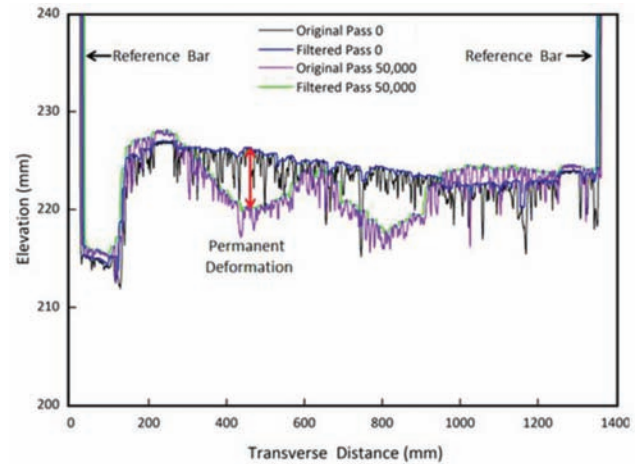


Figure 3.35 Sample transverse profile.

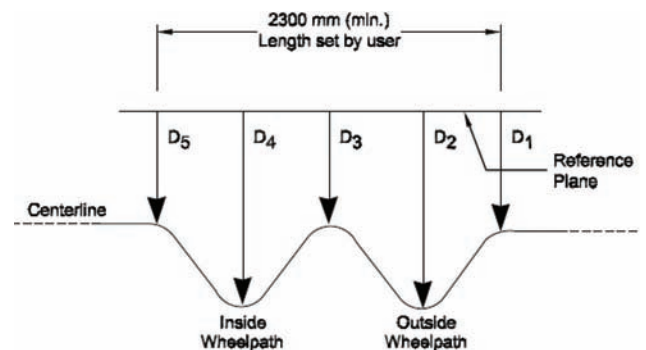


Figure 3.36 Definition of rut depth (AASHTO R 48, 2013).

structure but different surface course materials. The null hypotheses are:

- No difference is evident between the average means of the permanent deformation measured at Lane 1 and Lane 4, or the mean difference between the means is zero.
- No difference is evident between the average means of the permanent deformation measured at Lane 3 and Lane 4, or the mean difference between the means is zero.

$$R_i = D_2 - \frac{D_1 + D_3}{2}$$

$$R_o = D_4 - \frac{D_3 + D_5}{2} \quad (3.2)$$

where:

- R_o = rut depth outside wheel path estimate;
- R_i = rut depth inside wheel path estimate; and
- D_1, D_2, \dots, D_5 = height measured as shown in Figure 3.36.

Figures 3.37, 3.38, and 3.39 present the permanent deformations measured from test Lane 1, Lane 4, and Lane 3.

Table 3.11 provides a summary of the total permanent deformation after 50,000 APT load applications.

3.5.1.2 Interpretation of Test Results. Statistical analyses were performed to compare the test results obtained from Lane 1 and Lane 4, which have the same paving materials but different pavement structures, and from Lane 3 and Lane 4, which have the same pavement

At the 95 percent confidence level, the calculated two-tail p-value for the first hypothesis is 0.1211. Thus, the null hypothesis is accepted, and no significant difference exists between the permanent deformations measured at Lane 1 and Lane 4. This finding agrees with practice experience and previous research that indicate that the permanent deformation within asphalt concrete does not increase with an increase in pavement thickness once the pavement is sufficiently thick. Uge and van de Loo (1974) found the threshold value in their cases to be 5.12 inches (13.00 cm).

The p-value for the second hypothesis is 2.83E-06. Thus, the null hypothesis is rejected, and significant difference exists between the permanent deformations measured at Lane 3 and Lane 4. This finding agrees with expectations, because Lane 3 was constructed using an SMA surface course that has better rutting resistance

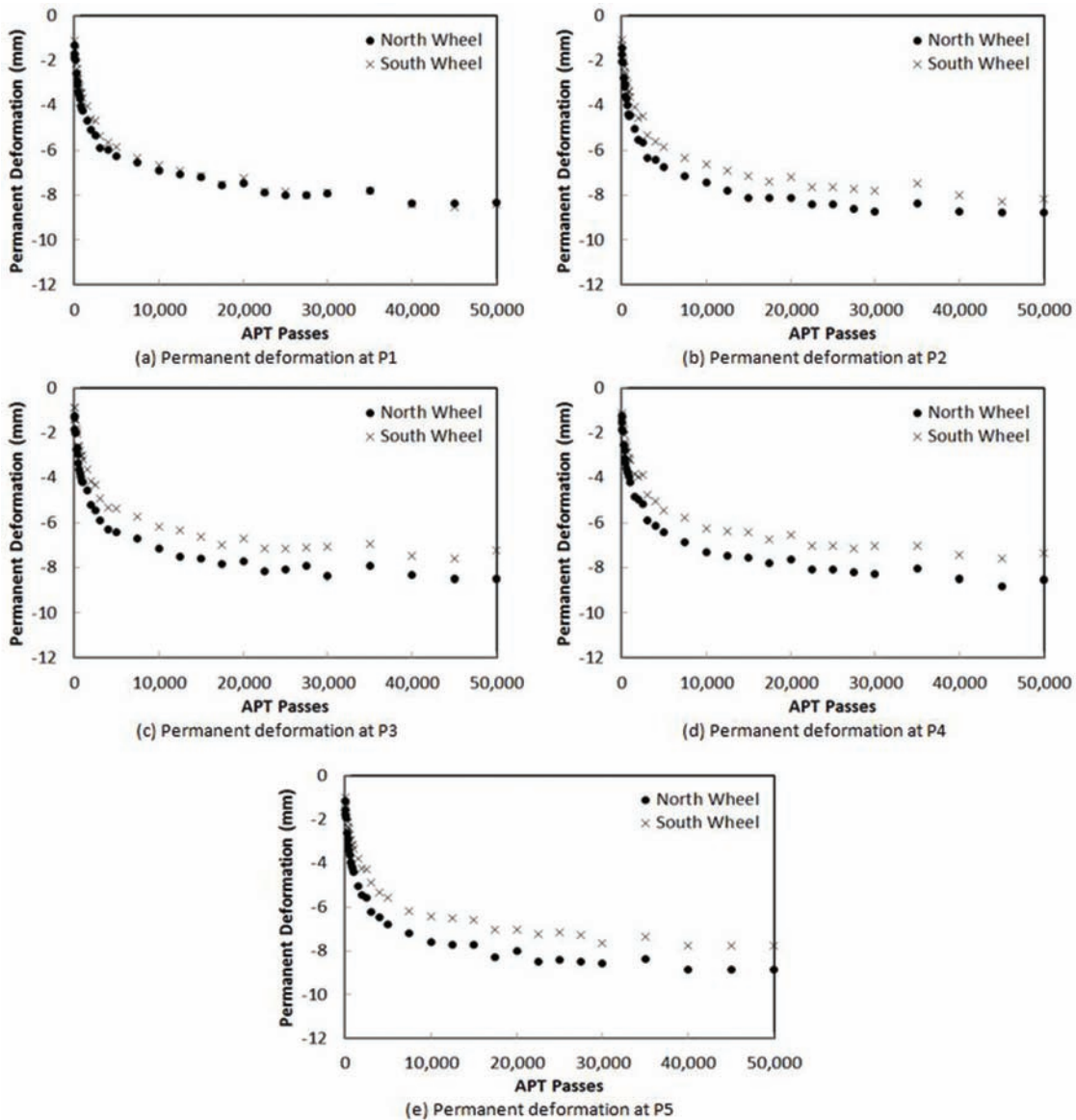


Figure 3.37 Lane 1 permanent deformation evolution.

than a regular dense-graded pavement. The permanent deformation measured in the SMA test lane is 46.2 percent less than that measured for a regular dense-graded surface course test lane.

3.5.2 Permanent Deformation for Individual Layers

3.5.2.1 Characteristics of Layer Deformation. Several parameters were used to characterize layer-wise deformation. The mid-depth rut is defined as the difference in elevation between the original and deformed interfaces at each depth. A negative value indicates depression, which means that the elevation decreased. Layer permanent deformation values were obtained by subtracting the elevation change in the bottom interface of the layer from that of the top interface. The permanent strain was calculated by normalizing the layer

permanent deformation with the layer thickness. The subgrade permanent deformation was calculated based on the assumption that the bottom interface of the subgrade layer was not deformed at all.

3.5.2.2 APT Results of Layer Deformation. Figure 3.40 and Figure 3.41 provide the mid-depth rut data for Lane 1 and Lane 4, respectively. A series of rutting prediction models based on logarithmic regression were developed to describe the data shown in the plots. Those prediction models were used for the data interpretation described in Section 3.5.2.3 in order to minimize the effects of measurement accuracy-related error. Figure 3.42 and Figure 3.43 present the layer permanent deformation and permanent strain results.

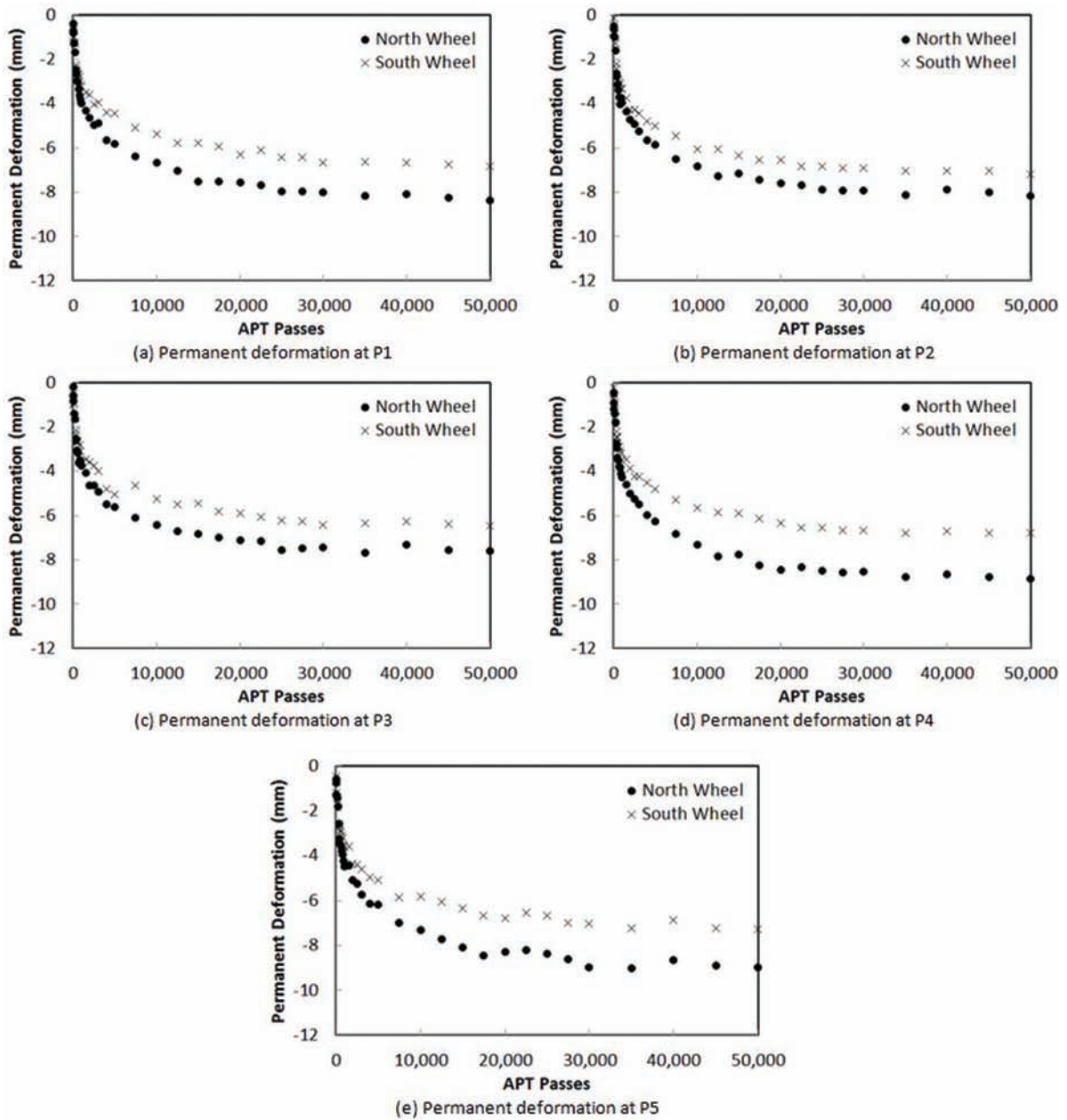


Figure 3.38 Lane 4 permanent deformation evolution.

The mid-depth ruts were measured only at the bottom of the surface layer and the top of the subgrade in Lane 3. In order to reconstruct the rutting distribution curve, it was assumed that the rutting distribution within the intermediate layer, upper base layer, OG layer, and lower base layer of Lane 3 was the same as that of Lane 4. This assumption was believed to be reasonable because Lane 3 and Lane 4 share the same paving materials and pavement structure, with only different surface layer materials.

Deformations within the lower four layers (i.e., the intermediate layer, upper base layer, OG layer, and lower base layer) of Lane 3 were calculated first using

the measured mid-depth ruts at 1.5 inches (3.81 cm) and 12.5 inches (31.75 cm). The deformations then were distributed among the lower four layers using the percentages found from Lane 4. Using the derived layer deformation, mid-depth rutting curves were constructed and layer permanent strains were calculated. Figure 3.44 and Figure 3.45 provide these derived Lane 3 data for the mid-depth rut measurements and the permanent deformations and permanent strains, respectively.

3.5.2.3 Interpretation of Test Results. Table 3.12 presents the distribution of the permanent deformation

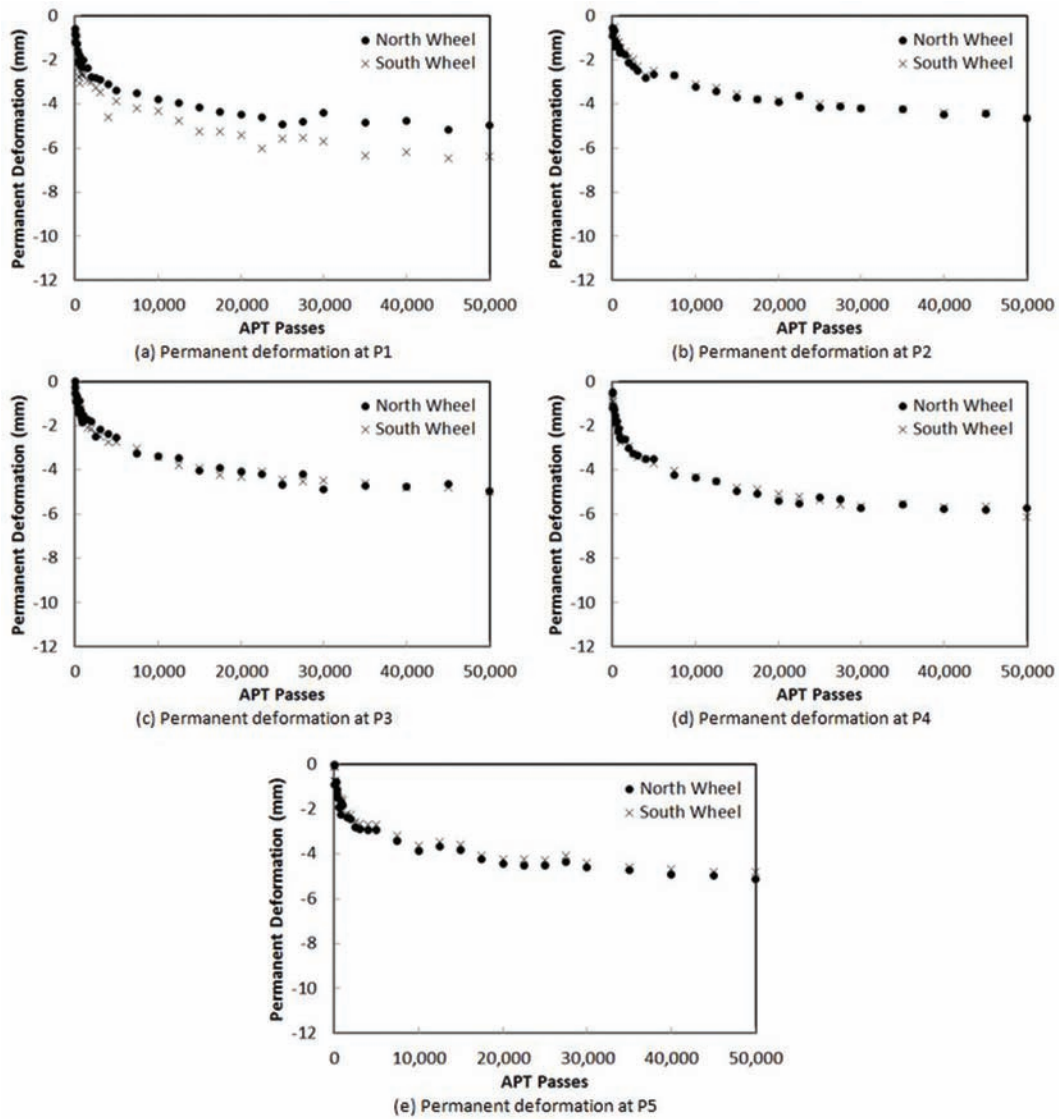
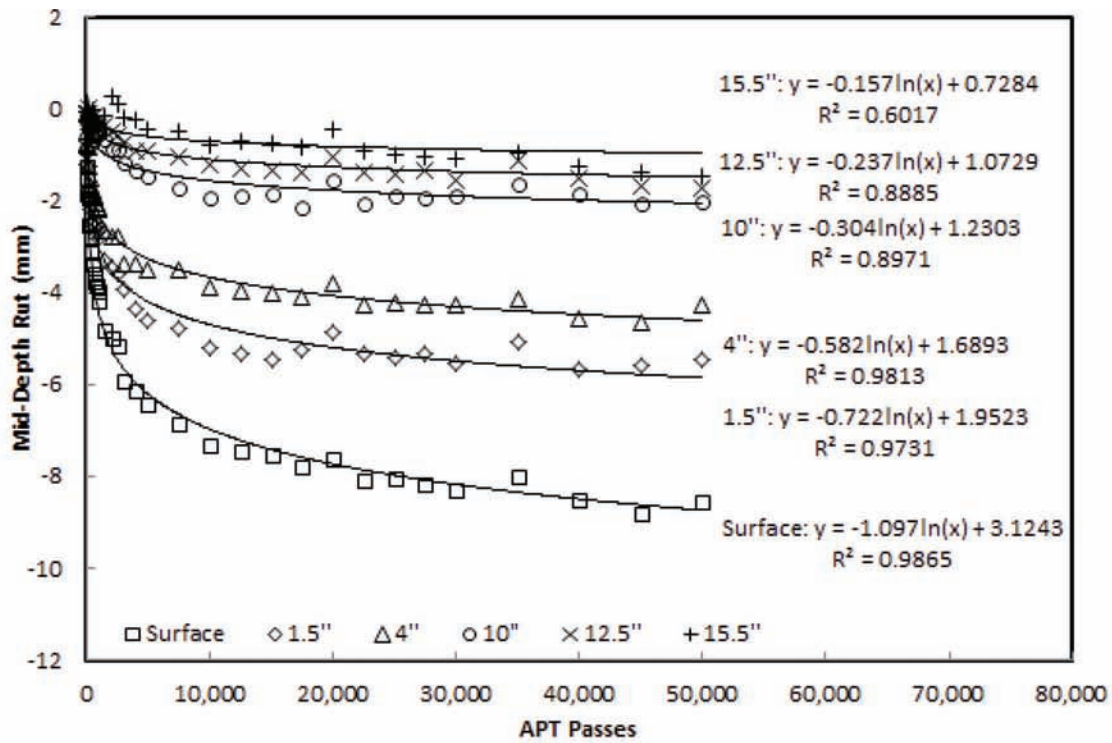


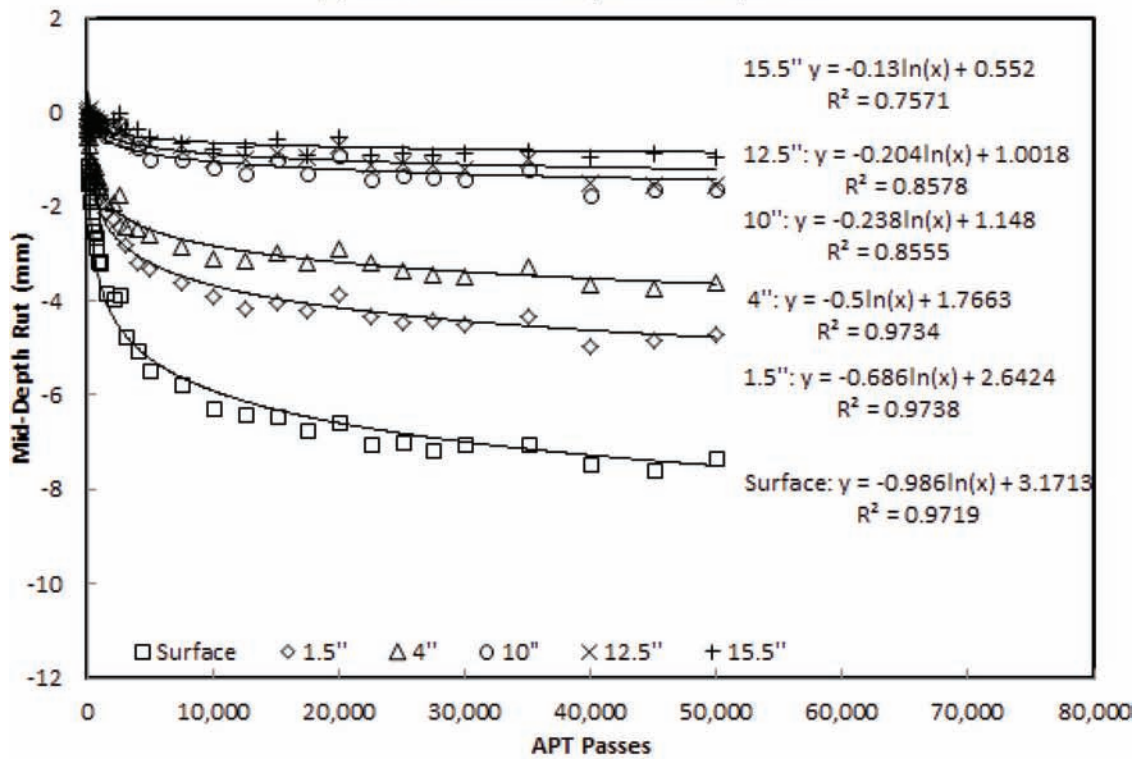
Figure 3.39 Lane 3 permanent deformation evolution.

TABLE 3.11
Permanent Deformation Summary

Measurement Location		Permanent Deformation (mm)		
		Lane 1	Lane 3	Lane 4
North wheel	P1	-8.32	-4.98	-8.37
	P2	-8.76	-4.65	-8.18
	P3	-8.48	-4.96	-7.59
	P4	-8.54	-5.75	-8.86
	P5	-8.86	-5.12	-8.99
South Wheel	P1	-8.41	-6.40	-6.84
	P2	-8.17	-4.64	-7.19
	P3	-7.23	-4.99	-6.48
	P4	-7.35	-6.13	-6.80
	P5	-7.91	-4.79	-7.29
Mean		-8.20	-5.24	-7.66
Standard Deviation		0.552	0.627	0.889



(a) Lane 1 north wheel path mid-depth ruts

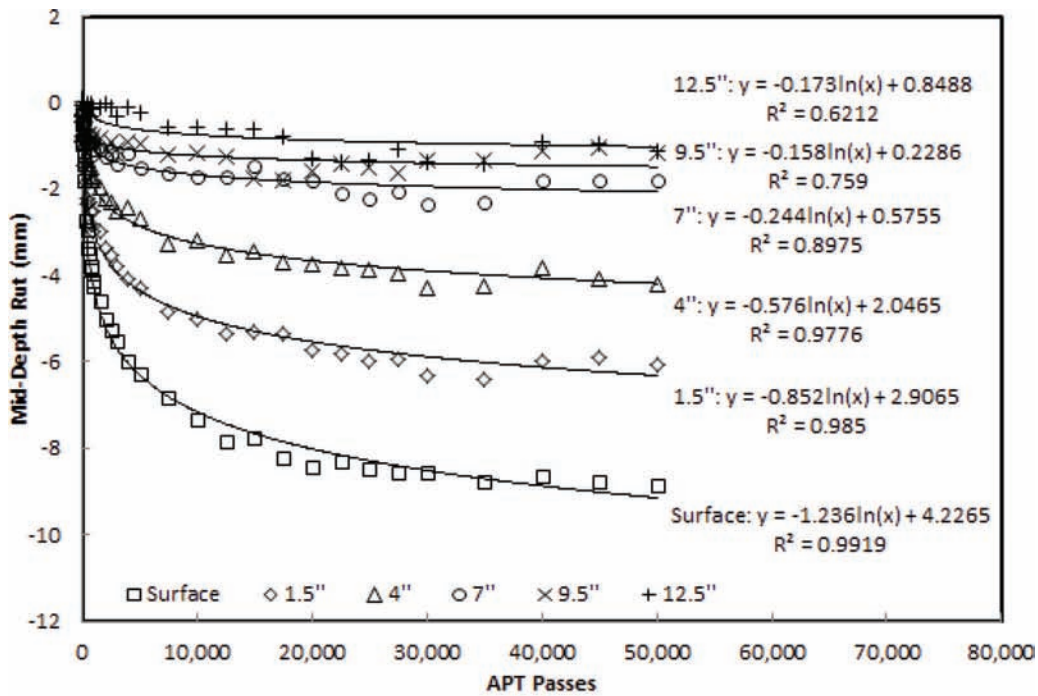


(b) Lane 1 south wheel path mid-depth ruts

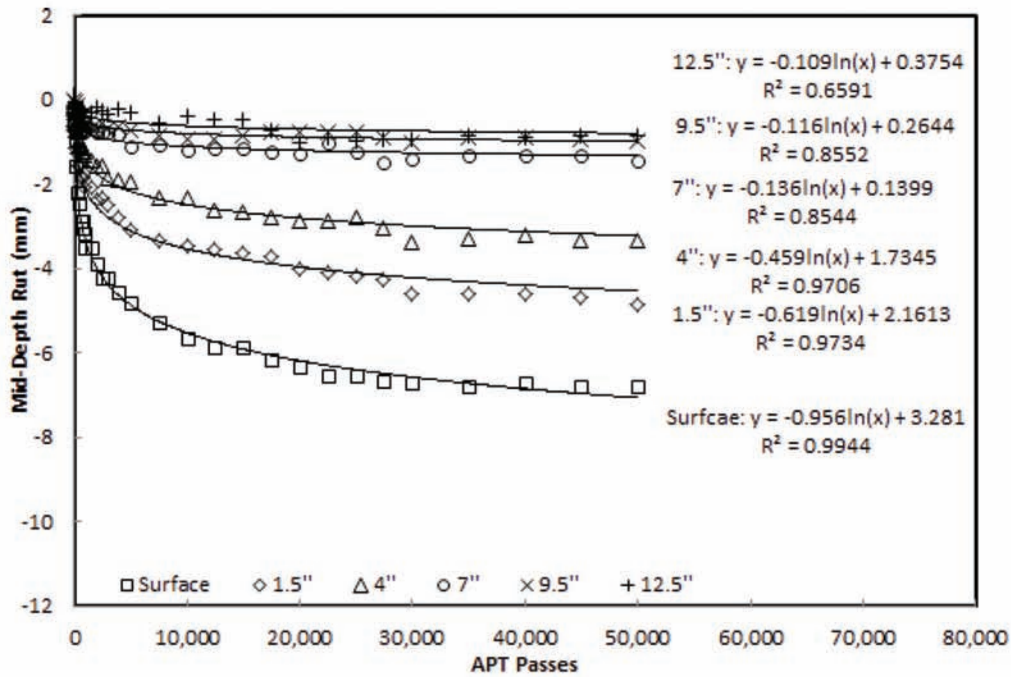
Figure 3.40 Lane 1 mid-depth ruts.

within the pavement layers. The distribution was derived at 50,000 APT load applications based on the developed rutting prediction model.

This study found that most of the pavement rutting was caused by the deformation of the asphalt concrete. The primary portion of the rutting occurred at the upper



(a) Lane 4 north wheel path mid-depth ruts



(b) Lane 4 south wheel path mid-depth ruts

Figure 3.41 Lane 4 mid-depth ruts.

asphalt concrete layers, with about half of the rutting observed within the top four inches of the pavement. This finding agrees with previous research and experience. For example, Hofstra and Klomp (1972) reported that permanent deformation in flexible pavements is greatest near the pavement surface and gradually decreases with depth.

This study also found that, regardless of pavement thickness and paving material, the subgrade deformation remained at a very low level; only about 11 percent of rutting occurred in the subgrade. As a surface course material, SMA has much greater rutting resistance than a regular dense-graded mix; in this study, the amount of rutting in the SMA surface course was

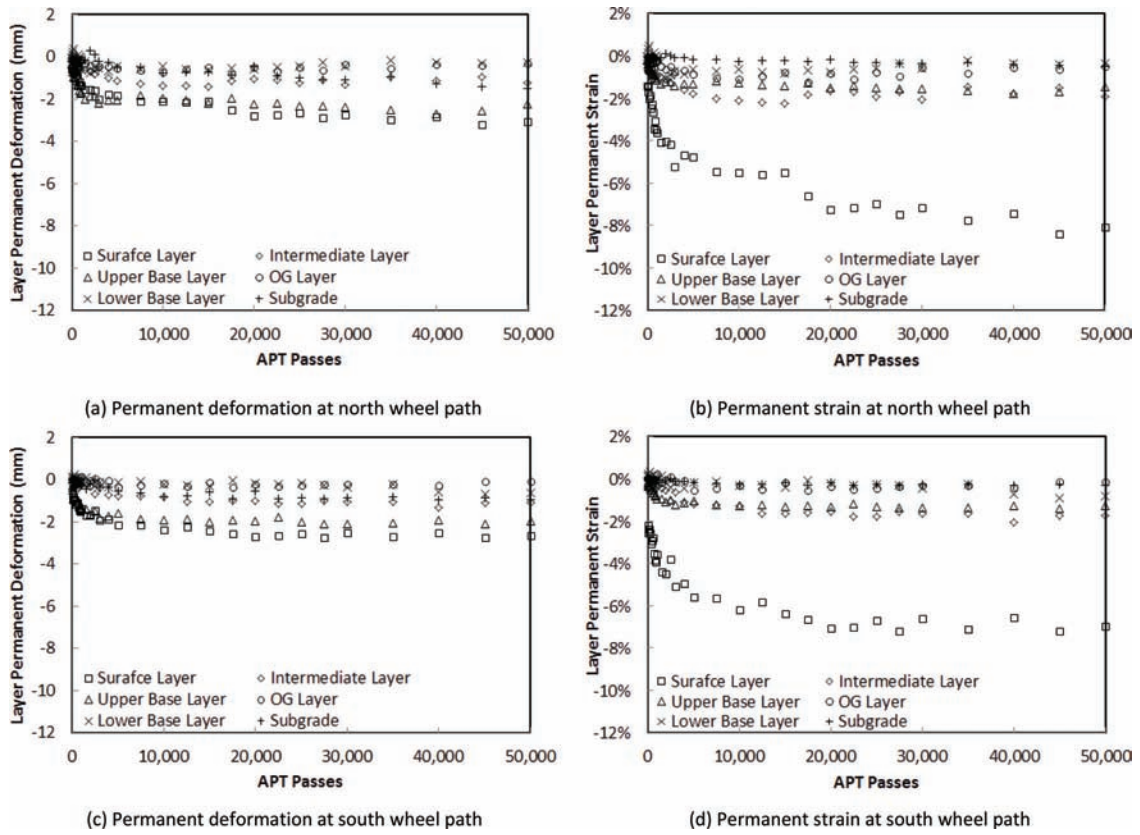


Figure 3.42 Lane 1-layer permanent deformation and permanent strain.

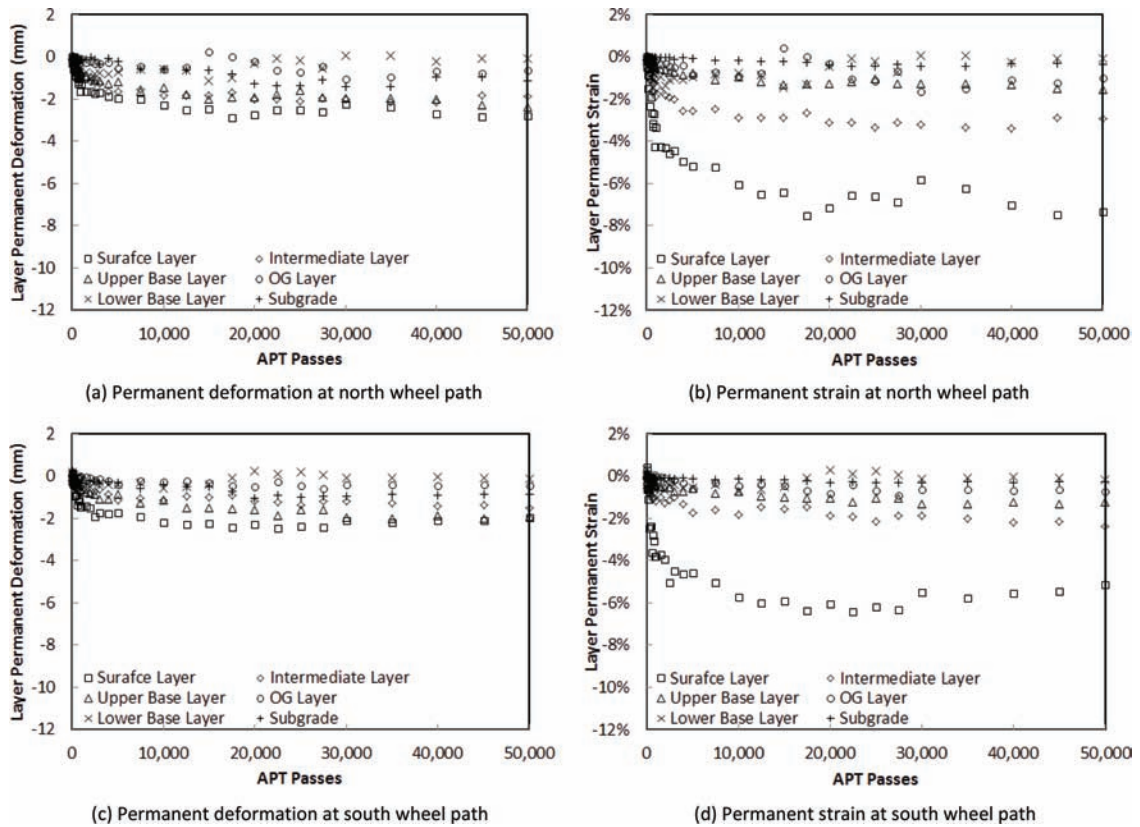
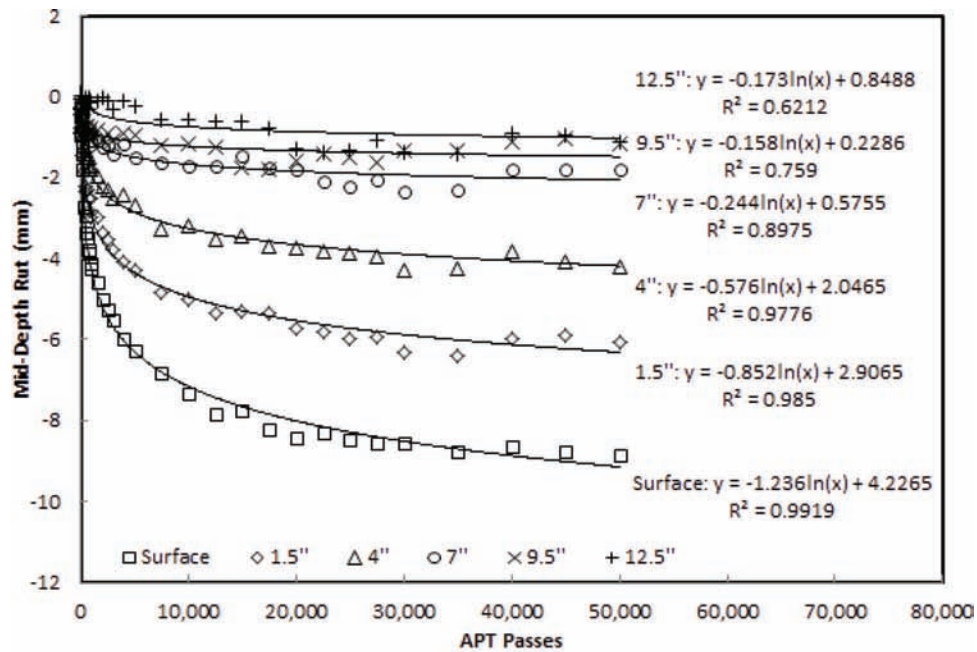
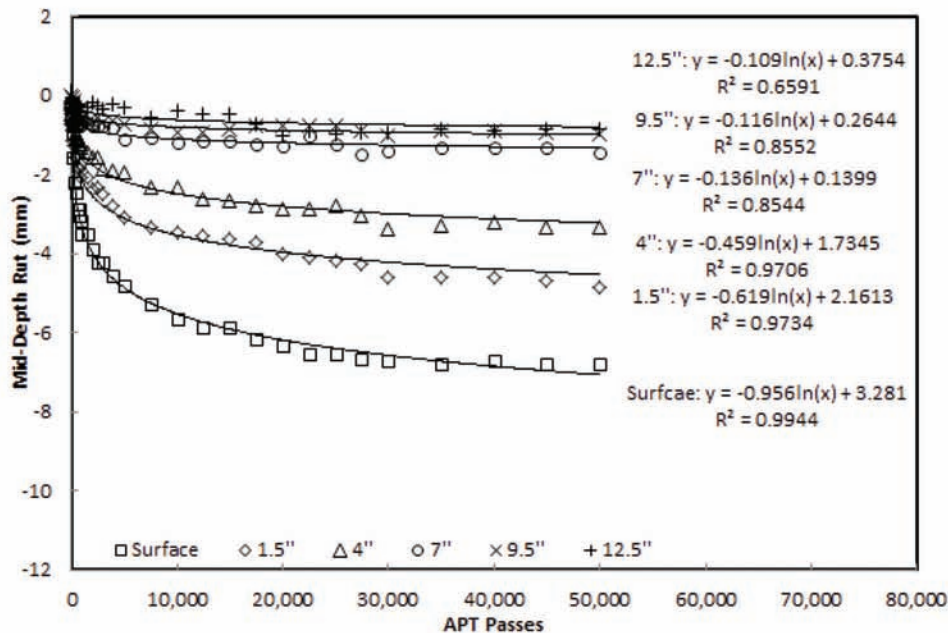


Figure 3.43 Lane 4-layer permanent deformation and permanent strain.



(a) Lane 4 north wheel path mid-depth ruts



(b) Lane 4 south wheel path mid-depth ruts

Figure 3.44 Lane 3 mid-depth ruts.

reduced by around 75 percent. The critical rutting location thus migrated from the surface layer to the intermediate layer.

3.5.3 Pavement Structure Evaluation Using Falling Weight Deflectometer

The test sections were kept at a high temperature during the entire testing period. When a test lane was being loaded, eight heating panels were used to heat the

test lane up to 117°F (47.22°C) at a 1.5-inch (3.81 cm) depth. Leaving asphalt concrete in this environment for such a long time could cause the material to become aged or conditioned. As a result, the material could harden, and the degree of hardening varies and depends on the aging time. To account for the effect of hardening properly, FWD tests were performed to quantify the amount of hardening that occurred during APT loading. Test Lane 1 and Lane 4 were used to evaluate the hardening effects at 117°F (47.22°C) that were due

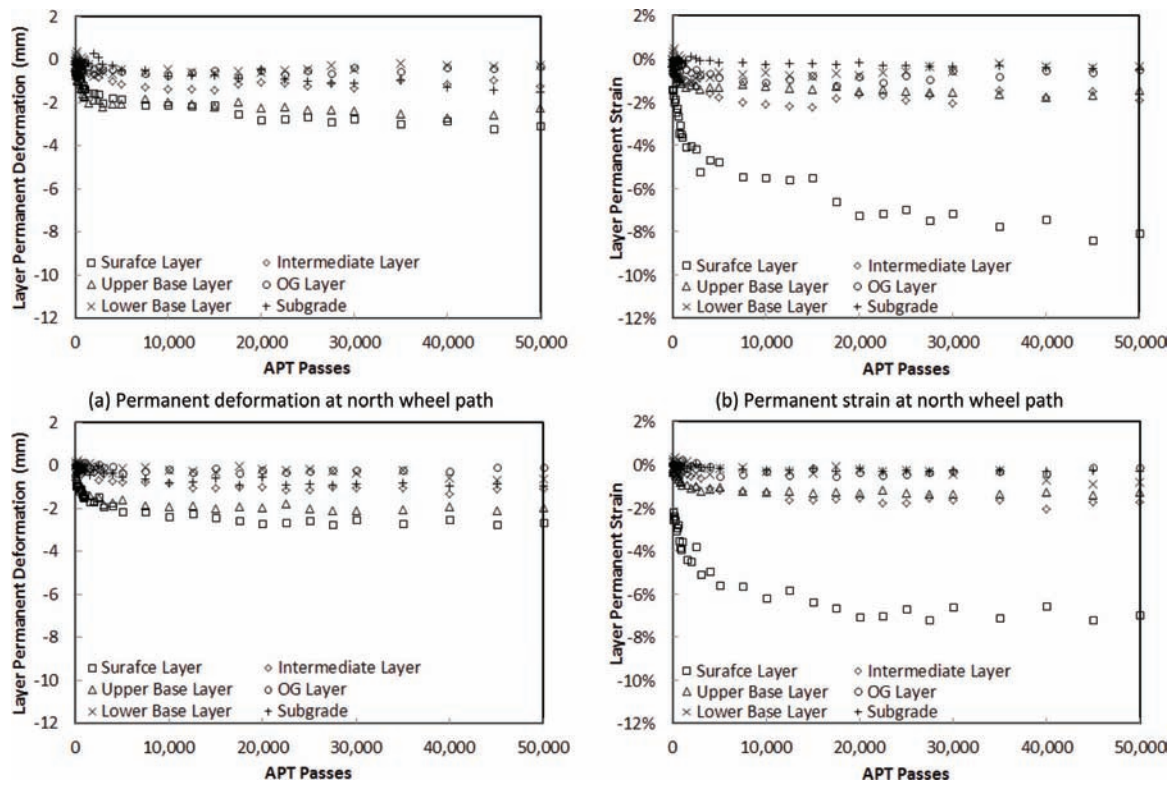


Figure 3.45 Lane 3-layer permanent deformation and permanent strain.

TABLE 3.12
Layer-Wise Permanent Deformation Distribution

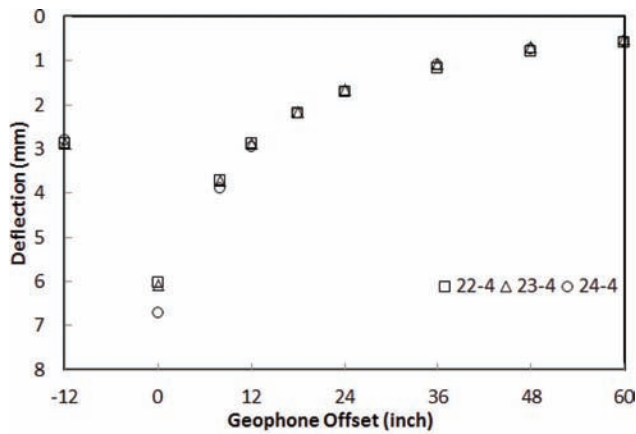
Layer	Lane 1		Lane 3		Lane 4	
	North Wheel Path	South Wheel Path	North Wheel Path	South Wheel Path	North Wheel Path	South Wheel Path
Surface (%)	33.0	36.2	9.1	8.2	31.0	35.8
Intermediate (%)	14.3	15.2	33.3	28.2	23.2	18.5
Upper Base (%)	29.1	29.6	32.4	38.8	23.2	26.9
OG (%)	6.5	3.0	9.0	7.8	6.4	4.8
Lower Base (%)	6.0	4.7	8.1	4.5	5.0	2.6
Subgrade (%)	11.1	11.4	8.1	12.5	11.2	11.4

TABLE 3.13
FWD Testing Temperatures for Lane 1 and Lane 4

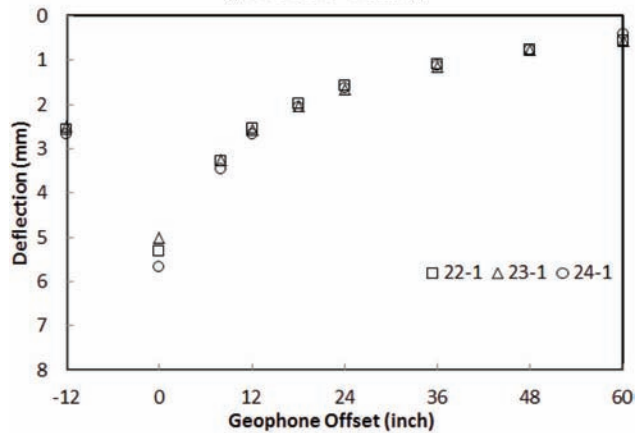
Depth	Lane 1 Temperature (°F)		Lane 4 Temperature (°F)	
	Prior to Loading 7/10/2014	After Loading 4/6/2015	Prior to Loading 3/31/2015	After Loading 10/15/2015
1.5 in.	117	117	118	119
4 in.	–	115	116	118
9.5 in.	–	–	109	113
12.5 in.	–	–	108	113
15.5 in.	–	108	–	–

to the heating panels. Table 3.13 presents the test temperatures. Figure 3.29 shows the test locations, and Figure 3.46 and Figure 3.47 provide the deflection data for Lane 1 and Lane 4, respectively.

It should be noted that the FWD tests were performed at the centerline of each test lane prior to APT loading. Once the test lanes were loaded, the test was performed at unloaded areas 20 1/4 inches (51.43 cm)



(a) Prior to APT loading



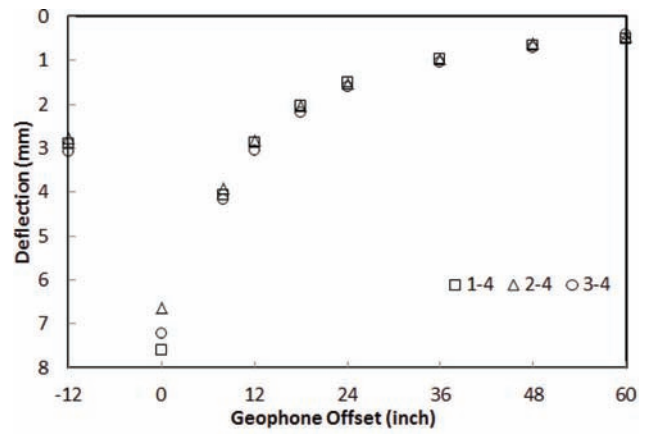
(b) After APT loading

Figure 3.46 Falling weight deflectometer deflections at Lane 1.

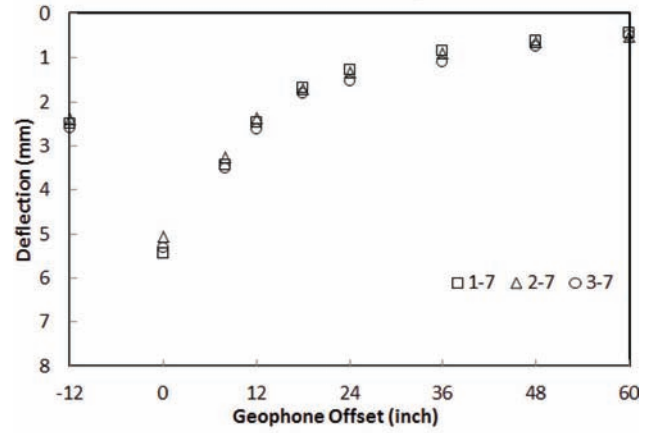
away from the centerline, which are denoted as locations ‘-7’ or ‘-1’ in Figure 3.29. Layer *in situ* moduli were back calculated using ELMOD v. 6. The five AC layers were treated as one single layer in the back calculation. The back calculated moduli are provided in Figure 3.48.

Statistical analyses were conducted to compare the back calculated moduli before and after APT loading for Lane 1 and Lane 4. It was found:

- For Lane 1, a significant difference was found between the back calculated moduli before and after APT loading



(a) Prior to APT loading



(b) After APT loading

Figure 3.47 Falling weight deflectometer deflections at Lane 4.

at the 95 percent confidence level; the calculated p-value is 4.38E-05. The mean moduli increased from 217,965 psi (1,503 MPa) to 276,832 psi (1,908 MPa), indicating about 27 percent increase.

- For Lane 4, a significant difference was found between the back calculated moduli before and after APT loading at the 95 percent confidence level; the calculated p-value is .03E-07. The mean moduli increased from 186,077 psi (1,283 MPa) to 273,991 psi (1,889 MPa), indicating about 47 percent increase.

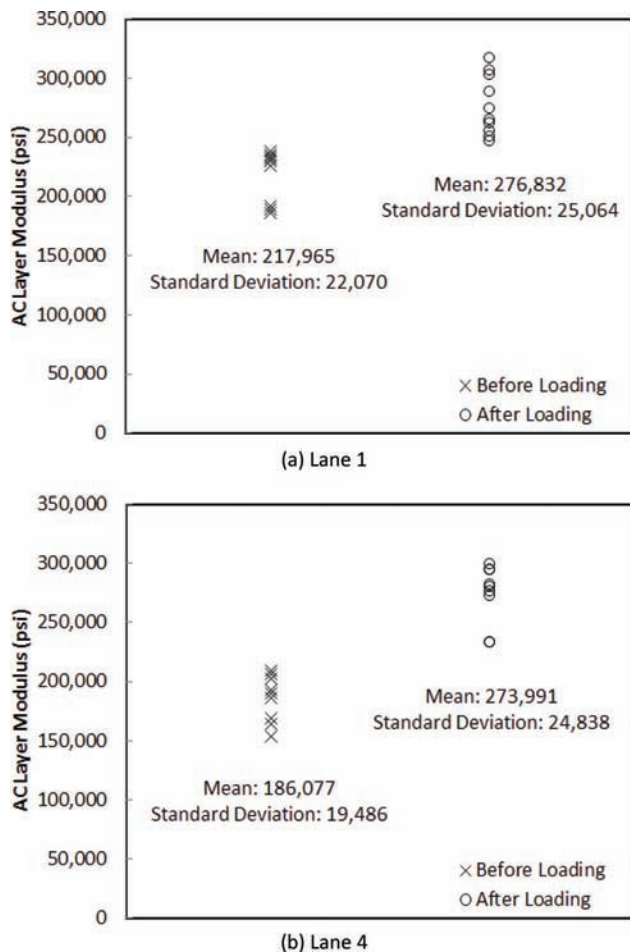


Figure 3.48 Back calculated asphalt concrete layer moduli.

4. MEPDG INPUT PREPARATION

4.1 Introduction

As discussed in Chapter 1, the MEPDG uses hierarchical input levels based on the designer's knowledge and the availability of the input parameters. Three input levels are used to characterize the material and traffic properties:

- Level 1 is the highest input level in which all parameters are measured directly from laboratory or field tests.
- Level 2 input parameters are calculated from other site-specific data or information using correlations or regression equations.
- Level 3 input parameters are estimated from global or regional default values.

The selection of an input level depends on current test capabilities, construction specifications, and data collection procedures. The selected input level for the local calibration process should be consistent with the future pavement design and analysis. The MEPDG local calibration is sensitive to input parameters and has a

significant influence on the accuracy and precision of calibrated transfer functions.

4.2 Field Section Selection

4.2.1 Selection Criteria

As recommended by NCHRP 1-37A, local calibration should be performed based on local data that represent local materials, construction practices, environmental conditions, and traffic conditions. The purpose of local calibration experimental design is to establish statistically sound estimates and to minimize bias and standard error between predicted and measured distresses. The research team for the NCHRP 1-37A project also recommended that several critical factors should be taken into account in the local calibration experimental design. Each factor, as it relates to this study, is described briefly as follows.

- *Traffic level* should be treated as one of the most important factors in the experimental design.
- *HMA layer thickness* significantly affects the state of the stress and strain within the pavement structure and hence is used to determine the developed permanent deformation. This study focuses on full-depth flexible pavement. Given this focus, the thickness of the roadway segments is normally within a range of 12 inches (30.48) to 20 inches (50.8 cm).
- *Nonconventional materials* should be considered by varying the surface layer material, such as regular dense-graded mixtures and SMA material.
- *Pavement age* is closely related to asphalt long-term aging effects and environmental variations.
- *Subgrade soil type* helps to determine the potential for subgrade deformation.
- *Pavement structure* is typically another important factor, but the structures considered in this study do not have much variation because Indiana's full-depth flexible pavements have a standard five-layer structure.
- *Climate zone* typically is a critical factor, because the viscous property of asphalt concrete depends highly on pavement temperature. However, the State of Indiana has relatively uniformly distributed environmental conditions; thus, climate zone is not treated as a selection criterion in this study.
- *Rehabilitated pavements* were considered in this study to determine whether the use of various rehabilitation strategies creates any bias or accuracy issues. The calibrated prediction models will be used only to design and analyze new pavements with high priority; therefore, overlaid flexible pavements were not considered in the experimental design.

4.2.2 Data Set

The primary focus of this study is full-depth flexible pavements constructed with Superpave-designed mixtures; this restricted focus limits the number of available roadway segments. After a thorough search of the INDOT project database for the past ten years, eight

field projects along with three current APT sections and two previous APT sections were selected to create a MEPDG local calibration database. The use of full-scale APT sections can lead to lower standard error of the estimates due to well-controlled test conditions and measurement procedures. Without the complexities associated with long-term aging and environmental variations, the use of the APT sections served to supplement and reduce the number of field roadways that typically are required to minimize bias and standard error.

In summary, the selected field roadway segments contain five APT sections, three state roads, four US highways, and one interstate highway. These segments include various pavement structures, surface course materials, and traffic levels. Tables 4.1, 4.2, 4.3, and 4.4 and Figure 4.1 provide details about the selected segments. The subgrade treatment type shown in the tables is covered in detail in Section 5.5.2.

4.3 Climate Data

4.3.1 Input Data Requirements

The MEPDG considers the environmental effects on the material properties and pavement responses in a sophisticated manner. Because asphalt is a viscoelastic material, its properties depend directly on temperature. The MEPDG is able to update HMA modulus values every hour due to real-time changes in temperature. It integrates a climatic model, the EICM, to calculate the temperature and moisture content within each pavement layer as well as the subgrade soil on an hourly basis throughout the pavement design life. The EICM consists of three major models:

- The Climatic Materials Structural (CMS) Model developed at the University of Illinois (Dempsey, Herlach, & Patel, 1985)

TABLE 4.1
Roadway Segments: 1–3

ID	1	2	3
Route Name	APT Test Lane 1	APT Test Lane 3	APT Test Lane 4
Contract Number	–	–	–
Location	West Lafayette	West Lafayette	West Lafayette
Segment Length (mile)	0.0038	0.0038	0.0038
Date Opened to Traffic	8/27/2014	11/22/2015	7/20/2015
Surface Course	Dense	SMA	Dense
Pavement Structure	1.5 in. Surface 2.5 in. Intermediate 6 in. Base 2.5 in. OG 3 in. Base 12.5 in. SG (lime-treated A-6)	1.5 in. Surface 2.5 in. Intermediate 3 in. Base 2.5 in. OG 3 in. Base 15.5 in. SG (lime-treated A-6)	1.5 in. Surface 2.5 in. Intermediate 3 in. Base 2.5 in. OG 3 in. Base 15.5 SG (lime-treated A-6)
Pavement Thickness (in.)	15.5	12.5	12.5
Speed (MPH)	5	5	5
AADTT	2500	2500	2500
Truck Percentage	100.0	100.0	100.0

TABLE 4.2
Roadway Segments: 4–6

ID	4	5	6
Route Name	Previous APT Lane 1	Previous APT Lane 2	SR-43
Contract Number			25550
Location	West Lafayette	West Lafayette	From 1.16 Miles North of I-65 to 1.93 Miles North of I-65
Segment Length (mile)	0.0038	0.0038	0.77
Date Opened to Traffic	1/28/2008	8/4/2008	11/26/2008
Surface Course	Dense	Dense	Dense
Pavement Structure	2 in. Surface 3 in. Intermediate 12 in. Base 16 in. SG (cement-treated A-4)	2 in. Surface 3 in. Intermediate 9 in. Base 16 in. SG (cement-treated A-4)	1.5 in. Surface 2.5 in. Intermediate 4 in. Base 2.8 in. OG 3 in. Base SG Type IA
Pavement Thickness (in.)	17	14	13.8
Speed (MPH)	5	5	60
AADTT	2500	2500	1,188
Truck Percentage	100.0	100.0	9.9

TABLE 4.3
Roadway Segments: 7–9

ID	7	8	9
Route Name	SR-28	US-41	SR-43
Contract Number	27265	28441	29399
Location	From I-65 to County Road 350 west	From 0.6 Mile South of US-36 to 2.1 Miles North of US-36	From 0.27 Mile South of I-65 to I-65
Segment Length (mile)	4.97	2.77	0.27
Date Opened to Traffic	10/26/2007	9/30/2008	11/30/2009
Surface Course	Dense	Dense	Dense
Pavement Structure	1.5 in. Surface 2.5 in. Intermediate 4 in. Base 3.4 in. OG 4 in. Base SG Type IA	1.5 in. Surface 2.5 in. Intermediate 4 in. Base 2.3 in. OG 3 in. Base SG Type IA	1.5 in. Surface 2.5 in. Intermediate 11.5 in. Base SG Type IA
Pavement Thickness (in.)	15.4	13.4	15.5
Speed (MPH)	60	45	60
AADTT	1,236	332	1,067
Truck Percentage	18.2	5.4	7.5

TABLE 4.4
Roadway Segments: 10–13

ID	10	11	12	13
Route Name	US-40	I-465	US-421	US-31
Contract Number	29133	29137	29320	29310
Location	From Franklin Road to Grassy Creek	North of I-74 to North of 56th Street	US-421 from SR-3 to Michigan Road	From SR-110 to SR-10
Segment Length (mile)	2.32	2.65	1.36	4.81
Date Opened to Traffic	11/2/2009	10/21/2009	7/7/2008	10/1/2007
Surface Course	Dense	SMA	Dense	Dense
Pavement Structure	1.5 in. Surface 2.5 in. Intermediate 4 in. Base 3.2 in. OG 4.5 in. Base SG Type IV	1.5 in. Surface 2.5 in. Intermediate 5.5 in. Base 3.6 in. OG 5.5 in. Base SG Type IA	1.5 in. Surface 2.5 in. Intermediate 4 in. Base 3.5 in. OG 4 in. Base 12 in. SG (stabilized A-6)	2 in. Surface 3 in. Intermediate 12 in. Base 16 in. SG (cement-treated A-4)
Pavement Thickness (in.)	15.8	18.6	15.5	17
Speed (MPH)	40	75	45	68
AADTT	1,701	14,463	579	4,139
Truck Percentage	6.7	14.3	8.3	29.4

- The CRREL Frost Heave and Thaw Settlement Model (CRREL Model) developed at the United States Army Cold Regions Research and Engineering Laboratory (Guymon, Berg, & Johnson, 1986)
- The Infiltration and Drainage (ID) Model developed at Texas A&M University (Lytton, Pufahl, Michalak, Liang, & Dempsey, 1990)

Both temperature and moisture content have a great impact on unbound materials. By calculating the temperatures within the unbound material, the month when the material is frozen can be determined and its resilient modulus thus can be adjusted according to freeze or thaw periods. The resilient modulus also can be adjusted in terms of the average monthly moisture content relative to the optimum moisture content.

Three outputs are provided by the EICM throughout the pavement design life for each pavement sublayer: (1) an unbound material resilient modulus adjustment factor, (2) the temperature at the surface and mid-point of each sublayer on an hourly basis, and (3) the average volumetric moisture content for each sublayer. To accomplish the climate analysis, the EICM requires six weather parameters on an hourly basis: (1) air temperature, (2) wind speed, (3) percentage of sunshine, (4) precipitation, (5) relative humidity, and (6) ground water table.

In addition, shortwave absorptivity is required to determine the amount of solar energy that is absorbed by the pavement surface. This parameter is used to define the heat flux boundary condition in the CMS



Figure 4.1 Roadway segment locations.

model. The color of the pavement surface affects short-wave absorptivity, and the MEPDG suggests using 0.9–0.98 (black) for fresh asphalt pavement and 0.8–0.9 (gray) for aged asphalt pavement.

4.3.2 Data Collection

For this study, the input data requirements described in Section 5.3.1 could be obtained from weather stations located near the project site. The INDOT has integrated the weather station data for the entire State of Indiana into a county-based database. Table 4.5 presents the weather data for each selected roadway segment. The APT sections have a well-controlled environment, so separate weather data were created to reflect the APT conditions. It would be ideal if the MEPDG could assign the temperature at each sublayer according to the measured values in the APT sections and force those values to be constant at all times throughout the analysis period. However, the MEPDG simulates realistic environmental conditions by considering daily and seasonal temperature and moisture variations. The controlled climate condition in the APT facility challenged the EICM. The most faithful simulation of the APT conditions was not allowed in the

TABLE 4.5
Weather Stations for Roadway Segments

Route Name	Contract Number	Weather Station
APT Test Lane 1	–	APT
APT Test Lane 3	–	APT
APT Test Lane 4	–	APT
Previous APT Test Lane 1	–	APT
Previous APT Test Lane 2	–	APT
SR-43	25550	Tippecanoe
SR-28	27265	Clinton
US-41	28441	Parke
SR-43	29399	Tippecanoe
US-40	29133	Marion
I-465	29137	Marion
US-421	29320	Decatur
US-31	29310	Marshall

MEPDG because the MEPDG does not allow the user either to turn off the EICM feature manually or modify the EICM output file to bypass this climate model.

In order to obtain the best simulations of the APT conditions, author generated a virtual weather station and adjusted the climatic parameters to achieve a constant representative temperature at all depths. Because the top portion of a pavement is more susceptible to rutting than its lower layers, it seemed logical to use the temperature at this upper portion as the representative temperature. The selected temperature was 117°F (47.22°C), which was the temperature 1.5 inches (3.81 cm) deep in the APT lanes. The APT weather data then were created using a constant air temperature of 117°F (47.22°C), and the wind speed, percentage of sunshine, and precipitation were set to be zero at all times. The relative humidity was 12 percent according to the measurement. The ground water table was set as 18 feet (5.49 m) because no water was introduced into the pavement system. Shortwave absorptivity was set to zero to maintain a constant temperature throughout the pavement depth.

4.4 Traffic Data

4.4.1 Input Data Requirements

Before the development of the MEPDG, traffic typically was considered based on the concept of the equivalent single-axle load (ESAL). The ESAL concept was developed from the AASHTO road test to establish a damage relationship between the effects of various axle types or amounts of loading and the standard axle load (i.e., 18,000 lb or 8.16 ton single axle with dual tires). The MEPDG, however, handles traffic using a more comprehensive process called *axle load spectra* that analyzes traffic directly via the axle configuration and load magnitude. The axle load spectra approach requires detailed and complete traffic information in order to

characterize traffic properly. The traffic input parameters for this approach include:

- *Initial two-way average annual daily truck traffic (AADTT)*, which is obtained directly from weigh-in-motion (WIM) data or INDOT traffic survey data by multiplying the average annual daily traffic (AADT) by the truck percentage.
- *Percentage of trucks ('percent trucks')* in the design lane and design direction. 'Percent trucks' is the percentage of truck traffic in the designed lane or direction relative to all truck traffic in one direction or both directions.
- *Operational speed*, which is the truck speed that determines the loading frequency underneath the pavement structure; hence, operational speed has a significant impact on the predicted dynamic modulus value(s) of HMA material.
- *Growth of truck traffic*, whereby the MEPDG is able to assign various growth rates to each individual vehicle class; however, those growth rates are constant over time.
- *Axle load distribution*, which is the percentage of the total number of load repetitions within each load group for each axle type. Single, tandem, tridem, and quad axles are considered in the MEPDG, and axle loads are grouped with 1,000-lb (0.45 ton) intervals.
- *Normalized truck volume distribution*, which is the percentage of each truck traffic class. The MEPDG provides nine truck traffic classes according to the FHWA's vehicle classification system.
- *Axle load configuration*, which is the axle spacing in each truck traffic class.
- *Monthly distribution factors*, which distribute the truck traffic within each class throughout the year. These factors were set to be one in the global calibration.
- *Hourly distribution factors*, which distribute the truck traffic within each class throughout one day.
- *Dual tire spacing information*, which can be obtained from WIM data; a default value of 12 inches (30.48 cm) was used in the global calibration.
- *Tire pressure*, which was set to a constant value in this study because individual tire pressure for each truck traffic class is not considered in the MEPDG.
- *Lateral wander of axle load*, which the MEPDG simulates as a normal distribution; standard deviation is used to characterize lateral wander. One distribution is used for all truck traffic classes. The default value of 10 inches (25.4 cm) was used in the global calibration.
- These traffic parameters can be input into three hierarchical input levels:
 - Level 1 requires site-specific traffic data, including traffic count, axle load, and truck traffic class distribution measured at or near the to-be-designed/analyzed roadway segments.
 - Level 2 requires site-specific traffic count and truck traffic class distribution data, whereas axle load data are normally averaged in neighborhood areas or regions.
 - Level 3 is used when only traffic count data are available for the desired roadway segments; global default values are assumed for the other traffic parameters.

4.4.2 Data Collection

The INDOT has characterized Indiana traffic based on the traffic volume and region of the roadways.

Traffic count, truck traffic class distribution, and axle load distribution data were collected for each roadway segment.

APT traffic was simulated using the special axle configuration feature offered by the MEPDG to customize and define the APT wheels assembly. The dual tires were simulated using two tires with each tire load of 4,500 lb (2.04 ton), the dual tire spacing was 13.5 inches (34.29) and the tire inflation pressure was 100 psi (0.69 MPa). Lateral wander standard deviation was set to zero so that the load could be applied repeatedly along the same location.

4.5 Material Characterization

4.5.1 Input Data Requirements

In this study, Level 3 input data were used for the HMA mixtures and unbound materials. Level 1 input requires laboratory characterization of the materials used in the construction of each roadway segment. The required laboratory tests typically are not required for construction. To be consistent with the future implementation of this calibration product, Level 1 input was excluded from the scope of this study.

Table 4.6 and Table 4.7 provide summaries of the data requirements for the three input levels for the HMA mixture volumetric and thermal properties and HMA mixture mechanical properties, respectively.

The unit weight of HMA can be calculated as shown in Equation 4.1.

$$\gamma_{HMA} = \gamma_w \times G_{mb} = \gamma_w \times G_{mm} \times \%G_{mm} \quad (4.1)$$

where:

G_{mb} = bulk specific gravity of the mix;

G_{mm} = theoretical maximum specific density; and

$\%G_{mm}$ = percentage of theoretical maximum specific density.

The calculation of the effective binder content by volume is shown in Equation 4.2.

$$v_{beff} = G_{mb} \left[\frac{P_b}{g_b} - (100 - P_b) \times \frac{(G_{se} - G_{sb})}{G_{se} \times G_{sb}} \right] \quad (4.2)$$

where:

P_b = binder content by weight;

G_b = specific gravity of binder;

TABLE 4.6
Data Requirements for HMA Mixture Volumetric and Thermal Properties

	Unit Weight
Mixture Volumetric	Effective Binder Content by Volume Air Void Content Poisson's Ratio
Thermal	Thermal Conductivity (ASTM E 1952) Heat Capacity (ASTM D 2766) Thermal Contraction

TABLE 4.7
Data Requirements for HMA Mixture Mechanical Properties

Level 1	Dynamic Modulus (AASHTO T 342) <i>or</i> Shear Modulus (AASHTO T 49)	Softening Point (AASHTO T 202) Absolute Viscosity (AASHTO T 201) Kinematic Viscosity (AASHTO T 228)
	Phase Angle (AASHTO T 49)	Specific Gravity Penetration (AASHTO T 53) Brookfield Viscosity (AASHTO T 316)
	Indirect Tensile Strength (AASHTO T 322) Creep Compliance (AASHTO T 322)	
Level 2	Percent Passing 3/4-inch sieve Percent Passing 3/8-inch sieve Percent Passing No. 4 sieve Percent Passing No. 200 sieve <i>or</i> Shear Modulus (AASHTO T 49)	Softening Point (AASHTO T 202) Absolute Viscosity (AASHTO T 201) Kinematic Viscosity (AASHTO T 228)
	Phase Angle (AASHTO T 49)	Specific Gravity Penetration (AASHTO T 53) Brookfield Viscosity (AASHTO T 316)
	Indirect Tensile Strength (AASHTO T 322) Creep Compliance (AASHTO T 322)	
Level 3	Percent Passing 3/4-inch sieve Percent Passing 3/8-inch sieve Percent Passing No. 4 sieve Percent Passing No. 200 sieve Performance Grade or Viscosity Grade or Penetration Grade	

G_{se} = effective specific gravity of mix; and
 G_{sb} = bulk specific gravity of aggregate.
The effective specific gravity of the mix is calculated as Equation 4.3.

$$G_{se} = \frac{100 - P_b}{\frac{100}{G_{mm}} - \frac{P_b}{G_b}} \quad (4.3)$$

The thermal properties are not utilized during rutting analysis; global default values are used.

The dynamic modulus is the most critical parameter that is used to describe HMA. It is a function of temperature and loading frequency. Factors such as aggregate gradation, binder viscosity, binder content, and air void content have a great impact on the dynamic modulus value. The dynamic modulus is measured directly for Level 1 input. For Level 2 and Level 3 inputs, the dynamic modulus is predicted using a revised Witczak model, as shown in Equation 4.4.

$$\begin{aligned} \log E^* = & 3.750063 + 0.02932\rho_{200} - 0.001767(\rho_{200})^2 \\ & - 0.002841\rho_4 - 0.058097v_a - 0.802208\left(\frac{v_{beff}}{v_{beff} + v_a}\right) \\ & + \frac{3.871977 - 0.0021\rho_4 + 0.003958\rho_{38} - 0.000017(\rho_{38})^2 + 0.005470\rho_{34}}{1 + e^{(-0.303313 - 0.313351 \log(f) - 0.3933532 \log(\eta))}} \end{aligned} \quad (4.4)$$

where
 E^* = dynamic modulus, psi;

η = binder viscosity, $10^6 Poise$;
 f = loading frequency, Hz;
 v_a = air void content, %;
 v_{beff} = effective binder content by volume;
 ρ_{34} = cumulative percentage retained on $\frac{3}{4}$ inch sieve;
 ρ_{38} = cumulative percentage retained on 3/8 inch sieve;
 ρ_4 = cumulative percentage retained on No. 4 sieve;
and

ρ_{200} = percentage passing the No. 200 sieve.

Binder viscosity is a critical parameter for dynamic modulus predictions. It is usually expressed as a function of temperature, as shown in Equation 4.5. When the dynamic modulus is provided using Level 1 or Level 2 input, the A and VTS parameters can be estimated using a dynamic shear rheometer test in accordance with AASHTO T 315 (2012) or a series of conventional tests that include viscosity, softening point, and penetration. When the dynamic modulus is provided using Level 3 input, the binder PG, viscosity grade, or penetration grade can be used for estimation.

$$\log \log \eta = A + VTS \log T_R \quad (4.5)$$

where:

η = binder viscosity, cP ;
 T_R = temperature, Rankine; and
 A, VTS = regression parameters.

The indirect tensile strength and creep compliance are measured directly in accordance with AASHTO T 322 (2007) at input Levels 1 and 2. At input Level 3, these parameters are estimated based on the air void content, voids filled with asphalt, asphalt penetration at 77 8F (25 8C), and parameter A.

The required parameters of all the input levels for the unbound subgrade material are the Poisson's ratio, coefficient of lateral earth pressure, and AASHTO soil classification. The material stiffness is defined using the resilient modulus. For Level 2 input analysis, the resilient modulus value is estimated using the California bearing ratio value, R-value, DCP rate, or gradation and Atterberg limit. For Level 3 input analysis, the resilient modulus value is estimated based on the soil classification.

4.5.2 Data Collection

A survey, interviews, and an archived documentation review have been conducted throughout local agencies to acquire the construction information for the roadway segments used in this study. This construction information includes the job mix formulas, pavement structures, construction logs, quality assurance/quality control (QA/QC) data, traffic counts, and pavement condition survey responses. The material properties were prepared for MEPDG inputs as provided in Appendix C. The $\%G_{mm}$ was assumed to be 92 percent because the original QC information was not available and 92 percent $\%G_{mm}$ is the target compaction level across all Indiana projects. As presented in Appendix C, the resilient modulus values were calculated using the DCP or LWD test results for the APT sections. For the other roadway segments, the resilient modulus values were not specified and were estimated based on the subgrade treatment type. The definitions of subgrade treatment type are as follows:

- Type IA consists of 12 inches of the subgrade excavated and replaced with coarse aggregate No. 53.
- Type IV consists of 12 inches of the subgrade excavated and replaced with coarse aggregate No. 53 on Type IB Geogrid.
- Type IB consists of 14 inches of chemical soil modification.

Coarse aggregate No. 53 is the most commonly used crushed aggregate in Indiana; detailed information can be found in the *Indiana Department of Transportation Standard Specifications*, Section 904.03 (INDOT, 2014).

4.6 Distress Survey

Rutting data for the test roadway segments were acquired from the INDOT PMS, which contains pavement transverse profiles and rut depth values at one-foot intervals. The rut depth is reported for the driving lane in each direction; measurements are taken from both the left wheel path and right wheel path. The most recent rut depth measurements (2014) were collected

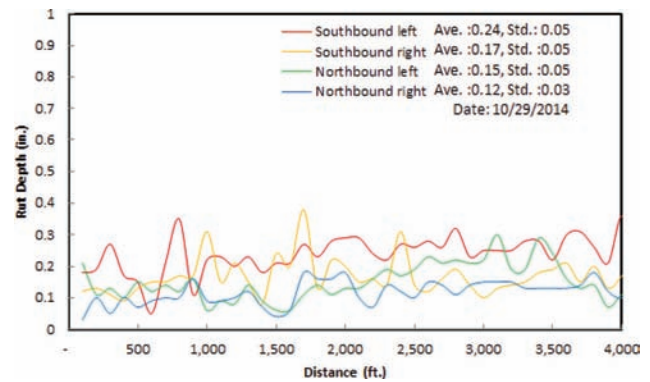


Figure 4.2 Rut depth measurements from SR-43-25550.

from the PMS. Figure 4.2 shows the rutting data from SR-43 (contract 25550). The standard deviation of the measurements is around 0.05 inch (0.127 cm), and the average of the collected data is used in the calibration process. The rest of these data can be found in Appendix D.

4.7 Conditions Simulation

Once asphalt concrete is placed and exposed to the environment, it begins to age as the material starts to oxidize. As a result, the viscous properties of the asphalt binder change over time and, thus, so do the HMA mixtures. HMA mixtures tend to become more stiff and brittle with time. Such an impact plays a vital role in material behavior and pavement long-term performance. The MEPDG incorporates the effects of aging using the GAS developed by Mirza and Witzak (1995). The system consists of four models: the original to mix/lay-down model, the surface aging model, air void adjustment, and the viscosity-depth model.

The GAS predicts the binder viscosity at any time and at any depth in the pavement system. The predicted viscosity is then incorporated into the determination of the dynamic modulus. A realistic aging effect is then simulated. However, such a feature challenges the most faithful simulation of an APT. APTs usually are performed within a few months of pavement placement whereas MEPDG simulations normally are conducted over a much longer analysis period to evaluate the rutting evolution. As a result, more asphalt aging is simulated in the MEPDG than actually occurs during APTs. Also, the MEPDG does not allow users to turn off the GAS manually. The minimum analysis period in the MEPDG is one year, which means that a minimum of one year of aging must be enforced. Figure 4.3 shows a preliminary MEPDG analysis run using APT parameters; the evolution of the modulus of each sublayer is plotted. During the one-year analysis period, about a 50 percent increase in the modulus value occurred in the first sublayer.

The FWD test was used to quantify the amount of increase in the modulus value. Then, the analysis period (referred to as the “aging analysis period”) in accordance with the amount of increase could be determined

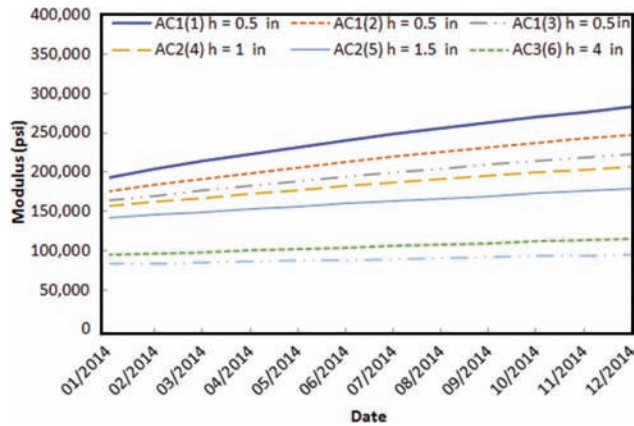


Figure 4.3 MEPDG simulated aging effect for APT Lane 4.

for each test lane. The aging analysis period is used in the calibration process if the aging analysis period is less than one year, which is the minimum analysis period allowed in the MEPDG. APT load applications were stretched within the aging analysis period, and only the simulation results within the aging analysis period were used. As an example, the *in situ* modulus value of APT Lane 1 was found to increase by 27 percent. Specifically, Figure 4.3 indicates that an average modulus value increase of 27 percent occurred within six months; i.e., the aging analysis period is six months. The total APT load application is 50,000 passes, which must be applied during the six-month period. Thus, 8,333 passes per month were used in the MEPDG one-year simulation. In short, six-month analysis results were used although one-year simulation was performed.

5. MEPDG CALIBRATION

5.1 Introduction

This chapter presents the MEPDG local calibration for Indiana full-depth flexible pavements. It should be noted that local calibration is a process of adjusting the calibration coefficients in order to eliminate or minimize bias and standard errors of estimates. The supporting models that are employed by the transfer functions, such as the EICM, GAS, HMA dynamic modulus prediction model, and others, are out of the scope of this study and are assumed to be representative of real-world conditions. The objective term used for the optimization process is the SSE between the predicted and actual rut depths instead of bias. Note that the MEPDG allows a maximum of three asphalt concrete layer analyses. However, because Indiana pavements normally have five layers, it was decided to combine the bottom three layers (i.e., the upper base layer, OG layer, and bottom base layer) as one uniform base layer in the MEPDG simulation. Recall that rutting that occurs in asphalt concrete and unbound material layers is predicted using two separate rutting transfer functions. The transfer function of asphalt

concrete layers, as shown in Equation 5.1, has three calibration coefficients (i.e., β_{r1} , β_{r2} , and β_{r3}), whereas the transfer function for unbound materials, as shown in Equation 5.2, has only one calibration coefficient (i.e., β_{s1}).

$$\frac{\varepsilon_p}{\varepsilon_r} = K_Z \beta_{r1} 10^{k_{r1}} (T)^{k_{r2} \beta_{r2}} (N)^{k_{r3} \hat{a}_{r3}} \quad (5.1)$$

$$\delta_a(N) = \beta_{s1} k_1 \varepsilon_v h \left(\frac{\varepsilon_0}{\varepsilon_r} \right) e^{-\left(\frac{N}{N_0} \right)^\beta} \quad (5.2)$$

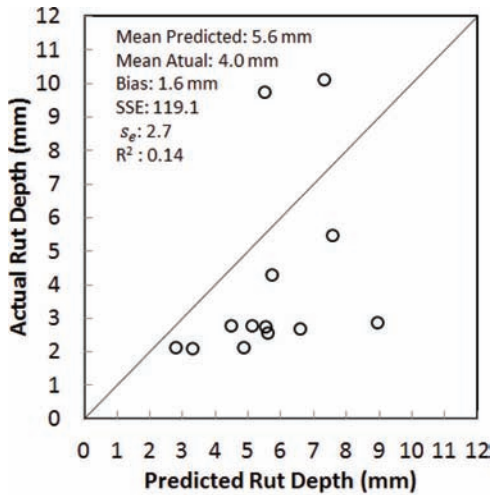
Previous calibration efforts were conducted under the assumption that the amount of rutting that occurs in asphalt concrete layers and unbound material layers is the same as that predicted by the MEPDG, because only total rut depth measurements were available. In other words, the two transfer functions were calibrated simultaneously. In this study, according to the APT findings, around 11 percent of the total rut depth was found in subgrade for typical Indiana full-depth flexible pavements, regardless of pavement thickness and paving material.

5.2 Evaluation of Local Bias from Global Calibrated Model

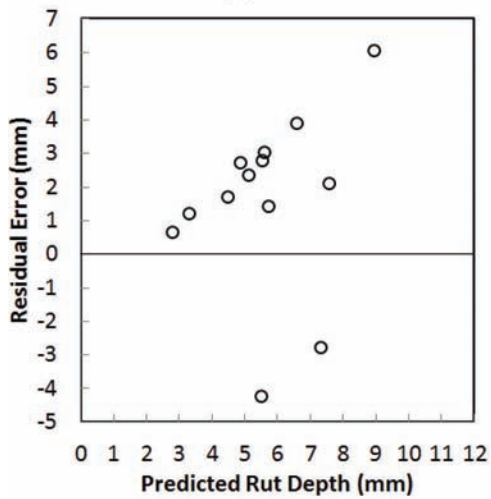
Before proceeding to the calibration process, it was necessary to evaluate the accuracy of the global calibrated model for local practice. The MEPDG with its default model was executed to analyze the preselected roadway segments and APT sections. Figures 5.1, 5.2, and 5.3 present comparisons between the predicted and actual rut depths in the global model for the total rut depths, asphalt concrete layer rut depths, and subgrade rut depths, respectively.

Extensive dispersion and poor correlation are evident between the predicted and actual values for total rut depth. The rut depth was overpredicted by 1.6 mm (0.063 inch). This trend was due mostly to the overestimation of the subgrade rutting (i.e., bias is 3.3 mm or 0.130 inch). For the asphalt concrete layer rutting, on the other hand, the predicted values are relatively close to the actual rut depths with a fair correlation (i.e., R^2 is 0.38), and the predicted values are lower than the actual values with an average of 1.7 mm (0.067 inch).

Statistical analyses were performed to evaluate the predictions. The null hypothesis is that no significant difference exists between the predictions and actual values. Table 5.1 presents a summary of the statistical parameters at the 95 percent confidence level for the globally calibrated models. The null hypothesis for both the asphalt concrete layer and subgrade was rejected, indicating that there is a significant difference between the predictions and actual values. Although the null hypothesis for the total rut depth was accepted, the p-value is very close to the critical value of 0.05, indicating an inconclusive conclusion.



(a)

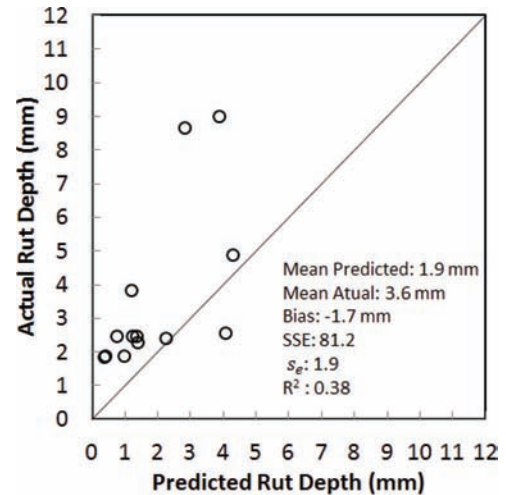


(b)

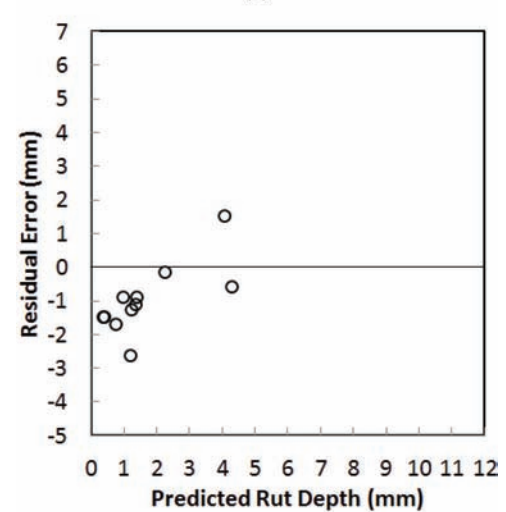
Figure 5.1 (a) Predicted rut depths, and (b) prediction residual errors of total rut depth for global model.

5.3 Elimination of Local Bias and Dispersion

Calibration is an optimization process that searches for the best combination of the four calibration coefficients (i.e., $\beta_{r1}, \beta_{r2}, \beta_{r3}$, and β_{s1}) to yield the lowest bias or SSE between actual and predicted rut depths. Among the four calibration coefficients, β_{r1} and β_{s1} are direct multipliers; in other words, they are linearly proportional to the predictions. Therefore, these two coefficients can be optimized externally using a GRG algorithm to reduce the SSE. The other two coefficients, β_{r2} and β_{r3} , on the other hand, are the power terms in the transfer functions shown in Equation 5.1 and Equation 5.2. They adjust the nonlinear effect of temperature and the number of traffic repetitions for the predictions, so that these two coefficients have to be fine-tuned by executing the MEPDG using every possible combination to determine the one that results in the lowest SSE.



(a)



(b)

Figure 5.2 (a) Predicted rut depths, and (b) prediction residual errors of asphalt concrete layer rut depth for global model.

Figure 5.4 presents the calibration procedure. The measured total rut depth was first distributed into the asphalt concrete layer and subgrade. Then, β_{s1} was optimized externally to minimize the SSE between the predicted and measured subgrade rut depths. For the asphalt concrete layer, β_{r1}, β_{r2} , and β_{r3} must be optimized simultaneously. A large factorial of every possible combination of β_{r2} and β_{r3} , as shown in Table 5.2, was determined based on previous research findings and experience gained from running the optimizations.

The MEPDG was executed for 13 sections for each combination. The predicted rut depths of the asphalt concrete layer and subgrade were exported and prepared for external optimization. β_{r1} was then optimized for each combination of β_{r2} and β_{r3} . Figure 5.5 presents the resultant SSEs between the predicted and measured asphalt concrete layer rut depths in a 3-D surface plot.

It was found that the combination of $\beta_{r2} = 1.9$ and $\beta_{r3} = 0.4$ yielded the lowest SSEs. Table 5.3 provides a summary of the selected calibration coefficients.

Figures 5.6, 5.7, and 5.8 present comparisons of the predicted rut depths and prediction residual errors between the global and local models. The notable bias that was evident in the global model for the rut depths in the asphalt concrete layer and subgrade was corrected in the local model. Precision also improved from

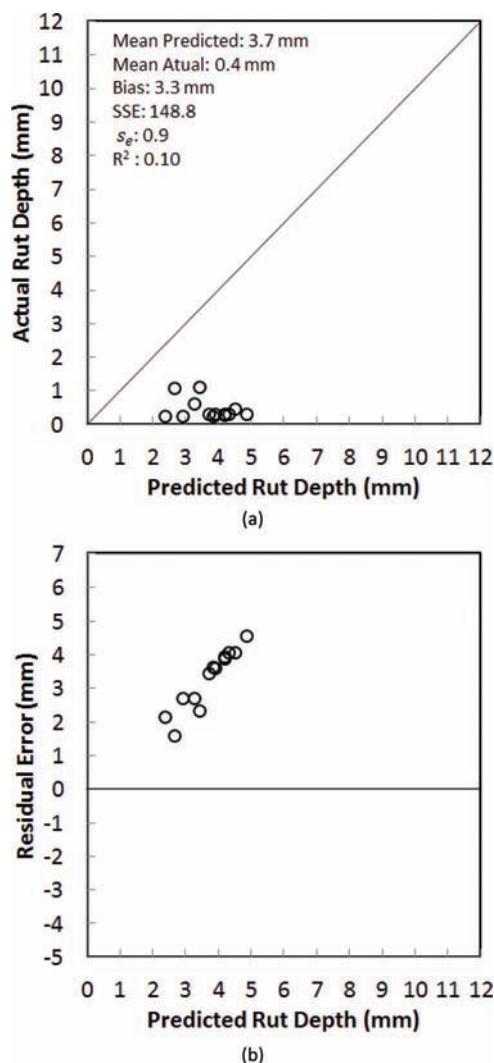


Figure 5.3 (a) Predicted rut depths, and (b) prediction residual errors of subgrade rut depth for global model.

TABLE 5.1
Summary of Statistical Parameters

Layer	Mean Predicted (mm)	Mean Actual (mm)	Bias (mm)	SSE (mm ²)	S _e (mm)	R ²	Hypothesis, H ₀ :
AC Layer	1.93	3.59	-1.66	81.28	1.9	0.38	Rejected, p = 0.048
SG	3.72	0.44	3.27	148.83	0.9	0.10	Rejected, p = 0.000
Total	5.65	4.03	1.62	119.10	2.8	0.14	Accepted, p = 0.088

the calibration; the residual errors are less scattered, especially for the subgrade, and they are evenly distributed around the zero line, indicating unbiased or low bias predictions.

Table 5.4 provides comparisons of the statistical parameters between the global and local models.

The accuracy of the MEPDG prediction models has been improved in every aspect. Prior to the calibration effort, the statistical test results showed that significant differences existed between the predictions and measured values for the asphalt concrete layer and subgrade rut depths, with an almost insignificant difference for the total rut depth. After calibration, all of the hypotheses were accepted, with a clear tendency toward significance at the 95 percent confidence level. The coefficients of correlation improved overall to above 0.7 except for the subgrade rut depths. The precision of prediction also increased, as indicated by the reduction by 42 percent in the standard error of estimates. The bias of the predictions also was reduced, as indicated by the reduction by 85 percent of the SSEs.

5.4 Model Validation

In order to demonstrate that the calibrated models could provide accurate and statistically sound pavement performance predictions, validation was conducted using jackknife resampling techniques. As shown in Figure 5.4, the validation process started with removing one section from the available 13 sections. Next, the MEPDG was calibrated using the remaining 12 sections, and the calibrated model was then validated using the removed section. This withholding, calibrating, and validating process was repeated 13 times. All the sections were used for validation, and the validation statistics were obtained. Because the validation was conducted using sections that were not used in calibrating the models, the validation statistics are considered as independent evaluations of the models' prediction performance. Figures 5.9, 5.10, and 5.11 present comparisons between the calibration and validation results.

Figures 5.9, 5.10, and 5.11 show a similar trend between the calibration and validation results in terms of bias and precision.

Table 5.5 compares the statistics obtained from the global model, calibrated model, and model validation. The validation statistics are similar overall to those of the

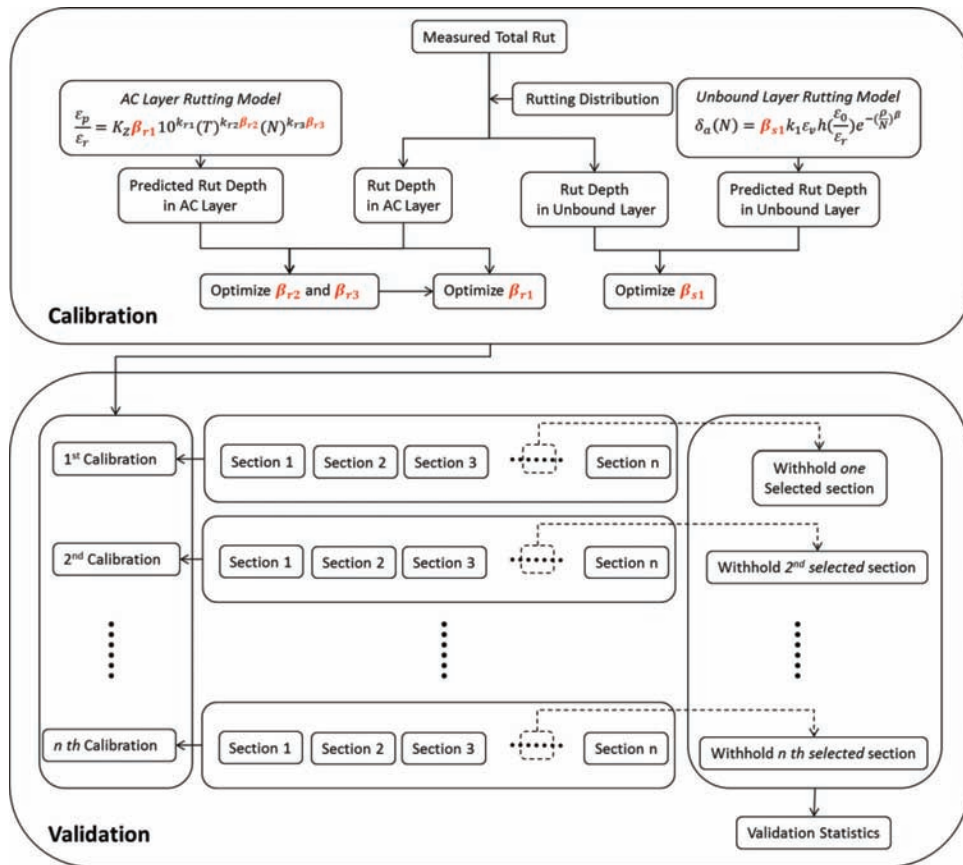


Figure 5.4 Calibration and validation flowchart.

TABLE 5.2
Combinations of β_{r2} and β_{r3}

No.	β_{r2}	β_{r3}	No.	β_{r2}	β_{r3}
1	1.7	0.1	11	1.9	0.1
2	1.7	0.2	12	1.9	0.2
3	1.7	0.3	13	1.9	0.3
4	1.7	0.4	14	1.9	0.4
5	1.7	0.5	15	1.9	0.5
6	1.8	0.1	16	2.0	0.1
7	1.8	0.2	17	2.0	0.2
8	1.8	0.3	18	2.0	0.3
9	1.8	0.4	19	2.0	0.4
10	1.8	0.5	20	2.0	0.5

calibrated models. Although the SSE values obtained from validation are relatively higher than those obtained from the calibrated models, they are still lower than those obtained from the original local models. The coefficients of correlation remained at the same

level for validation. The same hypotheses also were accepted for the asphalt concrete layer, subgrade, and total rut depth at the 95 percent confidence level, with p-values similar to those obtained from the calibrated models.

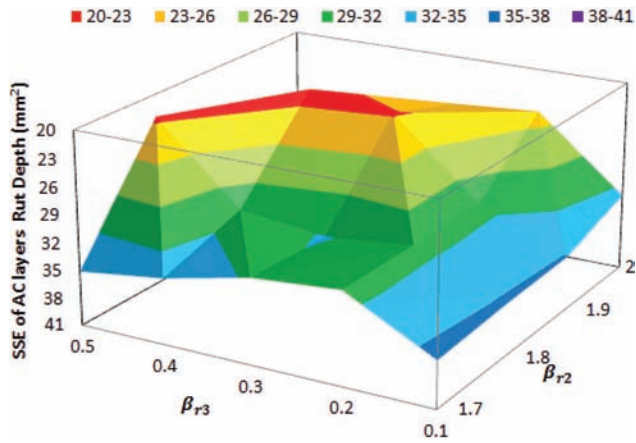


Figure 5.5 SSEs between predicted and measured asphalt concrete layer rut depths.

TABLE 5.3
Selected Calibration Coefficients

β_{r1}	β_{r2}	β_{r3}	β_{s1}
0.079	1.9	0.4	0.110

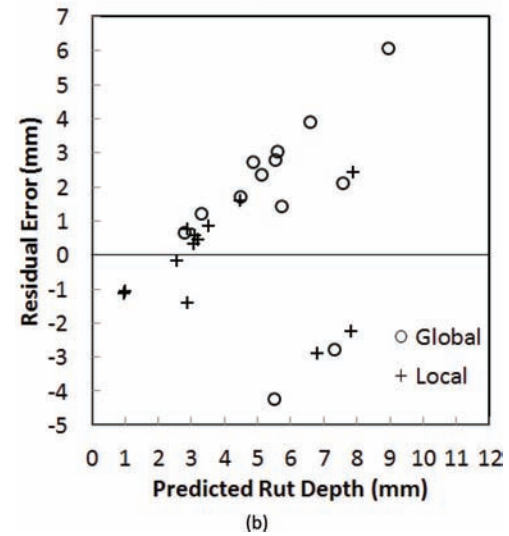
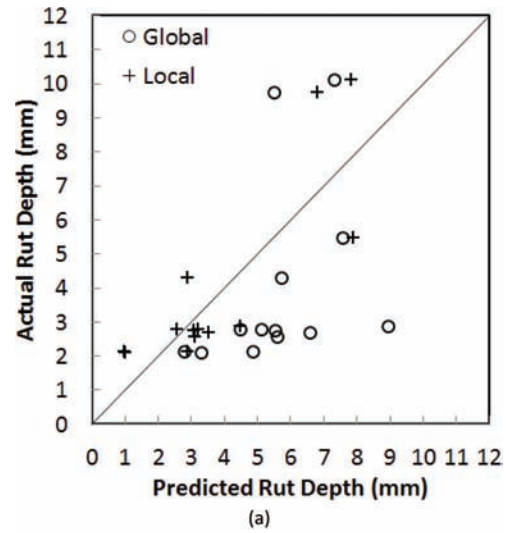
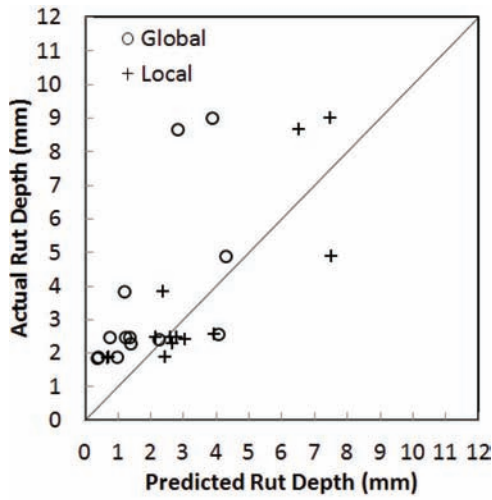
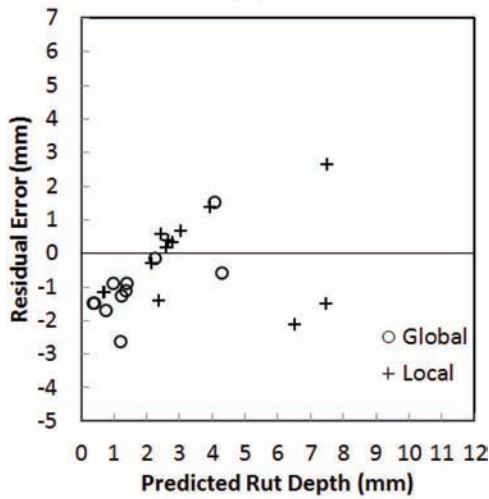


Figure 5.6 (a) Predicted rut depths, and (b) prediction residual errors of total rut depth for global and local models.

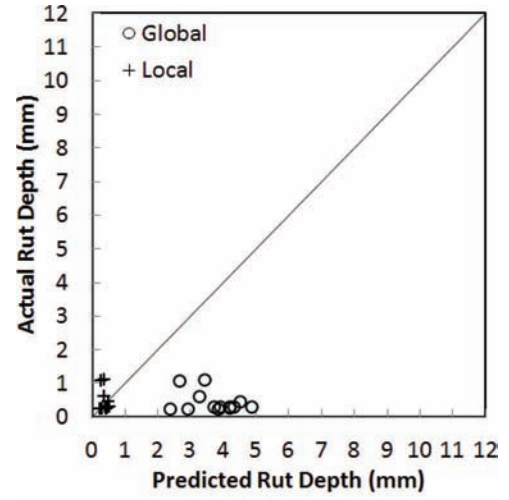


(a)

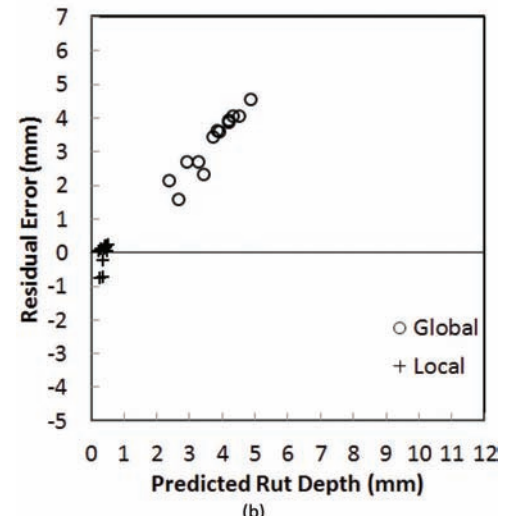


(b)

Figure 5.7 (a) Predicted rut depths, and (b) prediction residual errors of asphalt concrete layer rut depth for global and local models.



(a)



(b)

Figure 5.8 (a) Predicted rut depths, and (b) prediction residual errors of subgrade rut depth for global and local models.

TABLE 5.4
Statistics for Global and Local Models

Layer	Model	Mean Predicted (mm)	Mean Actual (mm)	Bias (mm)	SSE (mm ²)	S _e (mm)	R ²	Hypothesis, H ₀ :
AC Layer	Global	1.93	3.59	-1.66	81.3	1.9	0.38	Rejected, p = 0.048
	Local	3.46	3.59	-0.12	21.6	1.3	0.71	Accepted, p = 0.896
SG	Global	3.72	0.44	3.27	148.8	0.9	0.10	Rejected, p = 0.000
	Local	0.41	0.44	-0.03	1.4	0.3	0.10	Accepted, p = 0.709
Total	Global	5.65	4.03	1.62	119.1	2.7	0.14	Accepted, p = 0.088
	Local	3.87	4.03	-0.16	28.2	1.5	0.70	Accepted, p = 0.876

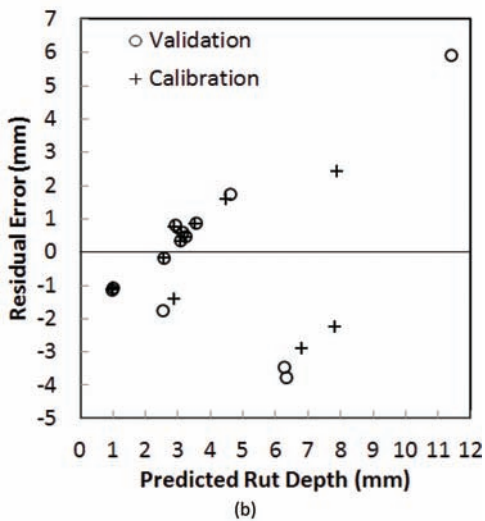
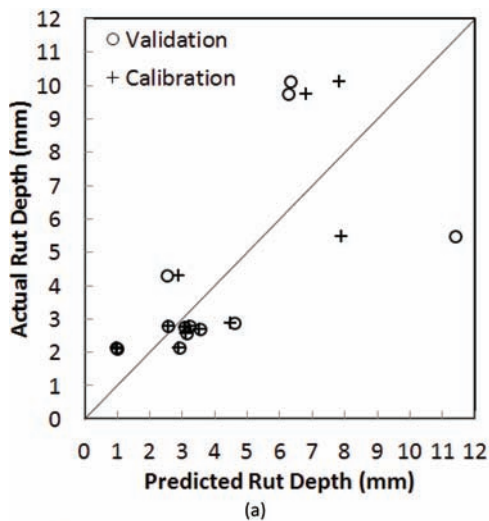


Figure 5.9 (a) Predicted rut depths, and (b) prediction residual errors of total rut depth for calibration and validation.

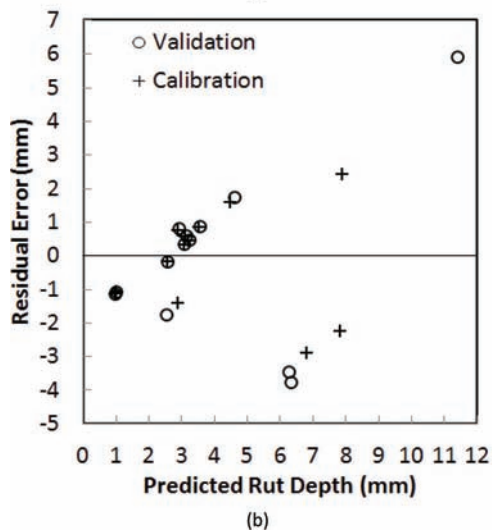
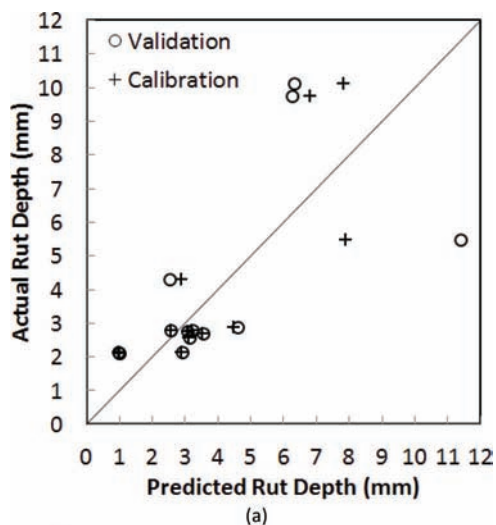


Figure 5.10 (a) Predicted rut depths, and (b) prediction residual errors of asphalt concrete layer rut depth for calibration and validation.

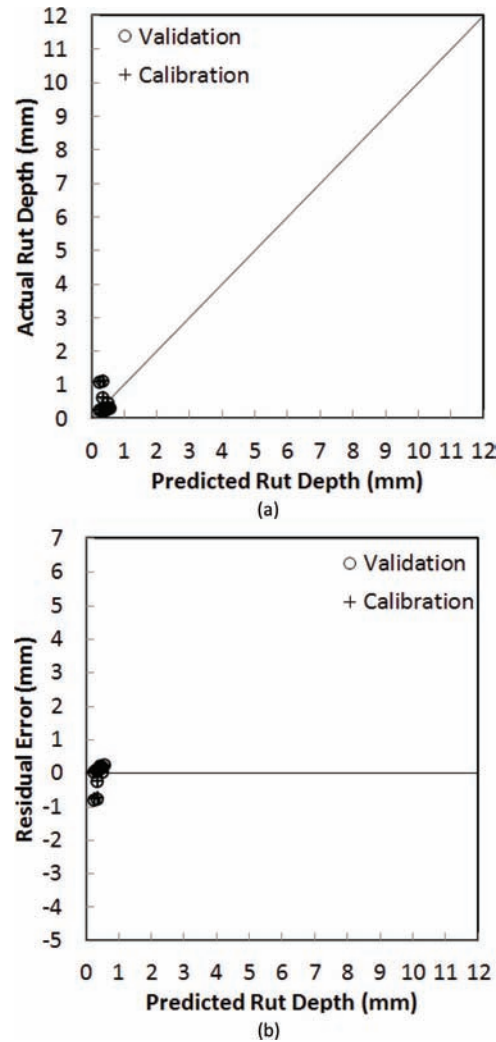


Figure 5.11 (a) Predicted rut depths, and (b) prediction residual errors of subgrade rut depth for calibration and validation.

TABLE 5.5
Statistics for Global and Local Models and Validation

Layer	Model	Mean Predicted	Mean Actual	Bias (mm)	SSE (mm ²)	S _e (mm)	R ²	Hypothesis, H0:
		(mm)	(mm)					
AC Layer	Global	1.93	3.59	-1.66	81.30	1.90	0.38	Rejected, p = 0.048
	Local	3.46		-0.12	21.60	1.30	0.71	Accepted, p = 0.896
	Validation	3.57		-0.02	63.27	2.30	0.71	Accepted, p = 0.984
SG	Global	3.72	0.44	3.27	148.80	0.90	0.10	Rejected, p = 0.000
	Local	0.41		-0.03	1.40	0.30	0.10	Accepted, p = 0.709
	Validation	0.41		-0.03	1.59	0.36	0.23	Accepted, p = 0.737
Total	Global	5.65	4.03	1.62	119.10	2.70	0.14	Accepted, p = 0.088
	Local	3.87		-0.16	28.20	1.50	0.70	Accepted, p = 0.876
	Validation	3.98		-0.05	71.77	2.44	0.70	Accepted, p = 0.963

6. CONCLUSIONS AND RECOMMENDATIONS

6.1 Summary

This study investigated the fundamentals of rutting behavior for full-depth flexible pavements. A mid-depth rut monitoring and automated laser profile system was designed to reconstruct the transverse profiles at each pavement layer interface. The rutting distributions throughout the pavement layers were monitored closely during APT loading. The findings were then employed to improve the rutting model that is embedded in the MEPDG.

A procedure was developed to provide the most faithful simulations of the APT conditions that include climate, traffic, and aging conditions using virtual weather station generation, a special traffic configuration, and FWD evaluation. A guideline was developed to calibrate the MEPDG prediction models using a database that contains both APT sections and field roadway segments and accounts for the rutting in individual pavement layers. The APT sections served to supplement the field roadways used in the calibration process to overcome issues such as small sample size and low distress levels of field roadways.

6.2 Conclusions

The following conclusions were drawn from this study:

- The developed mid-depth rut monitoring and automated laser profile system successfully captured the evolution of permanent deformation for each pavement structural layer.
- The prediction performance of the MEPDG rutting transfer functions was improved significantly using APTs.
- For full-depth flexible pavements constructed using the same type of mixture, the total rut depth measured at the pavement surface remained the same when the asphalt concrete layer thickness was increased from 12.5 inches (31.75 cm) to 15.5 inches (39.37 cm). This finding agrees with practice experience that permanent deformation within asphalt concrete does not increase with increasing pavement thickness once the pavement is sufficiently thick.
- Most pavement rutting was caused by the deformation of the asphalt concrete. The primary portion of rutting occurred at the upper part of the asphalt concrete layer, with about half of the rutting observed within the top four inches of the pavement layer.
- As a surface course, SMA has much greater rutting resistance than a regular dense-graded mix; in this study, replacing 1.5 inches (3.81 cm) of a regular dense-graded surface course with SMA mixture reduced the amount of rutting in the SMA surface course by around 75 percent and reduced the total rut depth measured at the pavement surface by 46.2 percent. The critical rutting location also migrated from the surface layer to the intermediate layer and upper base layer.
- For full-depth flexible pavements, regardless of the pavement thickness and paving material, the subgrade deformation remained at a very low level; only about 10 percent of rutting occurred in the subgrade.

- APT conditions were simulated successfully using the MEPDG following the developed procedures through virtual weather station generation, a special traffic configuration, and FWD evaluation.
- For the globally calibrated MEPDG models, the predicted asphalt concrete layer and subgrade rut depths were found to be significantly different from the actual measurements at the 95 percent confidence level. The total rut depth was overpredicted by 1.6 mm (0.063 inch). This trend was due mostly to the overestimation of the subgrade rutting (i.e., bias was 3.3 mm or 0.130 inch). However, the predicted asphalt concrete layer rutting depth values were lower than the actual values with an average of 1.7 mm (0.067 inch).
- The MEPDG was calibrated successfully for Indiana full-depth flexible pavements constructed with Superpave designed mixtures using a database generated from both APT sections and field roadways.
- The accuracy of the MEPDG prediction models was improved after the calibration process. The residual errors were less scattered, especially for the subgrade, and they were distributed evenly around the zero line, thus indicating unbiased or low bias predictions; the SSE was reduced by 85 percent. The standard error of estimates was reduced by 42 percent, indicating that the precision of the predictions was improved. No significant difference was found between the predicted and actual total rut depths and between the asphalt concrete layer and subgrade rut depths at the 95 percent confidence level.
- The model validation confirmed that the calibrated models are able to provide accurate and statistically sound pavement performance predictions. Jackknife resampling techniques were used in the validation process. A similar trend was observed between the calibration and validation in terms of bias and precision. The validation statistics are similar overall to the statistics of the calibrated models. No significant difference was found between the predicted and actual total rut depths and between the asphalt concrete layer and subgrade rut depths at the 95 percent confidence level.

6.3 Recommendations

The work completed in this study examined the rutting behavior of full depth flexible pavement and improved the MEPDG predictions. Several recommendations are provided for future research and MEPDG implementation:

- Only two types of surface course material, i.e., a regular dense-graded mixture and SMA mixture, were tested in this study. Future research should expand the material database and cover new materials such as warm mix asphalt, recycled asphalt pavement, and polymer-modified asphalt.
- Future research should be conducted for other pavement types such as asphalt overlays. When constructing asphalt overlays, the deteriorated surface commonly is milled to a certain depth; the new surface is then placed over the milled surface. Without knowing the rutting distribution in the existing pavement, the amount of rutting that already has occurred within the remaining layers of the existing pavement will be hidden, hence increasing the difficulty of designing the new surface layer.

Thus, the findings of this study would be valuable for the analysis and design of asphalt overlays.

- Given that only 13 sections were used during the calibration and validation processes in this study, further model validation might be necessary once additional full-depth asphalt concrete field roadways become available.
- Future research should expand the APT sections with additional pavement structures and subgrade types to develop a more comprehensive relationship between the rutting distribution and the paving material, pavement thickness, and subgrade.
- Forensic studies should be conducted for field roadways to confirm the findings from this APT study.
- Based on the experience gained from this study, it is highly recommended for future MEPDG implementation that extra care should be taken regarding the rutting distribution. This study found that the globally calibrated rutting model significantly overpredicts the amount of rutting that occurs in the subgrade, especially for full-depth pavement.
- It is also recommended that any pavement condition evaluation should be performed with extra caution, because most of the precision problems in this study seemed to come from the distress measurements.
- Finally, the author would like to emphasize the importance of a PMS that contains a complete and comprehensive roadway inventory and high quality data. A carefully designed and maintained PMS not only preserves the road network but also provides valuable information for the study, design, and analysis of future pavements.

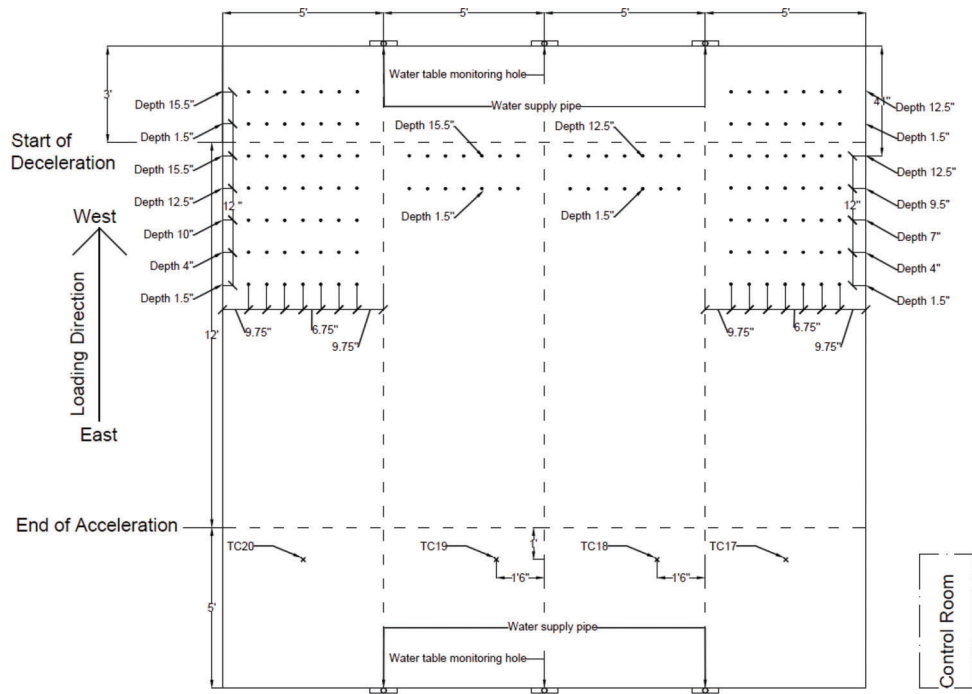
REFERENCES

- AASHTO. (1993). *AASHTO guide for design of pavement structures*. Washington, DC: American Association of State Highway and Transportation Officials.
- AASHTO. (2008). *Mechanistic-empirical pavement design guide: A manual of practice*. Washington, DC: American Association of State Highway and Transportation Officials.
- AASHTO. (2010). *Guide for the local calibration of the mechanistic-empirical pavement design guide*. Washington, DC: American Association of State Highway and Transportation Officials.
- AASHTO R 48. (2013). *Standard practice for determining rut depth in pavements*. Washington, DC: American Association of State Highway and Transportation Officials.
- AASHTO T 315. (2012). *Method of test for determining the rheological properties of asphalt binder using a dynamic shear rheometer (DSR)*. Washington, DC: American Association of State Highway and Transportation Officials.
- AASHTO T 322. (2007). *Standard method of test for determining the creep compliance and strength of hot mix asphalt (HMA) using the indirect tensile test device*. Washington, DC: American Association of State Highway and Transportation Officials.
- Alavi, S., Tavares, M. P., & LeCates, J. F. (2008). *Falling weight deflectometer usage* (NCHRP Synthesis 381). Washington, DC: Transportation Research Board.
- Al-Qadi, I. M., Loulizi, A., Elseifi, M., & Lahouar, S. (2004). The Virginia smart road: The impact of pavement instrumentation on understanding pavement performance. *Journal of the Association of Asphalt Paving Technologists, AAPT*, 427–465.
- Applied Research Associates, Inc. (2004). *Guide for mechanistic-empirical design of new and rehabilitated pavement structures* (NCHRP Project 1-37A). Washington, DC: Transportation Research Board.
- ASTM D 4694-09. (2015). *Standard test method for deflections with a falling-weight-type impulse load device*. West Conshohocken, PA: ASTM International.
- ASTM D 6951. (2015). *Standard test method for use of the dynamic cone penetrometer in shallow pavement applications*. West Conshohocken, PA: ASTM International.
- ASTM E 2583. (2015). *Standard test method for measuring deflections with a light weight deflectometer (LWD)*. West Conshohocken, PA: ASTM International.
- Ayres, M. J. (1997). *Development of a rational probabilistic approach for flexible pavement analysis* (Doctoral dissertation). College Park, MD: University of Maryland at College Park.
- Azari, H., Mohseni, A., & Gibson, N. (2008). Verification of rutting predictions from Mechanistic Empirical Pavement Design Guide using accelerated loading facility data. *Transportation Research Record*, 2057, 157–167. <https://doi.org/10.3141/2057-19>
- Bonaquist, R. J., & Mogawer, W. S. (1997). Analysis of pavement rutting data from FHWA pavement testing facility superpave validation study. *Transportation Research Record*, 1590, 80–88. <https://doi.org/10.3141/1590-10>
- Brown, E. R., & Cross, S. A. (1989). A study of in place rutting of asphalt pavements. *Journal of the Association of Asphalt Paving Technologists*, 58, 1–39.
- Brown, E. R., & Cross, S. A. (1992). *A national study of rutting in hot mix asphalt (HMA) pavements* (NCAT Report 92-05). Auburn, AL: National Center for Asphalt Technology, Auburn University.
- Ceylan, H., Kim, S., Gopalakrishnan, K., & Ma, D. (2013). *Iowa calibration of MEPDG performance prediction models* (InTrans Project 11-401). Ames, IA: Institute for Transportation, Iowa State University.
- Choubane, B., Greene, J., & Sheppard, K. (2011). *Instrumentation of Florida's accelerated pavement testing facility*. Tallahassee, FL: The Florida Department of Transportation.
- Dempsey, B. J., Herlach, W. A., & Patel, A. J. (1985). *The climatic-material-structural pavement analysis program* (Publication No. FHWA/RD-84-115; Vol. 3). Washington, DC: Federal Highway Administration.
- De Beer, M., Groenendijk, J., & Fischer, C. (1996). *Three dimensional contact stresses under the LINTRACK wide base single tyres, measured with the Vehicle-Road Surface Pressure Transducer Array (VRSPTA) system in South Africa*.
- El-Basyouny, M., Witzak, M., & Kaloush, K. (2005). Development of the permanent deformation models for the 2002 design guide. In *TRB 84th Annual Meeting compendium of papers* [CD-ROM]. Washington, DC: Transportation Research Board.
- Elkins, G. E., Thompson, T., Simpson, A., & Ostrom, B. (2012). *Long-term pavement performance information management system: Pavement performance database user reference guide* (Publication No. FHWA-RD-03-088). McLean, VA: Federal Highway Administration.
- Gautreau, G., Zhang, Z., & Wu, Z. (2008). *Accelerated loading evaluation of subbase layers in pavement performance* (Publication No. FHWA/LA.09/468). Baton Rouge, LA: Louisiana Transportation Research Center.
- Gibson, N., Li, S., & Kutay, M. (2010). Rutting resistance of laboratory-prepared and field-compacted asphalt mixtures. *Transportation Research Record*, 2181, 109–116. <https://doi.org/10.3141/2181-12>

- Gibson, N., Qi, X., Shenoy, A., Al-Khateeb, G., Kutay, M. E., Andriescu, A., Harman, T. (2008). *Performance testing for superpave and structural validation* (Publication No. FHWA-HRT-11-045). McLean, VA: Federal Highway Administration.
- Guymon, G. L., Berg, R. L., & Johnson, T. C. (1986). *Mathematical model of frost heave and thaw settlement in pavement* (CRREL Report 93-2). Hanover, NH: U.S. Army Corps of Engineers, Cold Region Research and Engineering Laboratory.
- Hall, K. D., Xiao, D. X., & Wang, K. C. (2011). Calibration of the Mechanistic-Empirical Pavement Design Guide for flexible pavement design in Arkansas. *Transportation Research Record*, 2226, 135–141. <https://doi.org/10.3141/2226-15>
- Harvey, J., & Popescu, L. (2007). Accelerated pavement testing of rutting performance of two caltrans overlay strategies. *Transportation Research Record*, 1716, 116–125. <https://doi.org/10.3141/1716-14>
- Hofstra, A., & Klomp, A. (1972). *Permanent deformation of flexible pavement under simulated road traffic conditions*. Paper presented at the Third International Conference on the Structural Design of Asphalt Pavements, September 11–15, Longon, England.
- Hong, F., & Chen, D.-H. (2008). Calibrating Mechanistic-Empirical Design Guide permanent deformation models based on accelerated pavement testing. *Journal of Testing and Evaluation*, 37(1), 31–39. <https://doi.org/10.1520/JTE101854>
- Hua, J. (2000). *Finite element modeling and analysis of accelerated pavement testing devices and rutting phenomenon* (Doctoral dissertation). West Lafayette, IN: Purdue University.
- Immanuel, S., & Timm, D. (2007). A field-calibrated shear strain rut prediction model. In *TRB 86th Annual Meeting compendium of papers* [CD-ROM]. Washington, DC: Transportation Research Board.
- INDOT. (2014). Course aggregates. Section 904.03 in *2014 Standard specifications*. Indianapolis, IN: Indiana Department of Transportation.
- Jones, D., Harvey, J., Mateos, A., & Al-Qadi, I. (2012). Simulating the effects of instrumentation on measured pavement response. In D. Jones, J. Harvey, A. Mateos, & I. Al-Qadi (Eds.), *Advances in pavement design through full-scale accelerated pavement testing: Proceedings of the 4th International Conference on Accelerated Pavement Testing* (pp. 153–161). Boca Raton, FL: CRC Press.
- Kaloush, K. E., & Witczak, M. W. (2000). *Development of a permanent to elastic strain ratio model for asphalt mixtures* (NCHRP Project 1-37A). Washington, DC: Transportation Research Board.
- Kerkhoven, R. E., & Dormon, G. M. (1953). *Some considerations on the California bearing ratio method for the design of flexible pavements* (Shell Bitumen Monograph, No. 1, 3rd Release). London, UK: Shell International Company.
- Kim, N. (2004). Evaluation of rutting performance of asphalt concrete layers using multi-depth deflectometers (MDD). *KSCJ Journal of Civil Engineering*, 8(4), 411–416. <https://doi.org/10.1007/BF02829165>
- Kim, Y. R., Jadoun, F. M., Hou, T., & Muthadi, N. (2011). *Local calibration of the MEPDG for flexible pavement design* (Research Project No. HWY-2007-07). Raleigh, NC: North Carolina State University.
- Leahy, R. B. (1989). *Permanent deformation characteristics of asphalt concrete* (Doctoral dissertation). College Park, MD: University of Maryland at College Park.
- Levenberg, E., McDaniel, R. S., & Olek, J. (2009). *Validation of NCAT structural test track experiment using INDOT APT facility* (Joint Transportation Research Program Publication No. FHWA/IN/JTRP-2008/26). West Lafayette, IN: Purdue University. <https://doi.org/10.5703/1288284314311>
- Li, Q., Lee, H., & Lee, S. (2011). Development and calibration of a permanent deformation model based on shear properties of asphalt mixtures. In *TRB 90th Annual Meeting compendium of papers* [CD-ROM]. Washington, DC: Transportation Research Board.
- Lytton, R. L., Pufahl, D. E., Michalak, C. H., Liang, H. S., & Dempsey, B. J. (1990). *An integrated model of the climatic effects on pavement* (Publication No. FHWA-RD-90-033). McLean, VA: Federal Highway Administration.
- Mbakisya, A., & Romanoschi, S. (2010). Verification of mechanistic prediction models for permanent deformation in asphalt mixes using accelerated pavement testing. In *TRB 89th Annual Meeting compendium of papers* [CD-ROM]. Washington, DC: Transportation Research Board.
- McEwen, T. V., Priest, A. L., & Timm, D. H. (2004). *Design and instrumentation of the structural pavement experiment at the NCAT test track* (NCAT Report 04-01). Auburn, AL: National Center for Asphalt Technology, Auburn University.
- McGennis, R., Anderson, R., Kennedy, T., & Solaimanian, M. (1995). *Background of superpave asphalt mixture design & analysis system* (Report No. FHWA-SA-95-003). Washington, DC: Federal Highway Administration.
- Metcalfe, J. (1996). *Application of full-scale accelerated pavement testing* (NCHRP Synthesis 235). Washington, DC: Transportation Research Board.
- Mirza, M. W., & Witczak, M. W. (1995). Development of a global aging system for short and long term aging of asphalt cements. *Journal of the Association of Asphalt Paving Technologists*, 64, 393–430.
- Monismith, C. L., Hicks, R. G., Finn, F. M., Sousa, J., Harvey, J., Weissman, S., Paulsen, G. (1994). *Permanent deformation response of asphalt aggregate mixes* (SHRP-A-415). Washington, DC: Transportation Research Board.
- Monismith, C., Popescu, L., & Harvey, J. (2006). Use of shear test data for mix design, performance analysis, and rut depth prediction. In *Proceedings of the 10th International Conference on Asphalt Pavements—August 12 to 17, 2006, Québec City, Canada* (Volume 2, pp. 694–706). White Bear Lake, MN: International Society for Asphalt Pavements.
- Nabhan, P. A. (2015). *Calibration of the AASHTO MEPDG for flexible pavements to fit Nevada's conditions* (Master's thesis). Reno, NV: University of Nevada, Reno
- Noureldin, A. S., & Zhu, K. (2007). Network pavement evaluation using falling weight deflectometer and ground penetrating radar. *Transportation Research Record*, 1860, 90–99. <https://doi.org/10.3141/1860-10>
- Onyango, M. A. (2009). *Verification of mechanistic prediction models for permanent deformation in asphalt mixes using accelerated pavement testing* (Doctoral dissertation). Manhattan, KS: Kansas State University.
- Park, D.-W., Martin, A. E., & Masad, E. (2004). Simulation of permanent deformation using an elastic-viscoplastic constitutive relation. In *Proceedings of the 2nd International Conference on Accelerated Pavement Testing, September 26–29, Minneapolis, Minnesota*. Washington, DC: Transportation Research Board.
- Saal, N. J., & Pell, P. S. (1960). *Kolloid-Zeitschrift MI*. Heft 1, 61–71.

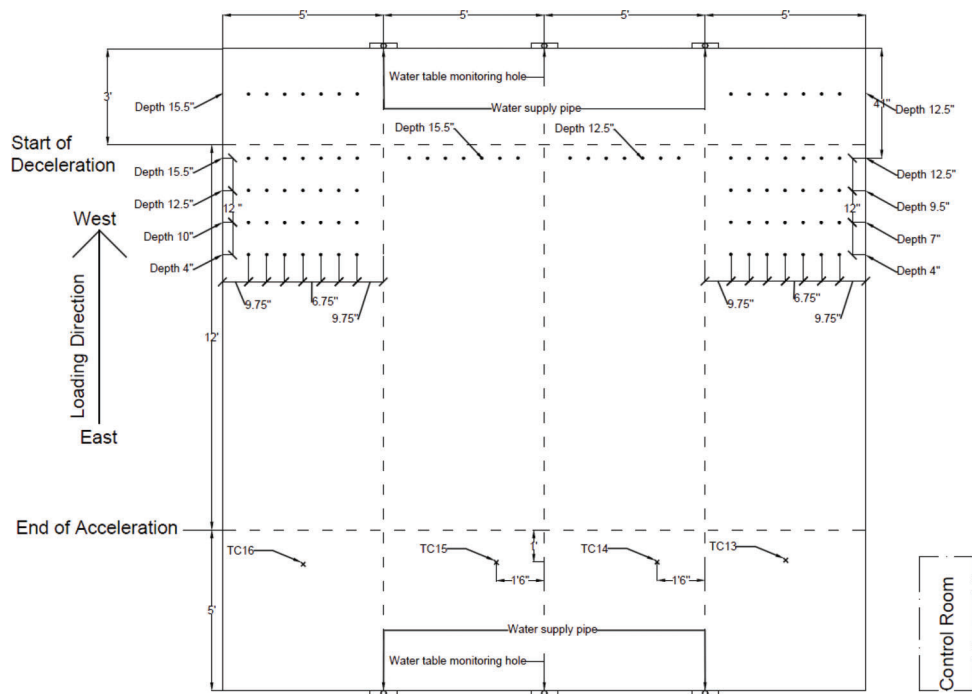
- Saeed, A., Hammons, M., & Bianchini, A. (2010). Airfield repairs in austere locations using pelletized asphalt technology. In *TRB 89th Annual Meeting compendium of papers* [CD-ROM]. Washington, DC: Transportation Research Board.
- Sivasubramaniam, S., & Haddock, J. E. (2006). *Validation of superpave mixture design and analysis procedures using the NCAT test track* (Joint Transportation Research Program Publication No. FHWA/IN/JTRP-2005/24). West Lafayette, IN: Purdue University. <https://doi.org/10.5703/1288284313375>
- Souliman, M., Mamlouk, M., El-Basyouny, M., & Zapata, C. (2010). Calibration of the AASHTO MEPDG for flexible pavement for arizona conditions. In *TRB 89th Annual Meeting compendium of papers* [CD-ROM]. Washington, DC: Transportation Research Board.
- Stiady, J. L., Hand, A. J., Noureldin, S., Hua, J., & White, T. D. (2003). *National Pooled Fund Study No 176, validation of SHRP asphalt mixture specifications using accelerated testing* (Joint Transportation Research Program Publication No. FHWA/IN/JTRP-2003/02). West Lafayette, IN: Purdue University. <https://doi.org/10.5703/1288284313276>
- Thompson, M. R., Barenberg, E. J., Carpenter, S. H., Darter, M. I., Dempsey, B. J., & Ioannides, A. M. (1990). *Calibrated mechanistic structural analysis procedures for pavements* (NCHRP Project 1-26). Washington, DC: Transportation Research Board.
- Timm, D. H., Priest, A. L., & McEwen, T. V. (2004). *Design and instrumentation of the structural pavement experiment at the NCAT test track* (NCAT Report 04-01). Auburn, AL: National Center for Asphalt Technology, Auburn University.
- Tseng, K., & Lytton, R. (1989). Prediction of permanent deformation in flexible pavement materials. In H. Schreuders & C. Marek (Eds.), *Implication of aggregates in the design, construction, and performance of flexible pavements* (STP 1016-EB, pp. 154–172). West Conshohocken, PA: ASTM International. <https://doi.org/10.1520/STP24562S>
- Uge, P., & van de Loo, P. (1974). *Permanent deformation of asphalt mixes*. Amsterdam, The Netherlands: Koninklijke/Shell-Laboratorium.
- Villiers, C., Roque, R., & Dietrich, B. (2005). Interpretation of transverse profiles to determine the source of rutting within asphalt pavement system. *Transportation Research Record*, 1905, 73–81. <https://doi.org/10.3141/1905-09>
- Von Quintus, H., Mallela, J., Bonaquist, R., Schwartz, C. W., & Carvalho, R. L. (2012). *Calibration of rutting models for structural and mix design* (NCHRP Report 719). Washington, DC: Transportation Research Board.
- White, T. D., Haddock, J. E., Hand, A. J., & Fang, H. (2002). *Contributions of pavement structural layers to rutting of hot mix asphalt pavements* (NCHRP Report 468). Washington, DC: Transportation Research Board.
- Williams, C., & Shaidur, R. (2013). *Mechanistic-Empirical Pavement Design Guide calibration for pavement rehabilitation*. Salem, OR: Oregon Department of Transportation.
- Xu, Q., & Mohammad, L. (2008). Modeling asphalt pavement rutting under accelerated testing. *Road Materials and Pavement Design*, 9(4), 665–687. <https://doi.org/10.1080/14680629.2008.9690144>
- Zafar, R., Nassar, W., & Elbella, A. (2005). Interaction between pavement instrumentation and hot-mix-asphalt in flexible pavements. *Emirates Journal for Engineering Research*, 10(1), 49–55.
- Zhou, F., & Scullion, T. (2002). *VESYS5 rutting model calibrations with local accelerated pavement test data and associated implementation* (Publication No. FHWA/TX-03/9-1502-01-2). College Station, TX: Texas Transportation Institute.

APPENDIX A. INSTRUMENTATION PLAN



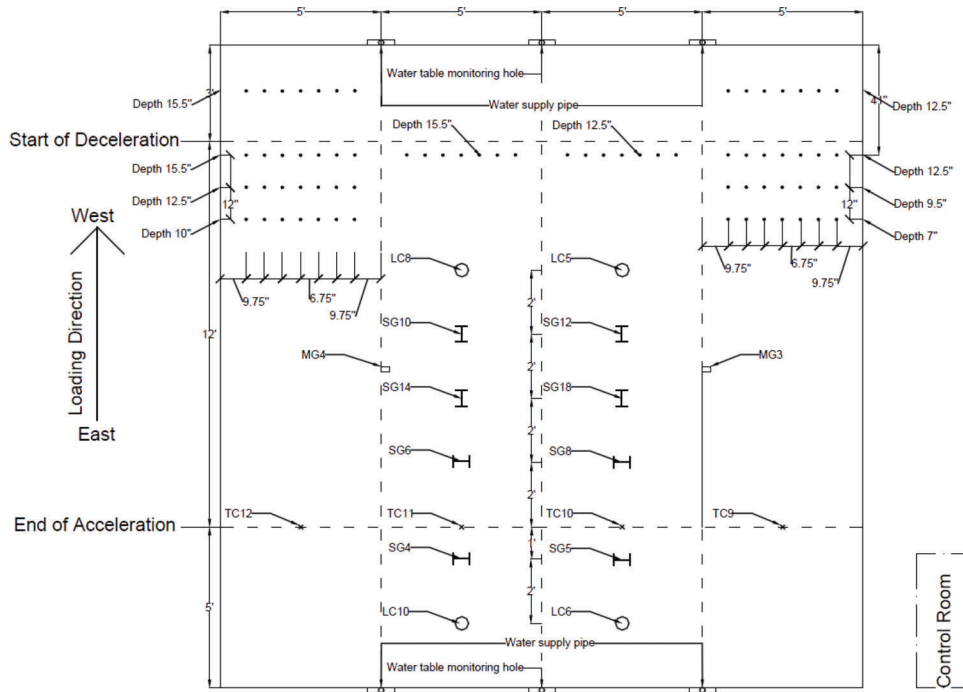
TC: Thermocouple; MG: Moisture Gauge; SG: Strain Gauge; LC: Load Cell

Figure A.1 Plan view of the intermediate layer surface.



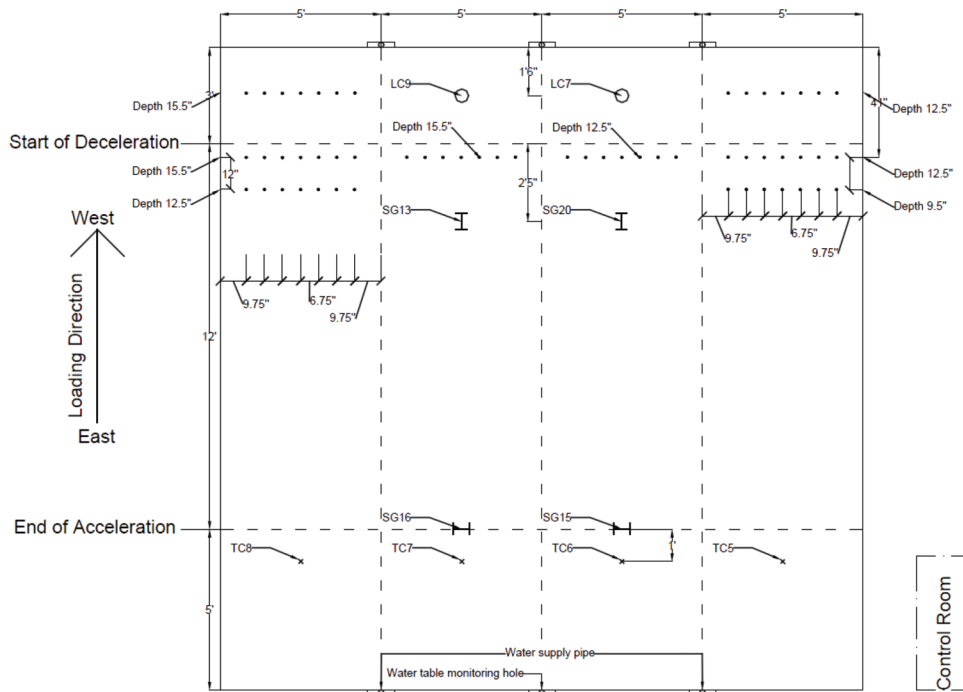
TC: Thermocouple; MG: Moisture Gauge; SG: Strain Gauge; LC: Load Cell

Figure A.2 Plan view of the upper base layer surface.



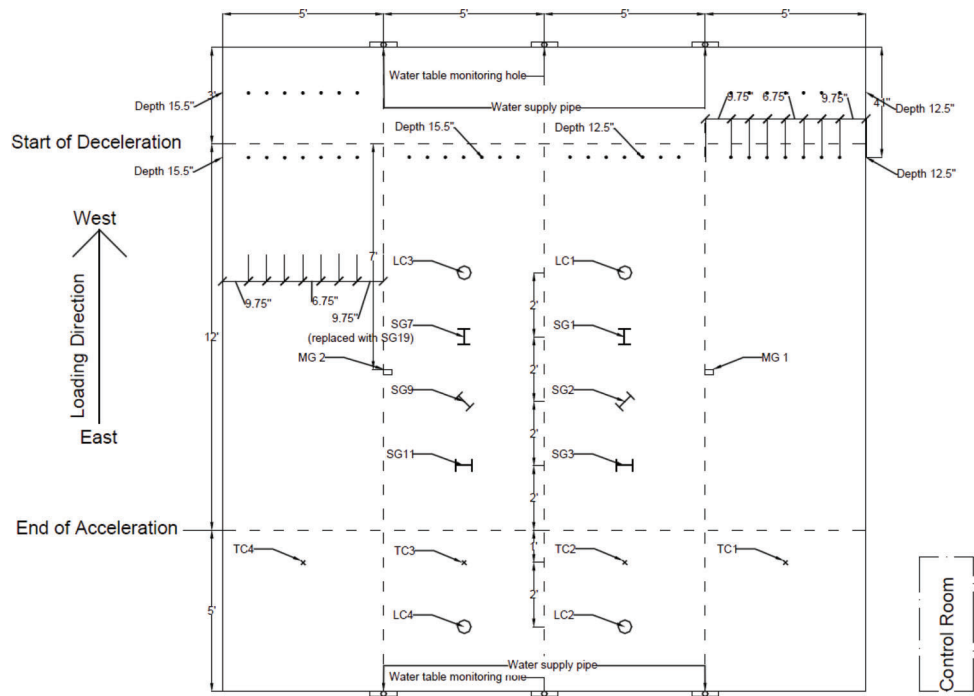
TC: Thermocouple; MG: Moisture Gauge; SG: Strain Gauge; LC: Load Cell

Figure A.3 Plan view of the open-graded layer surface.



TC: Thermocouple; MG: Moisture Gauge; SG: Strain Gauge; LC: Load Cell

Figure A.4 Plan view of the lower base layer surface.



TC: Thermocouple; MG: Moisture Gauge; SG: Strain Gauge; LC: Load Cell

Figure A.5 Plan view of the subgrade surface.

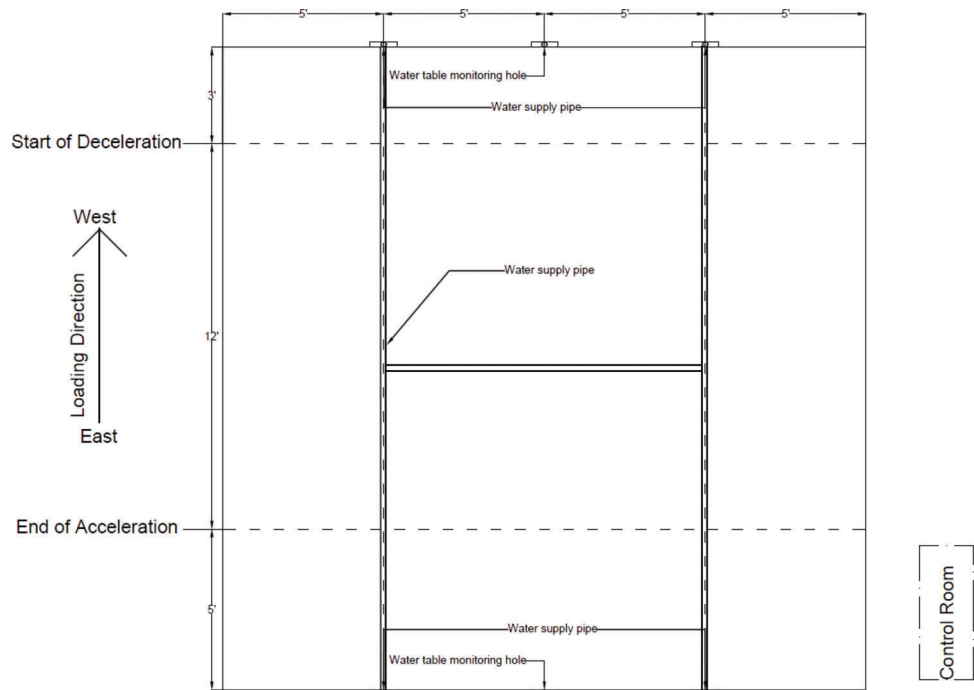


Figure A.6 Plan view of the original surface.

APPENDIX B. ACCELERATED PAVEMENT TEST LOAD APPLICATION HISTORY

TABLE B.1
Load Application History of Lane 1

Start Time	End Time	Passes Applied	Cumulative Passes
8/27/14 1:45 PM	8/27/14 1:49 PM	25	25
8/28/14 9:28 AM	8/28/14 9:32 AM	25	50
9/2/14 2:45 PM	9/2/14 2:49 PM	25	75
9/8/14 1:49 PM	9/8/14 1:53 PM	25	100
9/10/14 12:40 PM	9/10/14 12:58 PM	100	200
9/24/14 11:47 AM	9/24/14 12:05 PM	100	300
9/26/14 8:30 AM	9/26/14 8:48 AM	100	400
9/30/14 11:18 AM	9/30/14 11:36 AM	100	500
10/1/14 2:27 PM	10/1/14 2:45 PM	100	600
10/2/14 1:23 PM	10/2/14 1:41 PM	100	700
10/6/14 2:51 PM	10/6/14 3:09 PM	100	800
10/7/14 2:36 PM	10/7/14 2:54 PM	100	900
10/8/14 2:47 PM	10/8/14 3:05 PM	100	1,000
10/9/14 10:56 AM	10/9/14 12:29 PM	500	1,500
10/16/14 9:14 AM	10/16/14 10:47 AM	500	2,000
11/5/14 12:05 PM	11/5/14 1:38 PM	500	2,500
11/13/14 10:47 AM	11/13/14 12:20 PM	500	3,000
11/17/14 2:50 PM	11/17/14 5:57 PM	1000	4,000
11/20/14 9:30 AM	11/20/14 12:37 PM	1000	5,000
12/2/14 6:30 PM	12/3/14 2:19 AM	2500	7,500
12/4/14 7:00 AM	12/4/14 2:49 PM	2500	10,000
12/8/14 10:30 AM	12/8/14 6:19 PM	2500	12,500
12/10/14 6:37 AM	12/10/14 2:26 PM	2500	15,000
12/12/14 7:12 AM	12/12/14 3:01 PM	2500	17,500
12/15/14 9:07 AM	12/15/14 4:56 PM	2500	20,000
1/20/15 11:00 AM	1/20/15 6:49 PM	2500	22,500
1/21/15 9:41 AM	1/21/15 5:30 PM	2500	25,000
1/22/15 9:00 AM	1/22/15 4:49 PM	2500	27,500
1/23/14 9:00 AM	1/23/14 4:49 PM	2500	30,000
3/3/15 12:00 PM	3/4/15 3:38 AM	5000	35,000
3/5/15 12:00 PM	3/6/15 3:38 AM	5000	40,000
3/11/15 12:00 PM	3/12/15 3:38 AM	5000	45,000
3/18/2015 12:00	3/19/15 3:38 AM	5000	50,000

TABLE B.2
Load Application History of Lane 4

Start Time	End Time	Passes Applied	Cumulative Passes
7/20/15 2:09 PM	7/20/15 2:13 PM	25	25
7/21/15 2:30 PM	7/21/15 2:34 PM	25	50
7/22/15 8:50 AM	7/22/15 8:54 AM	25	75
7/22/15 3:10 PM	7/22/15 3:14 PM	25	100
7/22/15 7:34 PM	7/22/15 7:52 PM	100	200
7/23/15 3:09 PM	7/23/15 3:27 PM	100	300
7/23/15 9:00 PM	7/23/15 9:18 PM	100	400
7/24/15 7:50 AM	7/24/15 8:08 AM	100	500
7/24/15 4:34 PM	7/24/15 4:52 PM	100	600
7/27/15 3:45 PM	7/27/15 4:03 PM	100	700
7/27/15 10:11 PM	7/27/15 10:29 PM	100	800
7/28/15 8:32 AM	7/28/15 8:50 AM	100	900
7/28/15 12:15 PM	7/28/15 12:33 PM	100	1,000
7/28/15 5:30 PM	7/28/15 7:03 PM	500	1,500
7/30/15 7:56 AM	7/30/15 9:29 AM	500	2,000
7/30/15 4:15 PM	7/30/15 5:48 PM	500	2,500
7/31/15 8:30 AM	7/31/15 10:03 AM	500	3,000
8/2/15 9:46 AM	8/2/15 12:53 PM	1000	4,000
8/2/15 5:05 PM	8/2/15 8:12 PM	1000	5,000
8/6/15 9:00 AM	8/6/15 4:49 PM	2500	7,500
8/12/15 8:42 AM	8/12/15 4:31 PM	2500	10,000
8/21/15 8:53 AM	8/21/15 4:42 PM	2500	12,500
8/26/15 9:00 AM	8/26/15 4:49 PM	2500	15,000
8/28/15 9:30 AM	8/28/15 5:19 PM	2500	17,500
8/29/15 9:40 AM	8/29/15 5:29 PM	2500	20,000
8/30/15 11:00 AM	8/30/15 6:49 PM	2500	22,500
8/31/15 9:30 AM	8/31/15 5:19 PM	2500	25,000
9/1/15 9:00 AM	9/1/15 4:49 PM	2500	27,500
9/2/15 8:30 AM	9/2/15 4:19 PM	2500	30,000
9/2/15 7:30 PM	9/3/15 11:08 AM	5000	35,000
10/6/15 9:00 AM	10/7/15 12:38 AM	5000	40,000
10/7/15 9:00 AM	10/8/15 12:38 AM	5000	45,000
10/9/2015 12:00	10/10/15 3:38 AM	5000	50,000

TABLE B.3
Load Application History of Lane 3

Start Time	End Time	Passes Applied	Cumulative Passes
11/22/15 11:00 AM	11/22/15 11:04 AM	25	25
11/22/15 2:55 PM	11/22/15 2:59 PM	25	50
11/22/15 11:50 PM	11/22/15 11:54 PM	25	75
11/23/15 7:30 AM	11/23/15 7:34 AM	25	100
11/23/15 10:40 AM	11/23/15 10:58 AM	100	200
11/26/15 8:10 AM	11/26/15 8:28 AM	100	300
11/26/15 11:45 AM	11/26/15 12:03 PM	100	400
11/26/15 3:10 PM	11/26/15 3:28 PM	100	500
11/26/15 10:05 PM	11/26/15 10:23 PM	100	600
11/27/15 2:44 PM	11/27/15 3:02 PM	100	700
11/27/15 6:08 PM	11/27/15 6:26 PM	100	800
11/28/15 8:20 AM	11/28/15 8:38 AM	100	900
11/28/15 12:00 PM	11/28/15 12:18 PM	100	1,000
11/28/15 3:40 PM	11/28/15 5:13 PM	500	1,500
11/29/15 12:03 PM	11/29/15 1:36 PM	500	2,000
11/29/15 11:00 PM	11/30/15 12:33 AM	500	2,500
11/30/15 9:00 AM	11/30/15 10:33 AM	500	3,000
11/30/15 5:00 PM	11/30/15 8:07 PM	1000	4,000
11/30/15 11:19 PM	12/1/15 2:26 AM	1000	5,000
12/1/15 10:00 PM	12/2/15 5:49 AM	2500	7,500
12/2/15 10:38 PM	12/3/15 6:27 AM	2500	10,000
12/3/15 7:47 PM	12/4/15 3:36 AM	2500	12,500
12/5/15 12:47 AM	12/5/15 8:36 AM	2500	15,000
12/5/15 3:40 PM	12/5/15 11:29 PM	2500	17,500
12/6/15 10:30 AM	12/6/15 6:19 PM	2500	20,000
12/7/15 8:32 AM	12/7/15 4:21 PM	2500	22,500
12/7/15 9:36 PM	12/8/15 5:25 AM	2500	25,000
12/8/15 11:43 AM	12/8/15 7:32 PM	2500	27,500
12/8/15 11:01 PM	12/9/15 6:50 AM	2500	30,000
12/9/15 5:59 PM	12/10/15 9:37 AM	5000	35,000
12/10/15 9:05 PM	12/11/15 12:43 PM	5000	40,000
12/11/15 9:49 PM	12/12/15 1:27 PM	5000	45,000
12/12/2015 22:29	12/13/15 2:07 PM	5000	50,000

APPENDIX C. MATERIAL INPUTS

TABLE C.1
Material Inputs for 1 APT Lane 1

Layer	Surface	Intermediate	Upper Base	OG	Lower Base	Subgrade
HMA Mix						
G_{mm}	2.533	2.578	2.578	2.648	2.578	
Poisson's ratio	0.35	0.35	0.35	0.35	0.35	
G_{mb}	2.356	2.398	2.398	2.463	2.398	
$p_b\%$	5.7	4.6	4.6	3.1	4.6	
G_{se}	2.787	2.787	2.787	2.793	2.787	
G_{sb}	2.716	2.719	2.719	2.723	2.719	
$v_{bc}\%$	11.2	8.9	8.9	5.4	8.9	
γ_{HMA}	147.1	149.7	149.7	153.7	149.7	
% passing 3/4-inch sieve	100.0	98.6	98.6	96.0	98.6	
% passing 3/8-inch sieve	95.9	70.4	70.4	39.9	70.4	
% passing No. 4 sieve	65.7	43.2	43.2	19.2	43.2	
% passing No. 200 sieve	4.6	5.1	5.1	3.9	5.1	
PG	70-22	70-22	64-22	76-22	64-22	
Unbound Material						
Resilient Modulus						6,956
Soil Classification						A-6
Poisson's Ratio						0.35
k_0						0.5

TABLE C.2
Material Inputs for 2 APT Lane 3

Layer	Surface	Intermediate	Upper Base	OG	Lower Base	Subgrade
HMA Mix						
G_{mm}	2.826	2.578	2.578	2.648	2.578	
Poisson's ratio	0.35	0.35	0.35	0.35	0.35	
G_{mb}	2.628	2.398	2.398	2.463	2.398	
$p_b\%$	5.6	4.6	4.6	3.1	4.6	
G_{se}	3.163	2.787	2.787	2.793	2.787	
G_{sb}	3.101	2.719	2.719	2.723	2.719	
$v_{bc}\%$	13.0	8.9	8.9	5.4	8.9	
γ_{HMA}	164.1	149.7	149.7	153.7	149.7	
% passing 3/4-inch sieve	100.0	98.6	98.6	96.0	98.6	
% passing 3/8-inch sieve	90.3	70.4	70.4	39.9	70.4	
% passing No. 4 sieve	38.7	43.2	43.2	19.2	43.2	
% passing No. 200 sieve	7.6	5.1	5.1	3.9	5.1	
PG	70-22	70-22	64-22	76-22	64-22	
Unbound Material						
Resilient Modulus						9,849
Soil Classification						A-6
Poisson's Ratio						0.35
k_0						0.5

TABLE C.3
Material Inputs for 3 APT Lane 4

Layer	Surface	Intermediate	Upper Base	OG	Lower Base	Subgrade
HMA Mix						
G_{mm}	2.533	2.578	2.578	2.648	2.578	
Poisson's ratio	0.35	0.35	0.35	0.35	0.35	
G_{mb}	2.356	2.398	2.398	2.463	2.398	
$p_b\%$	5.7	4.6	4.6	3.1	4.6	
G_{se}	2.787	2.787	2.787	2.793	2.787	
G_{sb}	2.716	2.719	2.719	2.723	2.719	
$v_{be}\%$	11.2	8.9	8.9	5.4	8.9	
γ_{HMA}	147.1	149.7	149.7	153.7	149.7	
% passing 3/4-inch sieve	100.0	98.6	98.6	96.0	98.6	
% passing 3/8-inch sieve	95.9	70.4	70.4	39.9	70.4	
% passing No. 4 sieve	65.7	43.2	43.2	19.2	43.2	
% passing No. 200 sieve	4.6	5.1	5.1	3.9	5.1	
PG	70-22	70-22	64-22	76-22	64-22	
Unbound Material						
Resilient Modulus						6,158
Soil Classification						A-6
Poisson's Ratio						0.35
k_0						0.5

TABLE C.4
Material Inputs for 4 Previous APT Lane 1

Layer	Surface	Intermediate	Base	Subgrade
HMA Mix				
G_{mm}	2.500	2.548	2.560	
Poisson's ratio	0.35	0.35	0.35	
G_{mb}	2.325	2.370	2.381	
$p_b\%$	6.2	4.1	4.0	
G_{se}	2.770	2.725	2.735	
G_{sb}	2.657	2.724	2.696	
$v_{be}\%$	10.9	9.6	8.2	
γ_{HMA}	145.2	147.9	148.6	
% passing 3/4-inch sieve	100.0	97.9	85.2	
% passing 3/8-inch sieve	96.1	69.2	49.5	
% passing No. 4 sieve	69.8	46.0	39.7	
% passing No. 200 sieve	5.6	3.8	3.8	
PG	70-22	70-22	64-22	
Unbound Material				
Resilient Modulus				26,121
Soil Classification				A-4
Poisson's Ratio				0.35
k_0				0.5

TABLE C.5
Material Inputs for 4 Previous APT Lane 2

Layer	Surface	Intermediate	Base	Subgrade
HMA Mix				
G_{mm}	2.500	2.548	2.560	
Poisson's ratio	0.35	0.35	0.35	
G_{mb}	2.325	2.370	2.381	
$p_b\%$	6.2	4.1	4.0	
G_{se}	2.770	2.725	2.735	
G_{sb}	2.657	2.724	2.696	
$v_{be}\%$	10.9	9.6	8.2	
γ_{HMA}	145.2	147.9	148.6	
% passing 3/4inch sieve	100.0	97.9	85.2	
% passing 3/8-inch sieve	96.1	69.2	49.5	
% passing No. 4 sieve	69.8	46.0	39.7	
% passing No. 200 sieve	5.6	3.8	3.8	
PG	70-22	70-22	64-22	
Unbound Material				
Resilient Modulus				20,507
Soil Classification				A-4
Poisson's Ratio				0.35
k_0				0.5

TABLE C.6
Material Inputs for 6 SR-43 25550

Layer	Surface	Intermediate	Base	Subgrade
HMA Mix				
G_{mm}	2.547	2.587	2.567	
Poisson's ratio	0.35	0.35	0.35	
G_{mb}	2.369	2.406	2.387	
$p_b\%$	5.5	4.3	4.7	
G_{se}	2.795	2.782	2.778	
G_{sb}	2.743	2.730	2.733	
$v_{bc}\%$	11.4	8.7	9.8	
γ_{HMA}	147.9	150.2	149.0	
% passing 3/4-inch sieve	100.0	97.4	96.9	
% passing 3/8-inch sieve	95.0	70.1	60.8	
% passing No. 4 sieve	58.3	44.4	39.5	
% passing No. 200 sieve	5.0	5.4	4.9	
PG	76-22	76-22	64-22	
Unbound Material				
Resilient Modulus				
Soil Classification			No. 53	
Poisson's Ratio			0.35	
k_0			0.5	

TABLE C.7
Material Inputs for 7 SR-28 27265

Layer	Surface	Intermediate	Base	Subgrade
HMA Mix				
G_{mm}	2.544	2.587	2.572	
Poisson's ratio	0.35	0.35	0.35	
G_{mb}	2.366	2.406	2.392	
$p_b\%$	5.4	4.3	3.9	
G_{se}	2.785	2.782	2.744	
G_{sb}	2.719	2.730	2.733	
$v_{bc}\%$	10.7	8.7	8.9	
γ_{HMA}	147.7	150.2	149.3	
% passing 3/4-inch sieve	100.0	97.4	81.2	
% passing 3/8-inch sieve	95.5	70.1	53.8	
% passing No. 4 sieve	63.6	44.4	38.9	
% passing No. 200 sieve	5.7	5.4	4.8	
PG	70-22	70-22	64-22	
Unbound Material				
Resilient Modulus				
Soil Classification			No. 53	
Poisson's Ratio			0.35	
k_0			0.5	

TABLE C.8
Material Inputs for 8 US-41 28441

Layer	Surface	Intermediate	Base	Subgrade
HMA Mix				
G_{mm}	2.513	2.517	2.532	
Poisson's ratio	0.35	0.35	0.35	
G_{mb}	2.337	2.341	2.355	
$p_b\%$	5.4	4.0	4.1	
G_{se}	2.746	2.684	2.706	
G_{sb}	2.712	2.669	2.666	
$v_{bc}\%$	11.5	8.8	8.3	
γ_{HMA}	145.9	146.1	147.0	
% passing 3/4-inch sieve	100.0	98.7	84.0	
% passing 3/8-inch sieve	96.0	85.0	67.3	
% passing No. 4 sieve	63.4	62.6	39.5	
% passing No. 200 sieve	4.0	4.6	4.1	
PG	76-22	76-22	64-22	
Unbound Material				
Resilient Modulus				
Soil Classification			No. 53	
Poisson's Ratio			0.35	
k_0			0.5	

TABLE C.9
Material Inputs for 9 SR-43 29399

Layer	Surface	Intermediate	Base	Subgrade
HMA Mix				
G_{mm}	2.500	2.548	2.584	
Poisson's ratio	0.35	0.35	0.35	
G_{mb}	2.325	2.370	2.403	
$p_b\%$	6.2	4.5	4.2	
G_{se}	2.770	2.745	2.773	
G_{sb}	2.657	2.689	2.718	
$v_{bc}\%$	10.9	8.8	8.3	
γ_{HMA}	145.2	147.9	150.0	
% passing 3/4-inch sieve	100.0	96.6	88.3	
% passing 3/8-inch sieve	96.1	71.3	63.6	
% passing No. 4 sieve	69.8	49.0	48.8	
% passing No. 200 sieve	5.6	3.9	4.0	
PG	70-22	64-22	64-22	
Unbound Material				
Resilient Modulus				
Soil Classification			No. 53	
Poisson's Ratio			0.35	
k_0			0.5	

TABLE C.10
Material Inputs for 10 US-40 29133

Layer	Surface	Intermediate	Base	Subgrade
HMA Mix				
G_{mm}	2.468	2.514	2.527	
Poisson's ratio	0.35	0.35	0.35	
G_{mb}	2.295	2.338	2.350	
$p_b\%$	6.5	4.1	3.8	
G_{se}	2.743	2.685	2.686	
G_{sb}	2.617	2.680	2.661	
$v_{be}\%$	11.0	9.3	8.0	
γ_{HMA}	143.3	146.0	146.7	
% passing 3/4-inch sieve	100.0	97.4	88.0	
% passing 3/8-inch sieve	94.2	75.6	68.0	
% passing No. 4 sieve	67.2	46.3	39.0	
% passing No. 200 sieve	4.9	5.3	5.3	
PG	76-22	76-22	64-22	
Unbound Material				
Resilient Modulus				
Soil Classification			No. 53	
Poisson's Ratio			0.35	
k_0			0.5	

TABLE C.11
Material Inputs for 11 I-465 29137

Layer	Surface	Intermediate	Base	Subgrade
HMA Mix				
G_{mm}	3.023	2.525	2.543	
Poisson's ratio	0.35	0.35	0.35	
G_{mb}	2.811	2.348	2.365	
$p_b\%$	6.0	4.0	3.8	
G_{se}	3.464	2.693	2.705	
G_{sb}	3.388	2.672	2.671	
$v_{be}\%$	15.0	8.6	7.8	
γ_{HMA}	175.5	146.6	147.7	
% passing 3/4-inch sieve	100.0	96.6	84.1	
% passing 3/8-inch sieve	89.8	72.0	60.0	
% passing No. 4 sieve	40.5	41.0	38.0	
% passing No. 200 sieve	8.6	5.2	5.0	
PG	76-22	76-22	64-22	
Unbound Material				
Resilient Modulus				
Soil Classification			No. 53	
Poisson's Ratio			0.35	
k_0			0.5	

TABLE C.12
Material Inputs for 12 US-421 29320

Layer	Surface	Intermediate	Base	Subgrade
HMA Mix				
G_{mm}	2.426	2.504	2.508	
Poisson's ratio	0.35	0.35	0.35	
G_{mb}	2.256	2.329	2.332	
$p_b\%$	6.0	4.5	4.3	
G_{se}	2.664	2.692	2.687	
G_{sb}	2.607	2.650	2.657	
$v_{be}\%$	11.6	9.1	9.0	
γ_{HMA}	140.9	145.4	145.6	
% passing 3/4-inch sieve	100.0	97.2	97.2	
% passing 3/8-inch sieve	94.6	73.5	72.2	
% passing No. 4 sieve	64.6	48.5	44.0	
% passing No. 200 sieve	4.9	3.6	3.4	
PG	70-22	70-22	64-22	
Unbound Material				
Resilient Modulus				
Soil Classification				A-6
Poisson's Ratio				0.35
k_0				0.5

TABLE C.13
Material Inputs for 13 US-31 29310

Layer	Surface	Intermediate	Base	Subgrade
HMA Mix				
G_{mm}	2.500	2.548	2.560	
Poisson's ratio	0.35	0.35	0.35	
G_{mb}	2.325	2.370	2.381	
$p_b\%$	6.2	4.1	4.0	
G_{se}	2.770	2.725	2.735	
G_{sb}	2.657	2.724	2.696	
$v_{be}\%$	10.9	9.6	8.2	
γ_{HMA}	145.2	147.9	148.6	
% passing 3/4-inch sieve	100.0	97.9	85.2	
% passing 3/8-inch sieve	96.1	69.2	49.5	
% passing No. 4 sieve	69.8	46.0	39.7	
% passing No. 200 sieve	5.6	3.8	3.8	
PG	70-22	70-22	64-22	
Unbound Material				
Resilient Modulus				
Soil Classification				A-4
Poisson's Ratio				0.35
k_0				0.5

APPENDIX D. DISTRESS DATA

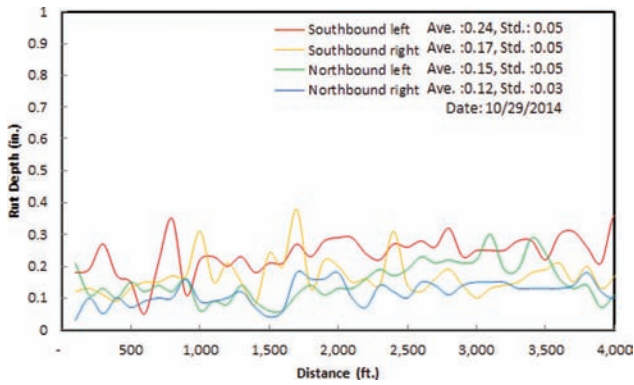


Figure D.1 Rut depth measurements from 6 SR-43-25550.

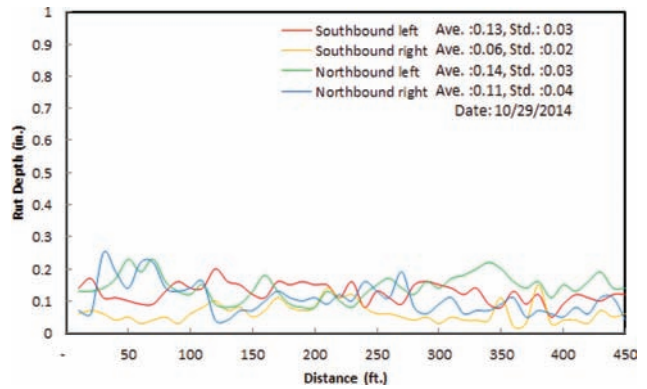


Figure D.4 Rut depth measurements from 9 SR-43-29399.

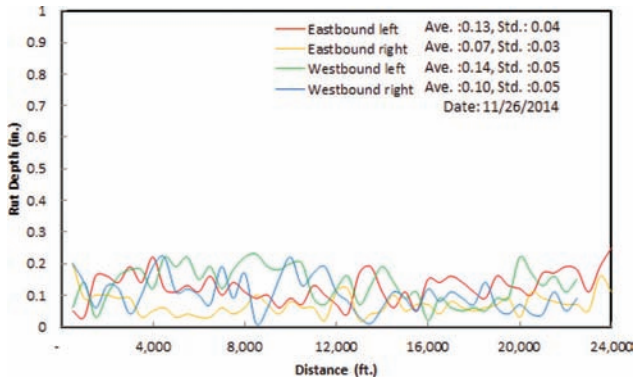


Figure D.2 Rut depth measurements from 7 SR-28-27265.

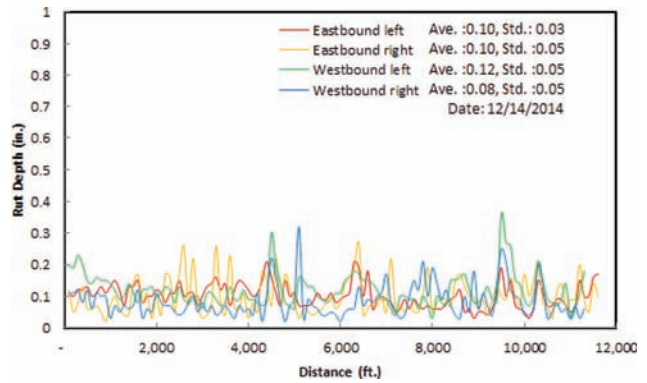


Figure D.5 Rut depth measurements from 10 US-40-29133.

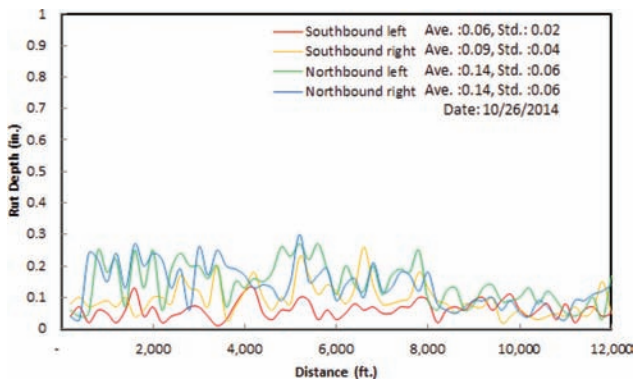


Figure D.3 Rut depth measurements from 8 US-41-28441.

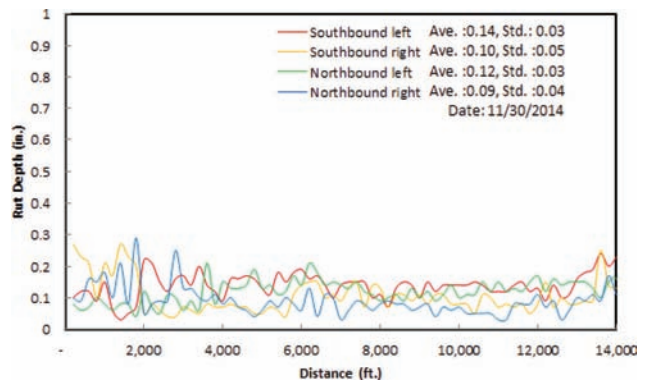


Figure D.6 Rut depth measurements from 11 I-465-29137.

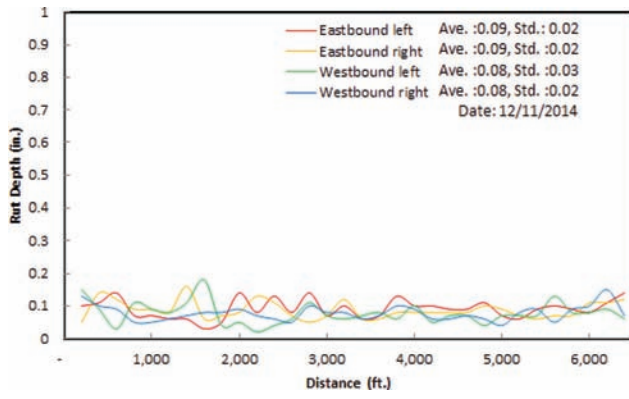


Figure D.7 Rut depth measurements from 12 US-421-29320.

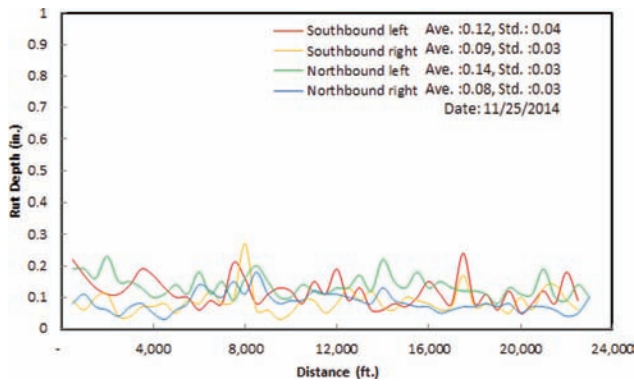


Figure D.8 Rut depth measurements from 13 US-31-29310.

About the Joint Transportation Research Program (JTRP)

On March 11, 1937, the Indiana Legislature passed an act which authorized the Indiana State Highway Commission to cooperate with and assist Purdue University in developing the best methods of improving and maintaining the highways of the state and the respective counties thereof. That collaborative effort was called the Joint Highway Research Project (JHRP). In 1997 the collaborative venture was renamed as the Joint Transportation Research Program (JTRP) to reflect the state and national efforts to integrate the management and operation of various transportation modes.

The first studies of JHRP were concerned with Test Road No. 1—evaluation of the weathering characteristics of stabilized materials. After World War II, the JHRP program grew substantially and was regularly producing technical reports. Over 1,600 technical reports are now available, published as part of the JHRP and subsequently JTRP collaborative venture between Purdue University and what is now the Indiana Department of Transportation.

Free online access to all reports is provided through a unique collaboration between JTRP and Purdue Libraries. These are available at: <http://docs.lib.purdue.edu/jtrp>

Further information about JTRP and its current research program is available at: <http://www.purdue.edu/jtrp>

About This Report

An open access version of this publication is available online. This can be most easily located using the Digital Object Identifier (doi) listed below. Pre-2011 publications that include color illustrations are available online in color but are printed only in grayscale.

The recommended citation for this publication is:

Nantung, T., Lee, J., & Tian, Y. (2018). *Efficient pavement thickness design for Indiana* (Joint Transportation Research Program Publication No. FHWA/IN/JTRP-2018/06). West Lafayette, IN: Purdue University. <https://doi.org/10.5703/1288284316649>